NANODIAMOND PARTICLES FOR BIOMACROMOLECULE IMMOBILIZATION AND DYE CONTAMINANT ADSORPTION

A Thesis Submitted to the College of Graduate Studies and Research

In Partial Fulfillment of the Requirements

For the Degree of Doctor of Philosophy

In the Division of Biomedical Engineering

University of Saskatchewan

Saskatoon

By

HAIDONG WANG

PERMISSION TO USE

In presenting this thesis in partial fulfillment of the requirements for a Postgraduate degree from the University of Saskatchewan, I agree that the Libraries of this University may make it freely available for inspection. I further agree that permission for copying of this thesis in any manner, in whole or in part, for scholarly purposes may be granted by Professor Qiaoqin Yang and Professor Catherine Hui Niu, who supervised my thesis work or, in their absence, by the Head of the Department or the Dean of the College in which my thesis work was done. It is understood that any copying or publication or use of this thesis or parts thereof for financial gain shall not be allowed without my written permission. It is also understood that due recognition shall be given to me and to the University of Saskatchewan in any scholarly use which may be made of any material in my thesis.

Requests for permission to copy or to make other use of material in this thesis in whole or part should be addressed to:

Head of the Division of Biomedical Engineering

University of Saskatchewan

Saskatoon, Saskatchewan, S7N 5A9, Canada

ABSTRACT

Nanodiamond (ND) has become a widely studied material in recent years due to its excellent properties, which includes high specific surface area, oxygen-containing surface groups (desirable for physical or chemical functionalization), physically and chemically inert diamond core, optical transparency, and biocompatibility. ND has been found to be biocompatible and have no cytotoxicity to cells. To date, significant attention has been focused on utilizing ND material as a platform for biomacromolecule immobilization which is promising for biological applications such as biosensor. Moreover, excellent surface properties of ND might be able to make it a desirable adsorbent material. The present thesis work has focused on using ND for biomacromolecule immobilization as well as dye contaminant adsorption.

First, the immobilization of an important biomacromolecule, carboxymethyl chitosan, onto ND surface as well as the properties of the product was investigated in detail. The carboxymethyl chitosan modified ND (NDCMCS) shows improved dispersity especially in low and high pH aqueous solutions. Moreover, the rich content of primary amine and hydroxyl on CMCS backbone would render further physical or chemical functionalization of ND more flexible and versatile. The following work is then focusing on the protein adsorption behaviors onto ND surface as well as whether protein could retain its structural features upon immobilization. To this end, bovine serum albumin (BSA) was chosen as a model protein for the study of protein conformation and the interaction between ND and protein in their complex. The results have demonstrated that ND is an excellent platform for protein immobilization with high affinity and

approximately 80% of BSA structural features could be preserved upon immobilization.

Second, based on strong ND-protein interaction, the assembly of ND-protein complex into macroscale material in a Layer-by-Layer (LBL) assembly fashion has been studied. The LBL assembly properties of ND-BSA complex with pristine ND were investigated on glass substrates. The ND-BSA/ND coatings fabricated by LBL assembly method were stable and more densely-organized coating structures could be obtained by increasing the number of bilayers deposited. The LBL assembly method for ND-protein coating fabrication could be easily employed to prepare biomacromolecule-functionalized ND films for biosensor applications. In the following work, it was found that NDs could also assemble into thin films through hydrogen bonding on a glass substrate. The films prepared have regularly-organized nanostructures, which could be tuned by adjusting the number of bilayers deposited. Moreover, the oxygen-containing surface groups on LBL films make possible the further functionalization by chemical or physical approach.

Finally, the excellent surface properties of ND have found new promising applications in addressing current environmental issues and ND has been demonstrated to be an effective dye contaminant adsorbent. In this work, the adsorption of azo dye acid orange 7 (AO7) onto ND surface has been investigated in order to ascertain the adsorption behavior as well as the interaction involved in the adsorption process, where ND has been proved to have higher capacity in azo dye adsorption than widely used activated carbons and carbon nanotubes. Due to strong π-donor-acceptor interaction between ND surface graphite layer and azo bond, ND shows high affinity with azo dye. Though affinity is slightly lower at high pH values, the adsorption

coefficients of ND with AO7 at neutral to alkaline pHs are still of the same orders of magnitude with those of low pH values, suggesting that ND could be a desirable candidate for textile wastewater treatment which is normally at alkaline pH.

The present thesis work might potentially contribute to utilizing NDs for biological and environmental applications.

ACKNOWLEDGMENTS

First and foremost, I would like to extend my heartfelt gratitude and thanks to my supervisors Professor Qiaoqin Yang and Professor Catherine Hui Niu for their great guidance and support throughout this research project. Second, I would like to thank my advisory committee members Professor Ildiko Badea, Professor Richard W. Evitts and Professor Chijin Xiao, for their critical guidance and kind encouragement. Special gratitude goes to Professor Ildiko Badea for her significant input in this project as well as inspiring discussions.

I would like to thank the entire faculty and staff in the Division of Biomedical Engineering, Department of Chemical and Biological Engineering as well as Department of Mechanical Engineering for providing an excellent research environment. Richard Blondin, Heli Eunike, Robert Peace, and Dragan Cekic deserve special thanks for their constant technical support. My thanks go to Jagbir Singh and McDonald Donkuru for providing help in dynamic light scattering analysis. I would like to thank Dr. Guosheng Liu, Dr. Ramaswami Sammynaiken, Tom Bonli, and Jason Maley for sample characterization. I also wish to appreciate the great help and friendship from all my colleagues.

My appreciation goes to the University of Saskatchewan, the Canada Research Chair Program, the Natural Sciences and Engineering Research Council of Canada, and the Canada Foundation for Innovation for financial support and infrastructure.

Finally, I would like to give my deepest thanks to my parents and all my family for their love.

DEDICATION

My Parents

Tianjie WANG

and

Qingli QIN

TABLE OF CONTENTS

LIST OF TABLES

LIST OF FIGURES

ACRONYMS

AC	Activated Carbon
A Form	Aged Form
AO7	Acid Orange 7
5-ASA	5-Aminosalicylic Acid
ATRP	Atom Transfer Radical Polymerization
B Form	Basic Form
BSA	Bovine Serum Albumin
α-BTX	α-Bungarotoxin
CD	Circular Dichroism Spectroscopy
CMCS	Carboxymethyl Chitosan
CNT	Carbon Nanotube
CS	Chitosan
CVD	Chemical Vapor Deposition
Dex	Dexamethasone
DI Water	Deionized Water
DNA	Deoxyribonucleic acid
EDC	1-(3-Dimethylaminopropyl)-3-Ethylcarbodiimide Hydrochloride
E Form	Expanded Form
F Form	Fast Form

FT-IR	Fourier Transform Infrared Spectroscopy
HPHT	High Pressure High Temperature
LBL	Layer-by-Layer
LMCS	Low Molecular Weight Chitosan
MALDITOF-MS	Matrix-assisted Laser Desorption/ionization Time-of-flight Mass Spectrometry
MES	2-(N-Morpholino) ethanesulfonic acid
MWNT	Multi-walled Carbon Nanotube
NCD	Nanocrystalline Diamond
ND	Nanodiamond
NDAT	Acid Mixture Treated Nanodiamond
ND-BSA	Nanodiamond-Bovine Serum Albumin Complex
NDCMCS	Carboxymethyl Chitosan Modified Nanodiamond
NDNT	Nitric Acid Treated Nanodiamond
N Form	Normal Form
NHS	N-Hydroxysuccinimide
pI	Isoelectric Point
SPY	Sulfapyridine
SSZ	Sulfasalazine
SSMCC	sulphosuccinimidyl-4-(N-maleimidomethyl)cyclohexane-1-carboxylate
TGA	Thermogravimetric Analysis

Trp	Tryptophan
UDD	Ultradispersed Diamond
UV-Vis	Ultraviolet-visible Spectrum
XRD	X-ray Diffraction

CHAPTER 1

INTRODUCTION

1.1 Research Motivation

Recently nanodiamond particles (ND) have been attracting increasing attention in scientific community due to its excellent properties. ND features high specific surface area (*ca.* 300 m^2/g) which results from its small crystal size (*ca.* 5 nm), oxygen-containing surface groups which could be flexibly functionalized by physical or chemical approach, optical transparency, physically and chemically inert diamond cores as well as desirable biocompatibility [1]. It has been reported that ND nearly has no cytotoxicity to a variety of cells of different origins with ND concentrations up to 100 μg/ml [2, 3]. While other carbon nanomaterials, for example, carbon nanotube (CNT) and C60 exhibit cytotoxicity to different extents [4-9].

The development of new platforms for the immobilization of biologically active substances has been a very active research area [10]. The combination of nanotechnology with life science techniques has given rise to a newly emerging area Nanobiotechnology [11], which is largely based on the biomacromolecule immobilization since the biomacromolecule especially protein immobilization is a crucial step in biotechnology as well as biochip developments [12-14]. The excellent surface properties and biocompatibility might be able to render ND a promising platform for biomacromolecule immobilization.

However, the strong interaction between nanoparticles and biomacromolecules may cause structural changes in biomacromolecules [15, 16], which might bring about the loss of

biofunctionalities. Therefore it is essential to systematically study whether biomacromolecule could retain its structural features upon being immobilized onto ND surface. In terms of practical applications for biomacromolecule immobilization, it is highly desirable to have diamond material prepared in a thin fiber-like and/or film form [17], which suggests that it is important to develop techniques to assemble ND or ND-biomolecule complex into macroscale materials for the ease of application. In addition, the current research has been focusing on the immobilization of proteins [18-23], enzymes [24, 25], antibodies [26], and peptides [27] onto ND surface. Then a question is naturally raised: is it possible to immobilize other important biomacromolecule, such as polysaccharide, onto ND surface to further extend its applications?

The excellent surface properties make ND not only a desirable platform for biomacromolecule immobilization but also a potential adsorbent to address the current environmental issues. Other carbon materials, such as activated carbon (AC) and CNT, have been reported to be an effective adsorbent in contaminant adsorption. Compared with CNT, ND has similar high specific surface area, similar surface sp^2 bonded carbon, and similar flexible surface chemistry. Moreover, ND is lower in synthesis cost than CNT. Therefore, it is reasonable to investigate the feasibility of using ND as a contaminant removal adsorbent.

1.2 Research Objectives

The concerns and needs in the current and potential ND applications in the areas mentioned above necessitate further research to quell concerns and meet needs. The present Ph.D. project aims to address these concerns to meet the needs for ND applications. Specifically, the research

has following objectives:

(1) Identifying the feasibility of polysaccharide immobilization onto ND surface to improve its dispersibility for extended applications.

(2) Understanding ND-protein interaction mechanism as well as how this interaction affects the structural features of protein upon immobilization onto ND surface.

(3) Studying the assembly properties of ND and ND-protein complex to find a facile and economical way to fabricate ND coatings for biological applications.

(4) Identifying the feasibility of utilizing ND for addressing environmental issues especially for azo dye contaminant removal.

1.3 Thesis Organization

The present thesis comprises the following 8 Chapters:

Chapter 1 introduces a brief overview of the present Ph.D. project.

Chapter 2 gives a comprehensive and up-to-date literature review as well as background information on the related research topics.

Chapter 3 deals with polysaccharide immobilization onto ND surface, where the ND dispersity in aqueous medium is improved and further functionality is extended.

Chapter 4 focuses on protein conformation and adsorption behaviors in ND-protein complexes, where it is found most of protein structural features could be preserved upon immobilization onto ND surface.

Chapters 5 and 6 study the possibilities of assembling ND or ND-protein complex into films

on glass substrates, demonstrating that ND thin films could be prepared by Layer-by-Layer assembly (LBL) with potentials to be applied to biosensor area.

Chapter 7 investigates the feasibility and mechanism of utilizing ND for dye contaminant adsorption, where ND has been demonstrated to be an effective adsorbent for this application.

Chapter 8 concludes the present thesis with conclusions as well as suggestions for future work.

CHAPTER 2
LITERATURE REVIEW

2.1 Element Carbon and Its Allotropes

Element carbon is widely distributed in nature and of great importance, which is the basic constituent of all organic matter and a major element in the fixation of energy by photosynthesis [28]. Carbon-based products can be found everywhere in daily life: from the exhaust gas emitted out of vehicles to the priceless diamond jewelries.

A unique property that sets carbon apart from other elements lies in its diversity [28]. Carbon is actually the most versatile element in the periodic table [29]. Depending on how the carbon atoms are arranged, pure carbon has different allotropes (or polymorphs) [17] including diamond, graphite, amorphous carbon, fullerene, carbon nanotubes, and etc. They are entirely composed of carbon but exhibit different properties due to different structures. A good case in point is that graphite is soft and black due to the layered arrangement of carbon hexagons, whereas diamond is hard and transparent because of the fully covalent bonding among carbon atoms in 3-dimensional space [17].

2.2 Diamond

The word “Diamond” is often associated with jewelries which are the symbols of value and eternity (Figure 2.1). However, in scientific community, the “Diamond” refers to far more than jewelries.

Figure 2.1 Diamond as jewelry [30].

Diamond is mainly composed of sp^3 bonded carbon with a small fraction of sp^2 bonded carbon on surface or grain boundary. Each carbon atom is tetrahedrally coordinated to four other carbon atoms through sigma bonds with a bonding angle of 109°28' [31] (Figure 2.2). These symmetric and strong bonds endow diamond with excellent chemical stabilities as well as outstanding mechanical properties.

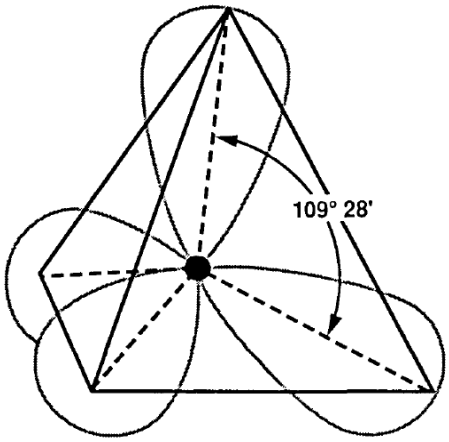

Figure 2.2 Diamond tetrahedron [28].

Originally, diamond is from nature. Even nowadays natural diamond still represents very high monetary value. Diamond was first synthesized from graphite by high-pressure/high-temperature (HPHT) methods in the 1950s, and low-pressure chemical vapor deposition (CVD) of diamond thin films was developed at the beginning of 1960s but not at an acceptable growth rate until

1981 [1]. Currently both HPHT [32, 33] and CVD [33, 34] are the major techniques for diamond synthesis. Diamond has many extreme properties. It is the hardest known natural material and has the highest thermal conductivity [28, 35]. Its sp^3 bonded carbon is extremely stable in terms of chemical and physical stabilities, which renders diamond material biocompatible in itself [36-39]. Moreover, diamond possesses very high wear resistance and very low friction coefficient [40, 41], excellent transparency [42, 43], and outstanding semiconductor property [44]. All those properties make diamond materials ideal for many applications including biosensors [26, 45, 46], biological interfaces [36, 47], abrasives [48], cutting tools [49], heat sinks [50], semiconductor devices [51], and electron emission devices [52].

2.3 Nanodiamond: Synthesis, Properties and Further Treatment

The nanotechnology has been undergoing rapidly exploding development in recent years which could find wide applications in a broad range of scientific areas [53-55]. Nanodiamond particles (ND) have recently come into focus as a new promising nanomaterial. Nanodiamond, as the name suggests, is diamond on nanometer scale, including nanoparticles, nanorods, nanocones, nanofibers, etc. Since it is diamond materials in nature, it possesses all the excellent properties as bulk diamond materials as well as new properties related to its nanostructure. The present research mainly deals with diamond nanoparticles. Therefore the term “nanodiamond” or “ND” will be used to refer to “diamond nanoparticle” for the sake of simplicity throughout the entire thesis.

2.3.1 Synthesis of Nanodiamond

ND could be synthesized by several methods. The simplest one is the milling technique. It begins with milling of synthetic or natural microdiamond and then after sorting out the remaining big particles a slurry of diamonds with a size below 100nm can be obtained [56, 57]. CVD technique could also be employed to produce nanodiamond and Frenklach *et al.* have reported on a substrate-free CVD for nanodiamond preparation in 1989 [58]. The resulting diamond particles are in a size range below 500 nm.

A large-scale alternative to produce ND is the shockwave method [59]. In this method, the graphitic material is mixed with copper for better heat transport. The generated shock wave compresses the inner tube containing the carbonaceous material, increasing pressure and temperature to transform graphite to diamond [59]. The resulting diamond consists of nanometer-scale primary crystals sintered together and covered with graphitic carbon [59].

Another technique for the large-scale production of ND particles is detonation synthesis (Figure 2.3). The first synthesis of detonation nanodiamond was reported by Titov and his collaborators in 1963 [60]. But the product prepared finally turned out to be extremely tight aggregates which was impossible to isolate and disperse. It was not until 2002 that Osawa and his colleagues made possible the dispersion of detonation nanodiamond in aqueous solution [61]. The detonation synthesis consists of placing an explosive charge into a detonation chamber and igniting it by another accelerator charge or electrically [62]. During this process, no additional carbon material is needed for the formation of diamond soot [62].

The detonation soot, produced by detonation process, contains up to 80% of diamond

nanoparticles as well as a variety of impurities, including metal and concrete debris from the reaction chamber and a significant amount of non-diamond carbon [62, 63]. After the first purification steps, the raw soot is collected and purified by acid treatment which not only further reduces the metal content of the material but also oxidizes the non-diamond carbon in the soot [62]. Due to the fact that the reactivity of sp^2 carbon, especially disordered graphitic material, towards oxidation is much higher than that of diamond carbon, it is therefore possible to selectively remove the sp^2 carbon so that the diamond content could be enriched [62]. The final nanodiamond product contains over 95% of carbon, with the rest being nitrogen (2%), hydrogen and oxygen as well as traces of iron and other metals [62].

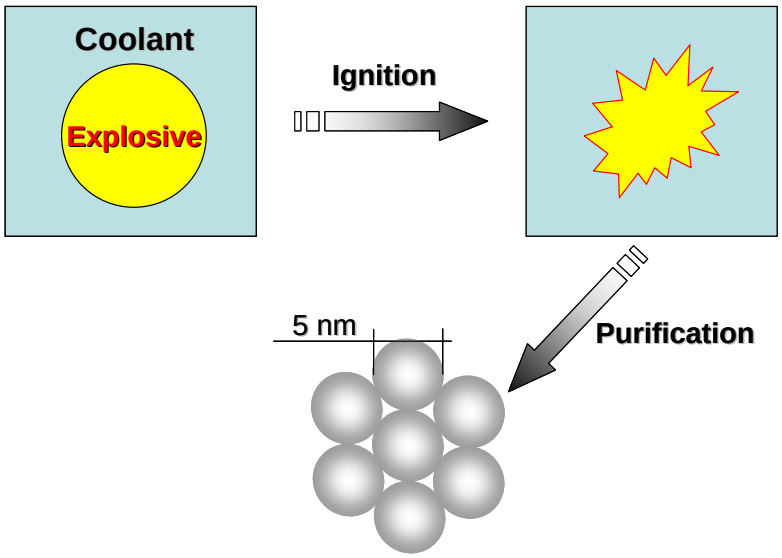

Figure 2.3 Synthesis of nanodiamond by detonation method.

2.3.2 The Merits of Detonation Method

The size of ND varies largely depending on different production methods. Among the four methods that produce ND, the milling technique produces ND with large size as well as widest

size distribution [62], and the CVD production method also generates diamond particles with relatively large size. For shock wave diamond, the size and size distribution depend on the granulometry of the original graphite material that is being compressed [62] and ND crystals are usually sintered together instead of forming isolated particles [62, 64].

For nanomaterials, the size distribution is very important factor since uniform physical and chemical properties of nanoparticles require narrow size distribution [65]. After oxidizing acid treatment to remove most of sp^2 carbon during the detonation nanodiamond synthesis process, there is still graphitic carbon present in the sample, giving rise to strong agglomeration among primary particles [64]. Several methods, including stirred-media milling with micron-sized ceramic beads [61], have been developed to yield completely de-agglomerated primary particles [64]. Therefore the detonation diamond is (also known as ultradispersed diamond, UDD) usually credited with single crystal size of around 5 nm as well as very narrow size distribution [1, 61]. Compared with NDs prepared by milling, CVD and shock wave methods, detonation nanodiamond has smaller particle size as well as narrow size distribution, which renders nanodiamond high in specific surface area and thus gives full play to the surface properties of ND as nanomaterials. According to the above discussion, detonation nanodiamond is chosen and used throughout this research.

2.3.3 Further Treatment of Synthesized Nanodiamond

2.3.3.1 The Needs for Further Treatment: Surface Properties of Synthesized Nanodiamond

The needs for the further treatment of ND originate from its surface properties after production.

Depending on different production methods, the surface of pristine ND particles shows distinctive features. The substrate-free CVD process of acetylene in a microwave-enhanced plasma oven produces hydrogen terminated diamond which cannot be synthesized by detonation or shock wave method [58]. The shockwave diamond has a graphitized surface. In case of detonation nanodiamond, oxygen containing groups are usually present on surface [61, 66] which are the results of the reaction of newly formed diamond crystallites with cooling medium in detonation reactor or from purification process using concentrated mineral acids [62]. Usually most of functional groups on detonation nanodiamond surface are carboxyls, hydroxyls, lactones, ketones and ethers [62], which provide possibilities for both non-covalent and covalent functionalization of detonation nanodiamond surface.

Besides the surface functional groups, there is a thin layer of graphitic carbon on nanodiamond surface. For detonation nanodiamond, the graphite layer accounts for approximately 5% of total ND mass even after oxidative acid treatment and for shock wave diamond the graphite layer content is even much higher [62].

The above discussion on the surface functional groups of ND suggests that nanodiamond surface includes both oxygen-containing groups (mainly carboxyl, hydroxyl, and etc.) and graphite layer. The presence of oxygen-containing groups facilitates the dispersity of ND in suspension while the graphite layer would result in strong agglomeration of particles [64]. The content of ND surface oxygen-containing groups varies depending on different production methods and manufacturers. In addition, ND surface might need to be further treated for different applications. Accordingly, the functionalization of nanodiamond is generally focused on how to

enhance the dispersity by increasing the oxygen-containing group content while reducing the graphite layer content or how to introduce new functional groups (by physical or chemical approach) to the diamond surface to facilitate the dispersion of ND and endow nanodiamond with new functionalities.

2.3.3.2 Treatment Utilizing Oxidization, Reduction, and Other Methods

In general, the methods for further treatment of nanodiamond include oxidization, reduction and others.

Oxidization is one of major approaches to modify ND surface properties. Among different oxidization methods, oxidizing acid treatment is one of the most frequently used and meanwhile very effective method giving rise to the immobilization of oxygen-containing groups (mainly carboxyls and hydroxyls) onto ND surface [67-72]. The oxidizing acid treatment can selectively oxidize the existing graphitic sp^2 carbon and remove metallic impurities [1] on surface. After oxidizing acid treatment, the ND surface is functionalized with carboxyl groups which can be further modified by means of chemical or physical method. Moreover, other oxidants (KNO_3 or $KClO_3$) could also be used as a means of oxidizing agent for ND [62].

Another effective approach to modify ND surface properties is the thermal oxidization treatment which oxidizes ND surface so that the oxygen-containing group content can be increased and therefore the dispersity is improved [73-80] since the thermal oxidization treatment under air or oxygen environment can eliminate sp^2 carbon species (mainly graphite and amorphous carbon) [78].

The thermal oxidization in the air followed by ultrasonic treatment could give rise to desirable dispersity of NDs in aqueous solution, as indicated by the research conducted by Shenderova and her colleagues [77]. However, during the thermal treatment, the bridge-forming bonds among ND particle surfaces may cause some agglomeration but in general the positive effect of highly improved dispersivity of ND due to high temperature oxidation outweighs the negative effect of bridge formation among ND particles [77].

For the treatment using reduction method, hydrogenated diamond could be obtained by reacting ND with hydrogen [81] while the reaction with borane creates hydroxyl groups on ND surface [69]. Besides oxidization and reduction reactions, ND could also react with various gaseous reactants, such as fluorine [82], ammonia [81] and chlorine [83], to yield the respective functionalized nanodiamond.

2.4 Nanodiamond for Biomacromolecule Immobilization

The term "Macromolecule" refers to "*A molecule of high relative molecular mass, the structure of which essentially comprises the multiple repetition of units derived, actually or conceptually, from molecules of low relative molecular mass*" [84]. "Macromolecule" covers a wide range of substances normally encompassing synthetic and naturally occurring macromolecules. In the scope of the present thesis work, focus is given to naturally occurring macromolecules (which could also be referred to as biomacromolecules, including proteins, polysaccharides, nucleic acids, and etc.) with special attention being given to proteins and polysaccharides.

2.4.1 Nanodiamond: A Good Platform for Biomacromolecule Immobilization

2.4.1.1 Biocompatibility of Nanodiamond

When it comes to biological applications, the biocompatibility of the material is an important factor to be considered. ND material is mostly made up of element carbon which is very similar to human body: carbon is one of major substituent elements of human body. Actually the biocompatibility of ND material has already been proved by previous research [1, 25, 30, 62, 64, 85, 86]. However, since the outermost layer of ND, as mentioned previously in Section 2.3, is composed of graphite layer and traces of heavy metals which might naturally cause a concern. The existence of heavy metal or other impurities, though in tiny amount, will pose potential risk for future biological applications of this material [2]. This concern is quite reasonable because it is not until recently people begin to realize that the thorough removal of metal (mainly iron) from detonation diamond is a more challenging task than thought before [62]. The metal content could only be removed by air oxidization followed by oxidizing acid treatment [73]. Fortunately, the research on the cytotoxicity of nanodiamond reveals that nanodiamond had no cytotoxicity to cells [2, 3] which lays a solid ground for further investigation on the biological applications of ND materials. On the other hand, other carbon nanomaterials, for example, carbon nanotube and C60 exhibit cytotoxicity to different extents according to previous research [4-9].

2.4.1.2 High Affinity with Biomacromolecules

Up till now there has been some work reporting on the high affinity of ND with

biomacromolecules such as proteins [18-23], enzymes [24, 25], antibodies [26], and peptides [27]. In these work, the nanodiamond-biomacromolecules prepared were subjected to different tests of their applicability in biological systems and it was shown that these complexes largely preserve the activity of the adsorbed biomacromolecules and that further functionalization is possible on existing functional groups.

Chang *et al.* [22] were among the first to investigate the affinity of ND toward protein biomacromolecules (cytochrome c). In their work [22], the adsorption isotherms of horse cytochrome c on NDs with sizes of 100 and 5 nm were studied in phosphate buffers at pH 6.5. They found that the cytochrome c adsorption isotherms showed very steep slope at low concentration ranges, indicating that the affinity between ND and cytochrome c is very strong. The adsorption behaviors of cytochrome c onto ND surface could be well fit by Freundlich model. In their following research, Chang's group [23] employed ND to concentrate and separate protein from dilute solution for mass spectrometric analysis. Adsorption isotherms of horse heart cytochrome c (HCC), horse heart myoglobin (Mb), and bovine serum albumin (BSA) on 100-nm diamonds were studied at pH 10.5, 6.9, and 4.7, respectively, where they also found high affinities between NDs and these proteins.

The above pioneering work on ND-protein interaction demonstrates the high affinity between ND material and biomacromolecules, which reveals its potentials for biomacromolecule immobilization applications.

In addition, the nanodiamond, especially the detonation nanodiamond, possesses high specific surface areas (due to small particle size and narrow size distribution) and the concomitant high

adsorption capability, significant amount of oxygen-containing functional groups on the surface, and chemically inert diamond cores [1]. All these properties render ND an excellent platform for biomacromolecule immobilization, which has been receiving ever-increasing attention.

Moreover, oxygen-containing groups on ND surface could be easily modified by physical or chemical method. The flexibility in the modification of oxygen-containing surface groups of ND might further open up more opportunities for biomacromolecule immobilization.

To sum up, ND has exceptional properties including high specific surface area, oxygen-containing functional groups on the surface, optical transparency, and highly chemically and physically inert sp^3 carbon (diamond) cores [1, 17, 30]. By virtue of its chemical and physical inertness, ND has excellent biocompatibility which has already been proved by many previous studies [30, 64, 87]. The research on the cytotoxicity of ND revealed that it has no cytotoxicity to cells while other carbon nanomaterials such as carbon nanotube and C60 exhibit cytotoxicity to different extents based on previous reports [3, 7]. All these properties make ND a good platform for biomacromolecule immobilization [88].

2.4.2 Nanodiamond with Biomacromolecules: Promising for Nanobiotechnology Applications

2.4.2.1 Nanodiamond is Promising for Nanobiotechnology Applications

The development of new platforms for the immobilization of biologically active substances has been a very active research area [10]. Recently, the combination of nanotechnology with life science techniques gives rise to a newly emerging area Nanobiotechnology [11], which is largely based on the biomacromolecule immobilization since the biomacromolecule especially protein

immobilization is a crucial step in biotechnology as well as biochip developments [12-14]. Presently, the platforms for biological substances immobilization have been focused on silica, gold, and iron oxide particles, glass surfaces, and cadmium chalcogenide quantum dots [10]. According to the above discussion, due to excellent properties such as high affinity and biocompatibility with biomacromolecules, high surface area, highly chemically and physically inert diamond cores, ND is promising to be new platform (substrate) material [10].

One previous work was led by Ushizawa *et al.* [68], where diamond powder (1-2 μm) surface was functionalized with deoxyribonucleic acid (DNA) through phosphatization of 5'-end from PCR products as well as hydrogen bonding between adenine and thymine residues (Figure 2.4). Their work demonstrated the feasibility for the immobilization of biologically active substance onto diamond surface which reveals the potential of utilizing diamond and ND for this application.

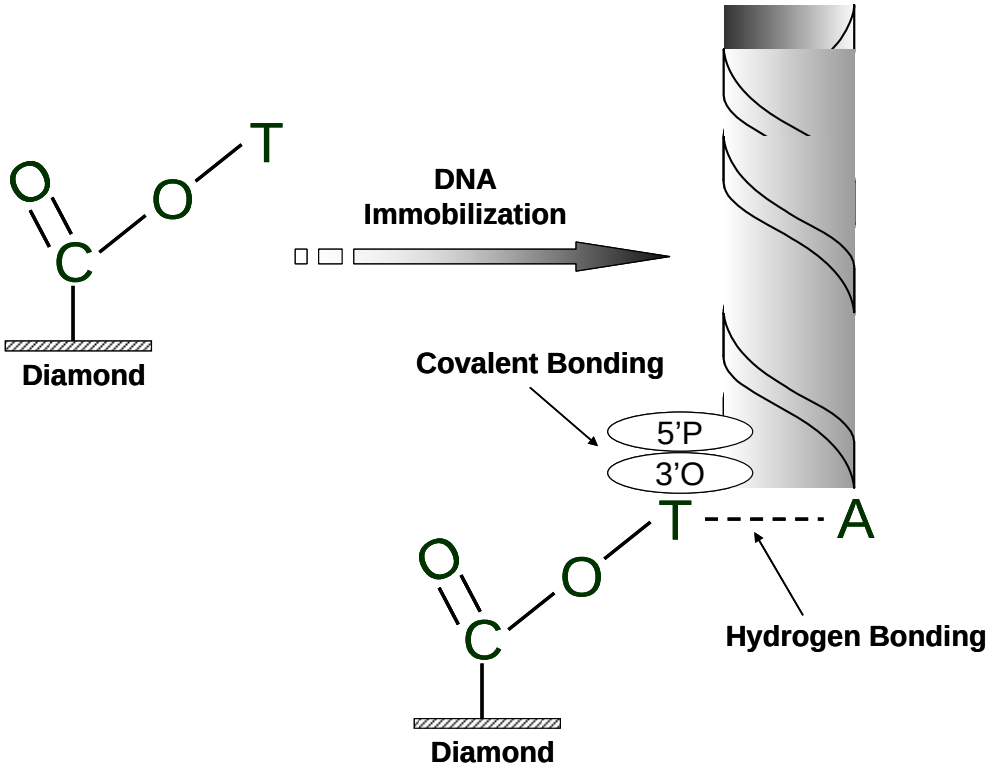

Figure 2.4 Immobilization of DNA onto diamond powder surface through ester linkage.

2.4.2.2 Current Nanodiamond Applications: Biosensor and Biolabel

Biosensor and biolabel applications are currently among the most studied fields in terms of ND applications. Chang *et al.* [23] employed acid-oxidized ND to concentrate protein dilute solution for mass spectrometric analysis. The high protein adsorption capability of ND greatly facilitates the detection process: proteins in dilute solution can be concentrated by NDs, and directly analyzed by matrix-assisted laser desorption/ionization time-of-flight mass spectrometry (MALDITOF-MS) after a simple centrifugation process.

The ability of ND to immobilize antibody for the purpose of detecting bacterial has been demonstrated in another research carried out by Tzeng *et al.* [26]. The immobilization of

anti-*Salmonella* and anti-*Staphylococcus aureus* antibodies on hydrogen or air plasma-treated ND, which is coated on a silicon substrate, gives rise to a greatly enhanced bacterial binding efficiency compared with ND samples without antibody immobilization.

In Puzyr *et al.*'s work [89], an "aluminum oxide film–adhesive layer–nanodiamond–luciferase" supramolecular structure has been prepared on an aluminum oxide substrate (Figure 2.5). The loading of light-emitting protein luciferase onto ND surface was achieved by adsorption method. It was found that the luciferase immobilized could retain its catalytic activity. They pointed out that the system proposed in their work could be applied to bioluminescent analysis.

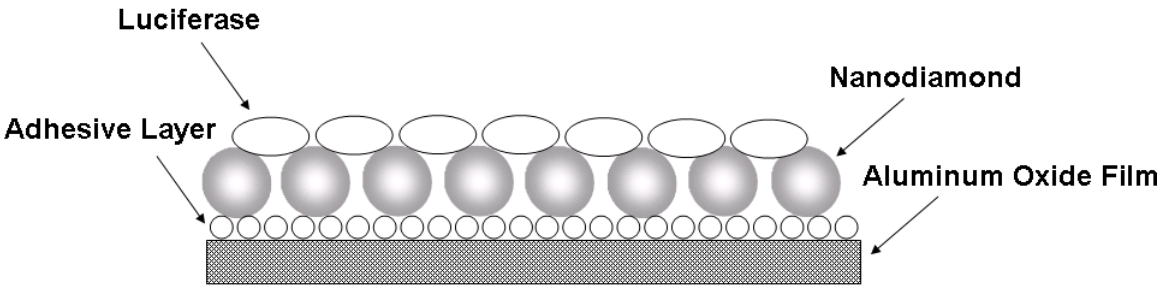

Figure 2.5 The proposed "aluminum oxide film–adhesive layer–nanodiamond–luciferase" supramolecular structure.

Besides the potentials to be applied in biosensor as well as related fields, ND is also a very promising material as biolabel. Extensive optical investigations have revealed that there are over 100 luminescent defects on diamond [90]. Among all these defects, the N-V center is one of the most studied [91-93], which consists of a substitutional nitrogen atom with an adjacent carbon vacancy [94]. The N-V defect can endow ND with interesting luminescence properties. In addition, it is possible to produce ND with different emission colors [95, 96]. Fu *et al.* [70] have carried out in vitro labeling experiments with covalently modified ND particles by a

biomacromolecule poly-L-lysine and they found that the photophysical properties of the particles do not deteriorate even after coating ND surface with poly-L-lysines that interact with DNA molecules through electrostatic forces. All these properties make the ND material a valuable alternative for other fluorescence labels.

2.4.3 Is It Feasible to Immobilize Polysaccharides onto Nanodiamond Surface?

Based on the above discussion on the immobilization of biomacromolecules onto ND surface, it can be seen that ND is a desirable platform for biologically active substances immobilization. Actually it has been reported that proteins [18-23], enzymes [24, 25], antibodies [26], and peptides [27] could be immobilized onto ND surface. However, there has been nearly no report on the immobilization of polysaccharide onto ND surface to modify its surface properties for further applications though polysaccharide is also an important biomacromolecule with great potentials for further functionalization.

2.4.3.1 Chitosan as a Promising Functional Biomacromolecule

The representative polysaccharides are chitin, cellulose, starch and etc. Chitin is the second abundant natural polymer in the world (only second to cellulose). It is not soluble in water, weak acid and weak alkaline. Chitosan is the deacetylation derivative of chitin. It has excellent biocompatibility, good hydrophilicity as well as desirable membrane-forming ability [97]. The molecular structure of chitosan is given in Figure 2.6.

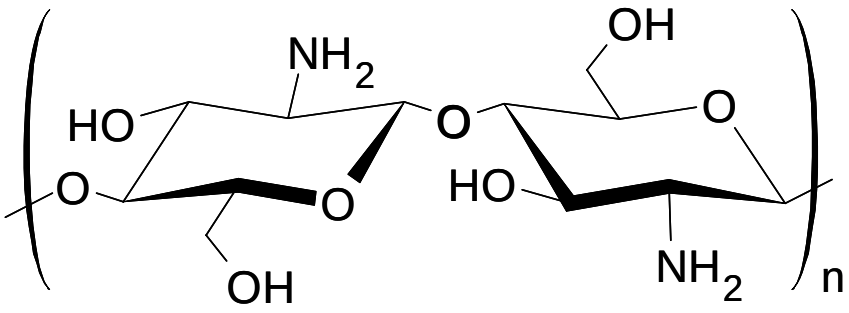

Figure 2.6 The molecular structure of chitosan.

Normally, the higher the degree of deacetylation, the more desirable the chitosan is for the further functionalization through physical or chemical method since the deacetylation process can generate primary amine group which is very active. However, totally deacetylated chitosan is very hard to obtain and actually the most widely used is partially deacetylated chitosan. Due to the rich content in primary amine and hydroxyl groups, chitosan is a desirable platform for further functionalization.

An important chitosan derivative is carboxymethyl chitosan (CMCS), which is among the most studied chitosan derivatives (Figure 2.7) [98]. CMCS is a water-soluble chitosan derivative which is biocompatible, either in vitro in fibroblast culture assays or in vivo in testing with intraperitoneal, oral, or subcutaneous treatments [99]. CMCS has been widely used for protein drug delivery [100-103] as well as surface functionalization of other materials for biological applications such as antibacterial coating [104, 105].

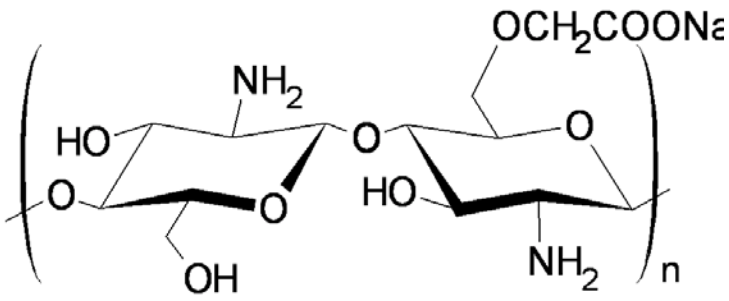

Figure 2.7 The molecular structure of carboxymethyl chitosan (CMCS).

2.4.3.2 Immobilization of Chitosan and Synthetic Polymers onto Carbon Nanomaterials

Though chitosan (derivatives) might be able to improve the dispersity of ND in aqueous medium and open up new opportunities for further functionalization of ND surface due to its rich primary amine and hydroxyl groups content, up till now there has been nearly no work reporting on using chitosan to modify the surface properties of ND or prepare ND/chitosan nanocomposites.

In contrast, for carbon nanotube (CNT), there have been several reports on the modification of CNT surface properties using chitosan by chemical or physical method [106, 107]. Moreover, a large number of work have investigated the properties of CNT/chitosan nanocomposites and electrodes, where mechanical and electrical properties of CNTs were applied [108, 109].

In Guan *et al.*'s work [106], low molecular weight chitosan (LMCS) was immobilized onto multi-walled carbon nanotube (MWNT) surface by nucleophilic substitution reaction (Figure 2.8). Though the synthesized product MWNT-LMCS has a LMCS content as high as *ca.* 58% and LMCS is water soluble, the MWNT-LMCS was found to be water insoluble while it is soluble in some organic solvents (Table 2.1) as MWNT. LMCS is insoluble in organic solvents but the

synthesize product MWNT-LMCS is soluble. These findings indicate that the CNT surface is not totally and tightly covered by biomacromolecule LMCS and MWNT-LMCS might have similar surface properties as CNT surface. This further suggests that the nucleophilic substitution reaction used in their work might not be a very effective approach for biomacromolecule immobilization. Moreover, the MWNT-LMCS synthesis procedure is complicated and time-consuming and it involved the use of thionyl chloride which is a very toxic and dangerous chemical (thionyl chloride could react violently with water). Therefore, the synthesis procedure is not environmental friendly.

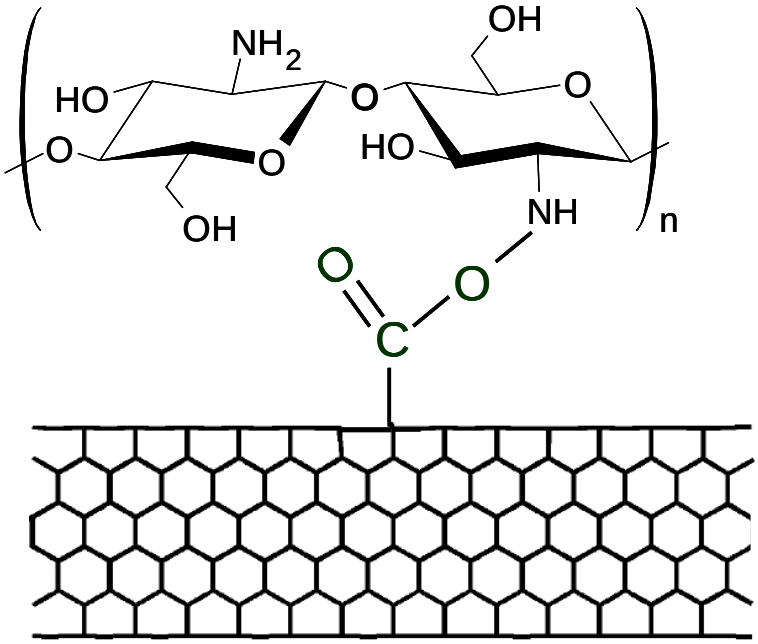

Figure 2.8 Schematic illustration of the immobilization of low molecular weight chitosan onto carbon nanotube surface.

Table 2.1 Dispersibility of LMCS and MWNT-LMCS in Different Solvents [106].

Solvents	LMCS	MWNT-LMCS
distilled water	+	—
hydrochloric acid [b]	+	—
acetic acid [c]	+	+
dimethylsulfoxide	—	+
N,N'-dimethylformamide	—	+
N,N'-dimethylacetamide	—	+

[a] Dispersibility: +, dispersible; —, not dispersible. [b] Hydrochloric acid: 1-35 wt% aqueous solution.

[c] Acetic acid: 10-95 wt% aqueous solution.

In Liu *et al.*'s work [107], CNT was dispersed into chitosan acetic acid solution and the addition of diluted ammonia into the suspension gave rise to the deposition of chitosan onto CNT surface due to deionization of chitosan. This is a physical method and thus the chitosan on CNT surface might not be very stable. Actually they used glutaraldehyde to crosslink the chitosan coating to make it stable but the glutaraldehyde tends to introduce high molecular weight aggregates into the system if its concentration is not properly controlled.

Though no work has touched the immobilization of chitosan onto ND surface, there have been several reports on introducing synthetic polymers onto nanodiamond surface. Cheng *et al.* [110] anchored the ABC-type block copolymer of tert-butyl methacrylate (tBMA), glycidyl

methacrylate (GMA), and styrene onto the carboxylated ND surface. After the modification with polymer, ND with V-shaped surface polymer structure could be self-assembled on oil-water interface to form stable ultrathin films. In Lukehart *et al.*'s work [111], the hydrophobic poly(tert-butyl methacrylate) polymer brushes could be introduced onto ND surface through atom transfer radical polymerization (ATRP). After acid hydrolysis of poly(tert-butyl methacrylate), hydrophilic poly(methacrylic acid) polymer brush was generated on ND surface.

2.4.3.3 A Facile Approach for Chitosan Immobilization

As discussed above, in Guan *et al.*'s work [106], the MWNT-LMCS synthesis procedure was complicated and time-consuming and it involved the use of thionyl chloride which is a very toxic and dangerous chemical (thionyl chloride could react violently with water). Therefore, the synthesis procedure is not environmental friendly. Moreover, the immobilization of LMCS did not improve the dispersibility of CNT in aqueous medium (Table 2.1). For physical immobilization of chitosan as in Liu *et al.*'s work [107], the coating might not be stable since it is only physical adsorption and a further crosslinking procedure is needed which increases the risk of forming aggregates among modified CNTs.

ND surface features oxygen containing groups such as carboxyls and hydroxyls. For many biomacromolecules such as chitosan, they possess abundant content of primary amine groups. Therefore, the conjugation of carboxyl/hydroxyl with primary amine might be an effective approach for immobilization of these biomacromolecules. The zero-length crosslinking agent 1-(3-Dimethylaminopropyl)-3-ethylcarbodiimide hydrochloride (EDC) is able to be applied to this

end. EDC is a water-soluble carbodiimide which is widely used to activate carboxyls for coupling with primary amines to form amide bondings [112-114]. More importantly, it is a non-toxic crosslinking agent and as a result its crosslinking process is biocompatible [115, 116], which is desirable for biological applications.

In the present thesis work, the feasibility of using EDC chemistry to immobilize chitosan derivative onto ND surface has been studied. This work might contribute to enhancing the dispersity of ND in aqueous medium and opening up new opportunities for further functionalization of ND surface due to rich content of primary amine and hydroxyl on chitosan backbone (Chapter 3).

2.4.4 Is Biomacromolecule "Safe" upon Immobilization onto Nanodiamond Surface?

The combination of nanotechnology and biotechnology gives rise to a newly-emerging interdisciplinary field: nanobiotechnology [117]. The nanobiotechnology, which incorporates the unique properties of biomacromolecules (recognition, transport, and catalytic properties, etc.) with those of nanoparticles (electronic, photonic, catalytic properties, and etc.), is playing increasingly important role in biological applications [117]. Since the combination of nanomaterial and biomacromolecule needs to immobilize biomacromolecule onto nanomaterials surface, there might be a reasonable concern: Could biomacromolecule retain its biological activity or structural features upon being immobilized onto nanomaterial surface?

Biomacromolecules have been immobilized onto nanoparticles through a variety of techniques including covalent coupling and physical adsorption by noncovalent interaction such as

hydrophobic interaction, electrostatic binding, and specific recognition [117]. The noncovalent method is especially applicable to ND materials whose surface could be terminated with carboxyl groups or other oxygen-containing groups for the interaction with the amino groups of proteins [22].

ND shows high affinity with biomacromolecules such as proteins [18-23], enzymes [24, 25], antibodies [26], and peptides [27], which indicates that it is an exceptional platform for biomacromolecule adsorption and immobilization [22]. This property makes it promising for many biological applications including biosensors [26] and diagnostic tools in clinical proteomics research [88]. However, the strong interaction between nanoparticles and biomacromolecules may cause structural changes in biomacromolecules [15, 16]. In order to understand the protein adsorption mechanism and identify optimal conditions to preserve functionality of protein following protein immobilization on ND surface, it is necessary to investigate the conformation of protein upon binding with nanodiamond [15, 118]. But there has been no systematic investigation in this regard so far [22]. Therefore, part of the present thesis work has been focused on the systematic investigation of whether protein could retain its structural features upon being immobilized onto ND surface (Chapter 4).

2.5 Assembly of Nanodiamond-Biomacromolecule Complex

As discussed in Section 2.4, ND has been proved to be an excellent platform for biomacromolecule immobilization which renders it promising for applications such as biosensor. However, for practical applications, it is highly desirable to have diamond material prepared in a

thin fiber-like and/or film form [17], which would make the material more easier to handle. Therefore, it is essential to assemble nanodiamond-biomacromolecule into macroscale material for specific application. Actually Eugenii Katz and Itamar Willner have indicated in their work that *"The integration of biomolecule–nanoparticle hybrid systems with surfaces paves the way for the generation of ordered architectures with new functionalities"* [117].

The functionalization of nanoparticles with biomacromolecules could give rise to nanoparticle-biomacromolecule interactions and then to self-assembly [117]. Therefore, by making use of this property, one could assemble nanoparticle-biomacromolecule complex into macroscale materials, where the ultimate control over the properties of a bulk system could be achieved [119, 120]. In addition, biomacromolecules (such as antibody/antigen, enzymes, and etc.) normally possess unique recognition and catalytic properties. Then the nanoparticle-biomacromolecule complex might be able to transduce biological phenomena to electronic or optical signal (depending on the properties of nanoparticles) which is promising for biosensor applications [117].

2.5.1 Merits and Demerits of Using Diamond Thin Films for Biomacromolecule Immobilization

Recently diamond thin films have been attracting considerable attention as substrate materials for the immobilization of biomacromolecules. Yang *et al.* [121] were the first to immobilize DNA molecule onto nanocrystalline diamond thin film surface. They introduced a long-chain amine onto H-terminated diamond film surface and then thiol-modified DNA was immobilized through crosslinker. They have demonstrated that nanocrystalline diamond thin film as a

substrate for DNA immobilization has superior properties to those of other commonly used substrate materials such as glass, gold or silicon in terms of stability and sensitivity [121].

As mentioned previously, diamond material is biocompatible in itself [36-39] and diamond thin film is of no exception [37, 121]. Moreover, diamond thin films could possess excellent electrical properties by doping method [122-125]. For diamond thin film deposition, the chemical vapor deposition (CVD) technique is currently the most widely used approach [126], which is able to deposit large-area thin films of nanocrystalline diamond (NCD) on substrates [37]. Due to good biocompatibility, chemical inertness, and excellent electrical properties [121, 127] of nanocrystalline diamond thin film, in recent years an increasing research interest has been focused on using diamond thin film material as a substrate for biomacromolecule immobilization [22, 26, 37, 45, 46, 121, 128].

However, the CVD film deposition process requires specialized and costly instrument [17, 129]. In addition, the substrate used for diamond thin film deposition needs to be able to resist high reaction temperature which limits the choice of substrates [129]. In view of these limitations in CVD technique, it is necessary to develop a more economic and facile alternative approach utilizing mild reaction conditions for biomacromolecule immobilization instead of using CVD diamond thin films as substrate materials.

2.5.2 Layer-by-Layer (LBL) Assembly Technique for Thin Film Preparation

A promising alternative for thin film preparation is Layer-by-Layer (LBL) assembly technique, which has been widely used for the preparation of polyelectrolyte multilayer thin films [130-132].

The pioneering work in this field was initiated by Decher *et al.* for the Layer-by-Layer (LBL) assembly of polyelectrolyte multilayers [130, 133-135]. The LBL assembly approach they proposed for the preparation of polyelectrolyte multilayer thin films is given in Figure 2.9.

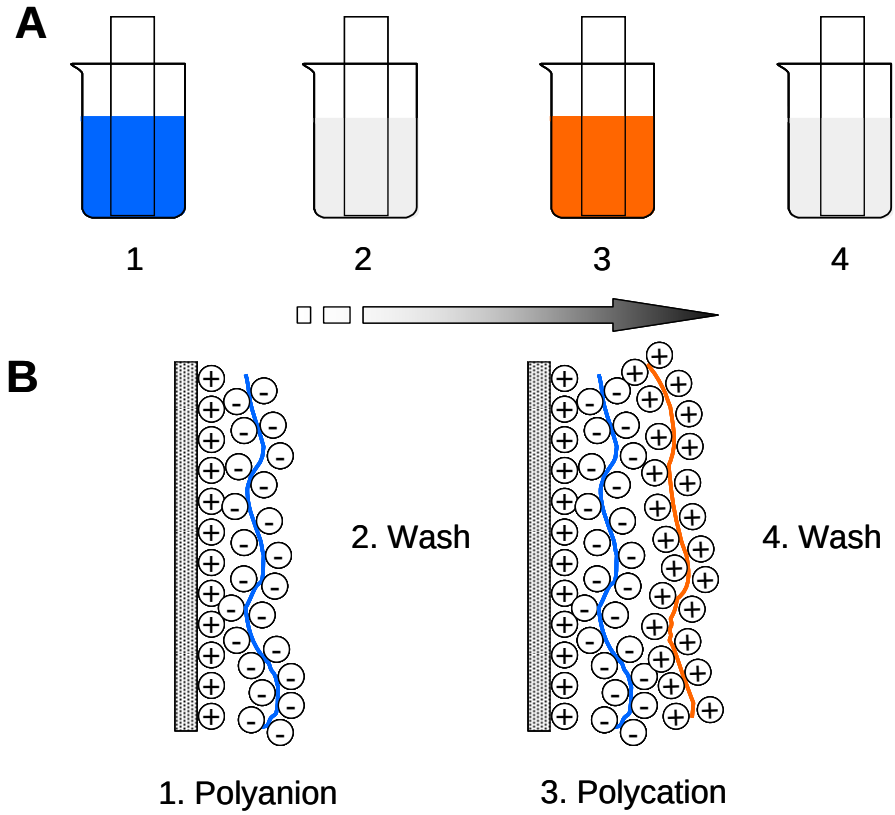

Figure 2.9 A. Steps 1 and 3 represent the adsorption of a polyanion and polycation, respectively, and steps 2 and 4 are washing steps; B. Simplified schematic illustration of the alternating adsorption of polyanion and polycation onto substrate.

During the LBL assembly process, polyelectrolyte multilayer films are formed by the alternating adsorption of polycations and polyanions, through electrostatic attraction, onto charged substrates. The film surface charge inversion during each adsorption step limits each layer thickness and prepares the surface for the subsequent adsorption of the oppositely charged polyelectrolyte [136]. The merits of LBL assembly technique lie in its simplicity and the control

over coating thickness, composition, and morphology which can be obtained at nanometer length scale [136].

Moreover, Decher has pointed out in his work that *"Layer-by-layer assembly by adsorption from solution is a general approach for the fabrication of multicomponent films on solid supports"* [130]. The materials that could be used for LBL assembly can be extended to a pool of small organic molecules, polymers, natural proteins, inorganic clusters, clay particles, and colloids [130].

2.5.3 Assembly of Nanodiamond into Macroscale Materials

In the family of carbon nanomaterials, LBL assembly technique has been widely applied to the fabrication of multilayer thin films of CNTs [119, 137-141], among which CNTs have been reported to be able to assemble into films on its own [137, 138] or with biomacromolecules as well as polyelectrolytes carrying opposite charges [119, 139-141]. For ND, up till now there has been some work reporting on the preparation of ND thin films through LBL assembly method. For instance, previous studies have demonstrated the feasibility of assembling ND with (bio)macromolecules into thin films [19, 142-146].

In Ho *et al.*'s work [19], ND was assembled with positively charged poly-L-lysine in an LBL fashion to form a packed nanodiamond multilayer films (Figure 2.10). Actually the high affinity between ND material and poly-L-lysine has been previously reported by Chang *et al.*'s work [22]. Chang *et al.* believe that the interaction involved is the electrostatic attraction between the surface-terminating anionic groups ($-COO^-$) of ND and the positively charged amine groups

(-NH_3^+) of poly-L-lysine [22]. In addition, they further indicated that ionic hydrogen bonding can also form between -NH_3^+ and ND oxygen-containing surface groups (such as carbonyl) as evidenced by previous research [147].

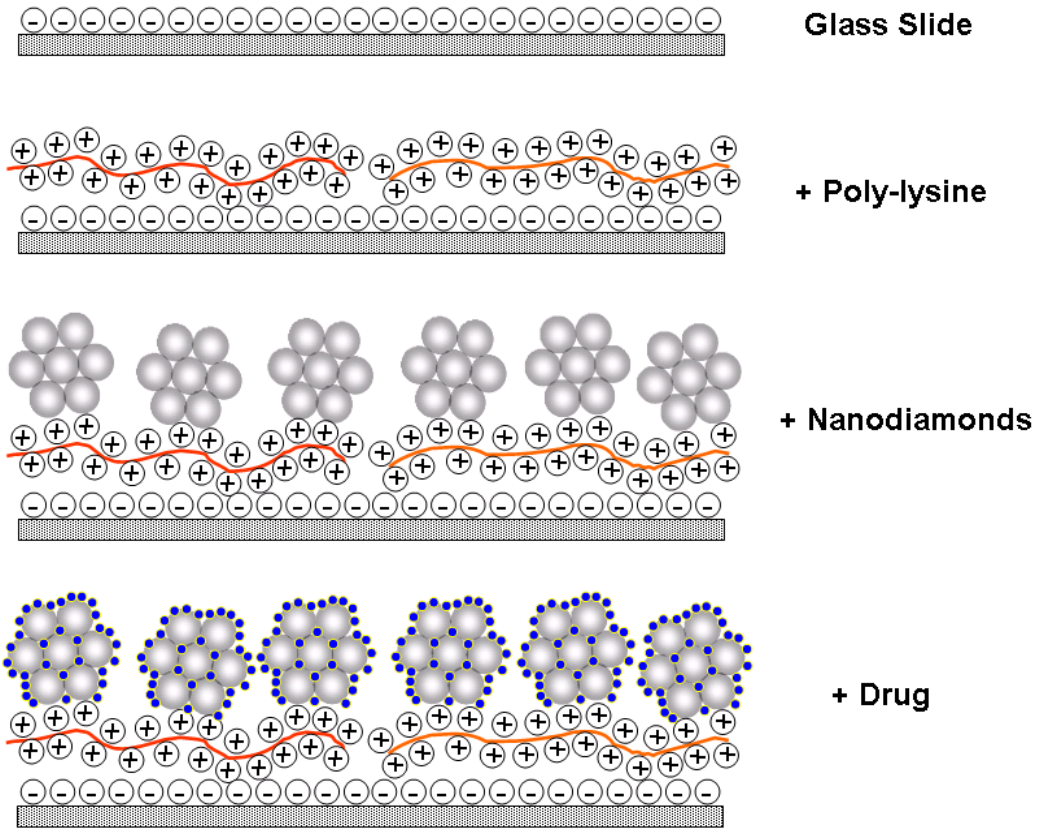

Figure 2.10 Schematic illustration of the nanodiamond nanofilm preparation process.

The LBL films prepared could load and then release therapeutic molecule dexamethasone (Dex) in a sustained manner [19]. They assessed basal cytokine secretion levels and found unchanged cellular inflammatory responses which proved the biocompatibility of ND as well as the feasibility of using ND for drug delivery applications [19].

There also has been some work reporting on assembling NDs into films by chemical or physical approach. Halas *et al.* [129] has assembled fluorinated ND monolayer onto glass surface

via wet chemistry approach but only one layer of ND could be deposited in Halas's work. Their ND coating process requires high temperature (130 °C) and long reaction time (24-40 h) [129]. Moreover, fluorination of ND powder involves toxic reaction atmosphere (fluorine gas) [82]. In another work, Dai *et al.* [17] and Terranova *et al.* [148] assembled ND into macroscale materials by drying an ND aqueous dispersion or slurry on substrates at certain temperature. Dai *et al.* [17] suggested that the hydrogen bonding among NDs could be a major force accounting for the ND film assembly in their work.

According to the above discussion, ND thin film coating could be prepared by assembling NDs and macromolecules or assembling NDs through physical or chemical approach. For assembling ND and biomacromolecule into films as in Ho *et al.*'s work [19], it might be necessary to further investigate if the biomacromolecule, such as protein, could be assembled with ND into films and meanwhile retain its structural features on the assembled ND films. If the answer is "yes" then the application of this ND/biomacromolecule film might be able to extend to other areas such as biosensor. For assembling NDs into films through hydrogen bonding as in Dai *et al.*'s work [17], LBL assembly technique might be able to be introduced to flexibly control the film thickness and morphology during film preparation process. Therefore in the present thesis work, further attempt has been made to study the feasibility and film growth mechanism of assembling NDs into films through ND-protein interaction (Chapter 5) as well as hydrogen bonding (Chapter 6).

2.6 Nanodiamond for Dye Contaminant Adsorption

In the discussions of the above sections, it could be seen that ND has excellent surface

properties (high specific surface area and oxygen-containing surface groups, etc.) for physical or chemical immobilization of biomacromolecules. Its excellent surface properties might also be able to be applied to addressing the current environmental issues as an effective adsorbent.

2.6.1 Dye Contamination Issues and Dye Wastewater Treatment

Recently, environmental issues have been attracting increasing attention worldwide and dye contamination issue is one of them. Many industries such as textile, paper and leather treatment are consuming a substantial amount of dyes and water, and generating a large amount of colored wastewater [149, 150]. Therefore, dye contamination has been a serious problem, posing health and environmental issues around the world [150]. The textile industry represents a major component of the world economy, accounting for 60% of world dye consumption and it has been estimated that 10~20% of water-soluble dye is lost during the dyeing process and released as an effluent [151]. Due to increasingly stringent restrictions on the organic content in industrial effluents [152], it is essential to remove dyes from wastewater. However, the dyes in wastewater are difficult to treat since they are recalcitrant organic molecules, resistant to aerobic digestion, stable to light, heat and oxidizing agents [153].

For dye wastewater treatment, there have been some approaches developed to this end including physical, chemical, and biological decoloration methods but few of them has been proved to be effective in textile industries [154]. With technical advancement, adsorption method has been standing out as an effective approach for decoloration [150, 155]. Compared with physical, chemical, and biological decoloration methods, adsorption gives better dye removal

results since it shows versatility being able to remove different types of coloring materials [150, 155, 156].

2.6.2 Carbon Materials as Adsorbents for Environmental Applications

Presently some adsorbents have been reported to be effective for decoloration, including activated carbon [157-159], biosorbent [160, 161], clay materials [162, 163], and etc. So far activated carbon (AC) has been demonstrated to be the most effective adsorbent for decoloration and actually it is currently the most widely used adsorbent for water treatment [150].

In recent years nanotechnology has been undergoing an exploding development which could find wide applications in a broad range of scientific areas [1, 164]. The large specific surface area of nanomaterials renders them attractive for adsorption of a variety of chemicals [165-167]. Correspondingly, carbon nanomaterial has been emerging as a new and promising route to address the current environmental issues [168], among which carbon nanotube (CNT) has been proved to be a desirable adsorbent for environmental applications. For instance, CNT has been studied for its potential application in removing organic [169, 170] and biological contaminants in water treatment [171, 172]. In addition, there have been reports on using CNT for metal contaminants removal [173, 174].

As adsorbents for environmental applications, carbon nanomaterials (such as ND and CNT) have an essential difference with AC in terms of surface area. Since both ND and CNT have non-porous structure, their specific surface area totally relies on the exterior surface of particles (or tubes) instead of the inner surface of pores. While the high specific surface area of AC is

mainly attributable to its inner surface area of pores. The pore structures of AC could be subjected to damage or blockage during adsorption or modification process if the adsorbate or the molecule for modification has high molecular weight [175-177]. In case the pore structure of AC is damaged or blocked, its efficiency as an adsorbent would be definitely compromised since specific surface area suffers from pore damage or blockage. Moreover, the high porous structure makes the mass transfer during adsorption process even longer, due to the fact that molecule has to move from the exterior to the inner surface of pores [178]. Therefore, ND and CNT might be better choices over AC as adsorbents in some environmental applications.

Actually, in some previous work, CNT has been found to have better performance over AC in contaminant adsorptions such as dioxin [179], fluoride [180], and trihalomethanes [178]. The AC has a specific surface area of up to *ca.* 1000 m^2/g [178] while for ND and CNT their specific area is normally below 500 m^2/g. The better performance of CNT over AC suggests that the exterior surface might be able to be more fully utilized than interior surface and CNT (or ND) could be very efficient adsorbent materials.

However, carbon nanomaterials, especially CNTs, are normally expensive, which hampers their practical applications [181]. Despite high synthesis costs, the cost effectiveness of single-walled and multiwalled CNTs over AC in contaminant adsorption has recently been demonstrated by Lu *et al.*'s work [182]. The synthesis cost for ND is much lower than that of CNT, which further suggests that ND also has potentials to be a cost-effective adsorbent material.

2.6.3 Nanodiamond as a Newly-emerging Adsorbent Material

As a newly-emerging carbon nanomaterial, ND particles possess some exceptional properties including high specific surface area, oxygen-containing surface functional groups, and highly chemically and physically inert sp^3 carbon (diamond) cores [1, 17, 64], which are desirable for adsorption applications. According to discussion in previous sections, the research on ND-biomacromolecule interaction shows that ND has high affinity with proteins [18, 19, 22, 88, 183, 184], enzymes [24, 25], antibodies [26] and peptides [185], which indicates that ND is an exceptional platform for biomacromolecule immobilization [22]. The high affinity between ND and biomacromolecules also implies that ND holds great potentials for biological contaminant removal.

Compared with the research on the adsorption of biomacromolecules onto ND surface, the work on adsorption of organic molecules such as dye molecules with ND is rather limited [186]. Gibson *et al.*[186] demonstrated that ND had high affinity to fluorescence dyes through electrostatic interaction, suggesting that ND could be a good platform for fluorescence dye adsorption. However, the fluorescence dye molecule adsorption in their work was largely driven by electrostatic force instead of other specific ND-dye interaction since they found positively (negatively) charged ND could only effectively adsorb anionic (cationic) dyes. Therefore, a question is naturally raised: could there be any other strong specific interaction(s) involved between ND and dye molecules?

In the present thesis work, the mechanism accounting for the adsorption of azo dye molecules onto ND surface has been studied, which has demonstrated the effectiveness and potentials of using ND in dye wastewater treatment (Chapter 7).

CHAPTER 3

FUNCTIONALIZATION OF NANODIAMOND PARTICLES WITH *N,O*-CARBOXYMETHYL CHITOSAN

Part of this chapter has been published in *Diamond and Related Materials*:

Wang H.D.; Yang Q.; Niu C.H. Functionalization of nanodiamond particles with *N,O*-carboxymethyl chitosan. *Diamond Relat. Mater.* **2010**, 19, 441-444.

Contribution of the Ph.D. Candidate

Under the guidance of Prof. Yang and Prof. Niu, Hai-Dong Wang designed and conducted the experiment for this chapter as well as prepared manuscript for publication.

3.1 Introduction

This chapter is aiming to enhance the dispersibility of ND in aqueous medium and open up new opportunities for further functionalization of ND through immobilization of polysaccharide *N,O*-carboxymethyl chitosan (CMCS) onto ND surface. CMCS is a water-soluble and biocompatible chitosan derivative desirable for biological applications [99, 104]. It is rich in primary amine and hydroxyl which renders it easily modified by physical or chemical approach [104, 105].

In this work, the functionalization of ND with CMCS has been successfully achieved and the NDCMCS thus obtained was found to have different properties compared with its ND

counterpart in terms of chemical composition, surface and crystalline properties. The functionalization with CMCS improves the dispersity of ND especially in low and high pH aqueous solutions. Moreover, the rich content of primary amine and hydroxyl on CMCS backbone would make further physical or chemical functionalization of ND more flexible and versatile. The approach described in this chapter is facile and environmental friendly. To the best of our knowledge, this work is the first report on the functionalization of ND by polysaccharide.

3.2 Materials and Methods

3.2.1 Materials

Nanodiamond (ND) particles with an average crystal size of 3-5 nm were purchased from Nanostructured & Amorphous Materials, Inc. They were produced by detonation method. Chitosan (degree of deacetylation: *ca.* 80%, molecular weight: *ca.* 1.0×10^5 Da) was purchased from Sigma-Aldrich. All other chemicals and reagents are of analytical grade.

3.2.2 Oxidizing Acid Treatment of ND

For the treatment using H_2SO_4-HNO_3 acid mixture, the ND powder (0.5 g) was dispersed into 25 ml of concentrated H_2SO_4-HNO_3 mixture (9:1, vol/vol) with the aid of ultrasonic treatment and stirred at 60 °C for 24 h. The acid mixture treated ND (NDAT) was then extensively rinsed with DI water until the supernatant reaches neutral. The final product (NDAT) was dried at 70 ^{o}C to dryness.

For the treatment using only nitric acid, the ND powder (0.5 g) was dispersed into 25 ml of

concentrated HNO_3 solution with the aid of ultrasonic treatment and stirred at 60 °C for 24 h. The nitric acid treated ND (NDNT) was then extensively rinsed with DI water until the supernatant reaches neutral. The final product (NDNT) was dried at 70 ^oC to dryness.

3.2.3 Synthesis of NDCMCS

The synthesis of CMCS was modified from literature reports [101, 187, 188] and the product was characterized by FT-IR to confirm the structure. The synthesis procedure is as the following: 3.9 g of NaOH was dissolved in 30 ml of isopropyl alcohol/water (4:1, v/v) mixed solvent. After the total dissolution of NaOH, 3.0 g of chitosan (CS) was added with agitation. The mixture was then agitated at 30 ^oC for 8 h, which was followed by the addition of 6 g of monochloroacetic acid (dissolved in 7.5 ml of isopropyl alcohol) in 20 min. After that the reaction mixture was agitated at 30 ^oC for another 4 h. The white-colored product was stirred with a large amount of absolute ethanol overnight. The product was then dissolved in deionized water and the non-soluble was removed by centrifugation. After being precipitated by absolute ethanol, the product was repeatedly stirred with ethanol/water (4:1, v/v) mixture. The final product (CMCS) was precipitated by absolute ethanol and then dried at 65 ^oC overnight.

The CMCS synthesized was then chemically immobilized onto the surface of the pristine ND particles using zero-length crosslinker 1-(3-Dimethylaminopropyl)-3-ethylcarbodiimide hydrochloride (EDC). The synthesis process is detailed as follows: 0.5 g of CMCS was dissolved in 20 ml of 2-(N-Morpholino) ethanesulfonic acid (MES) buffer (pH 6.7). 0.15 g of pristine ND particles was dispersed in 30 ml of MES buffer (pH 6.7). After total dispersion of ND in the

solution with sonication (Branson 2510), 0.345 g of N-Hydroxysuccinimide (NHS) was added which is followed by the addition of 0.288 g of EDC. After adjusting solution pH to 6.5 by 1.0 M NaOH, the solution was agitated at 4 ^{o}C for 30 min. The two solutions were then mixed and subjected to ultrasonic treatment for better dispersion. The reaction mixture was agitated at 4 ^{o}C for another 12 h and then the product NDCMCS was centrifuged and rinsed repeatedly with deionized water which was refreshed every 12 h until the supernatant after centrifugation approaches neutral.

To confirm the introduction of CMCS onto ND surface, several techniques were used for characterization of samples before and after modifications. FT-IR spectrum was recorded on a JASCO FT/IR-4100 spectrometer by KBr method (KBr:Sample=100:1, mass ratio). The pHs of different ND suspensions were measured on a Schott Automatic Titrator (Schott Instruments). Each measurement was performed in triplicate with the data presented being the average. Thermogravimetric analysis (TGA) was performed on a PerkinElmer TGA instrument in argon atmosphere with flow rate of 60 ml/min. Samples were heated from *ca.* 25 ^{o}C to 520 ^{o}C at a rate of 10 ^{o}C/min. Raman analysis was carried out on a Renishaw inVia Raman microscope with excitation wavelength at 514 nm. Zeta-potential was measured on a Malvern Zetasizer Nano ZS instrument over a pH range approximately from *ca.* 7.5 to 1.5 and the pH of solutions was adjusted by an autotitrator using HCl and NaOH aqueous solutions. After reaching the desired pH by titration, the solution was left to equilibrate for 1 min before taking measurement. Each measurement was performed in triplicate with the data presented being the average. X-ray diffraction (XRD) analysis was carried out on a Rigaku Rotaflex RU-200 diffractometer with a

Cu Ka radiation source and the scanning rate is 2 ^{o}/min.

3.3 Results and Discussion

3.3.1 Oxidizing Acid Treatment of ND

The ND used in the present work was produced by detonation method and the detonation soot is normally subjected to oxidizing acid treatment to remove metallic impurities as well as graphite layer on ND surface [64]. However, the composition and surface properties of ND products vary depending on treatment conditions, suggesting that the surface state of NDs might be different depending on manufacturers. Therefore, a further oxidizing acid treatment was carried out on pristine ND in the present work to evaluate its influence on the properties of ND and to determine if this further oxidizing acid treatment is necessary.

The treatment of ND with oxidizing acid is a common way to create oxygen-containing groups (carboxyls and hydroxyls) on ND surface in order to improve its dispersity in aqueous solutions and provide reactive groups for further functionalization. Upon the strong oxidizing acid treatment, the graphitic sp^2 carbon on ND surface is selectively oxidized and meanwhile metallic impurities are removed [1]. After the oxidizing acid treatment, the oxygen-containing groups thus generated could be further modified by means of chemical or physical approach.

In the beginning of experiment, mixture of concentrated sulfuric acid and nitric acid was used to treat ND by the method similar to previous literature reports [67-72]. The pristine ND in the present research is gray-colored fine powder and is produced by detonation method. However, after the acid mixture treatment the product (NDAT) becomes dark black-colored aggregate

which is not as easily “soluble” in aqueous medium as pristine ND. This phenomenon might be explained as the following: the already-existing oxygen-containing groups on the ND surface, for example carboxyl and hydroxyl groups, could be dehydrated by conjugating with each other because of the fact that the concentrated sulfuric acid is a very strong dehydrating agent. Therefore, the “bridges” among ND particles are formed which could account for the aggregated form of the product obtained by oxidizing acid mixture treatment. Similar findings were reported when air oxidizing method was applied to ND in an attempt to oxidize ND surface to generate oxygen-containing surface [75, 77].

In view of the strong oxidizing and dehydrating properties of concentrated sulfuric acid, to improve the dispersity of the product, concentrated nitric acid was used as the only oxidizing agent and the product thus obtained (NDNT) is gray-colored similar to the pristine ND. After the nitric acid treatment, the FT-IR analysis of NDNT and NDAT, together with pristine ND, is performed and the results are given in Figure 3.1.

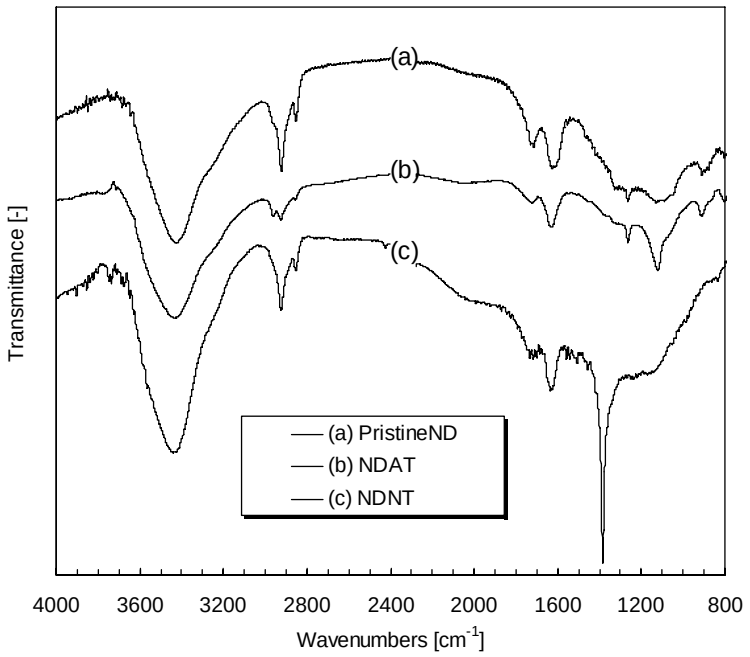

Figure 3.1 FT-IR spectra of NDs treated with oxidizing acids. NDAT: oxidizing acid mixture (sulfuric and nitric acids) treated ND. NDNT: nitric acid treated ND.

It could be seen from the FT-IR spectra (Figure 3.1) that pristine ND is actually already rich in hydroxyls and carboxyls while after oxidizing acid treatment (both acid mixture and nitric acid) the stretch vibration of C=O (**CO**OH, *ca.* 1730 cm^{-1}) seems to be weakened to different extent for NDAT and NDNT in comparison with the pristine ND.

In order to verify the results obtained from the FT-IR analysis, 0.1 wt% aqueous suspensions of NDs were prepared and the pHs were measured. The results are given in Figure 3.2.

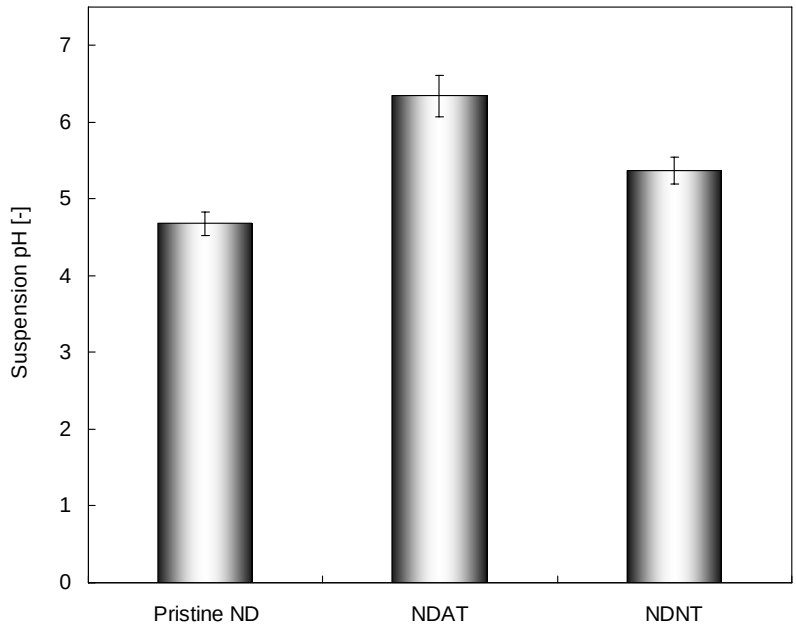

Figure 3.2 pHs of different ND aqueous suspensions (at 0.1 wt% concentration). NDAT: oxidizing acid mixture treated ND. NDNT: nitric acid treated ND. The error bar represents standard deviation.

The pristine ND suspension has a pH of *ca.* 4.7 while the acid mixture and nitric acid treatments bring pH up to *ca.* 6.3 and *ca.* 5.5, respectively. The increase in pH values after the treatment indicates that there might be a decrease in carboxyl group density on ND surface.

Combining Figures 3.1 and 3.2, it is clear that after the acid treatment (both acid mixture and nitric acid) the carboxyl group density on pristine ND surface might be reduced. The aim of acid treatment is to oxidize and remove graphite layer to generate carboxyl groups. However, for detonation ND used in this work, its graphite layer content is lower than NDs prepared by other production methods [64] which might be due to a more extensive and complete oxidizing acid treatment in production process. So it is possible that the carboxyl groups anchored on the surface

of pristine ND might be destructed and conjugated by strong oxidizing acid treatment (upon oxidizing they could be conjugated by forming C-O-C and C-N-C bonds as indicated in literatures [75, 77]). In this case, though the oxidizing acid might generate carboxyl groups by oxidizing graphite layer on ND surface, the oxygen-containing groups are simultaneously destructed by conjugating with each other and therefore the negative effects might outweigh the positive ones. These results are consistent with the work reported by Loktev et al [67] where it was found that the sulfuric and nitric acid treatment produced ND with considerable amount of graphitic carbon and the product was in a highly aggregated form.

Actually in the present work, it is reasonable to believe that the graphite layer on ND surface has already been greatly removed by the manufacturer because it is gray-colored fine powder, unlike the black-colored detonation ND powders (see Figure 3.3) as reported in previous work where a further oxidizing acid treatment is necessary to remove ND surface graphite layer [17].

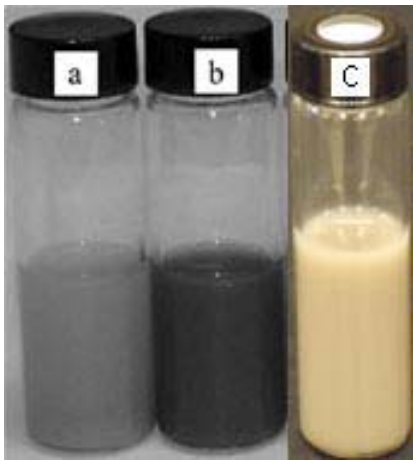

Figure 3.3 Oxidizing Acid treated (a) and pristine NDs (b) in literature report [17] as well as pristine ND in this work (c) in DI water at a concentration of *ca.* 0.4 wt%.

According to the above discussion, it is found that the pristine ND used in the present thesis

work is already high in oxygen-containing surface groups (low in surface graphite layer) and it is also found that a further oxidizing acid treatment gives rise to the destruction and conjugation of these oxygen-containing groups. Actually detonation ND surface properties might vary depending on different manufacturers, the ND used in the present work has already been well treated with oxidizing acid so that its surface is high in oxygen-containing groups and low in graphite which is desirable for further functionalization. Therefore, in this chapter as well as all other chapters throughout this thesis work, no further oxidizing acid treatment is applied. Instead, pristine ND is used directly for further functionalization.

3.3.2 Synthesis of NDCMCS

The synthesis of CMCS is carried out through zero-length crosslinker 1-(3-Dimethylaminopropyl)-3-ethylcarbodiimide hydrochloride (EDC) which is schematically illustrated in Figure 3.4.

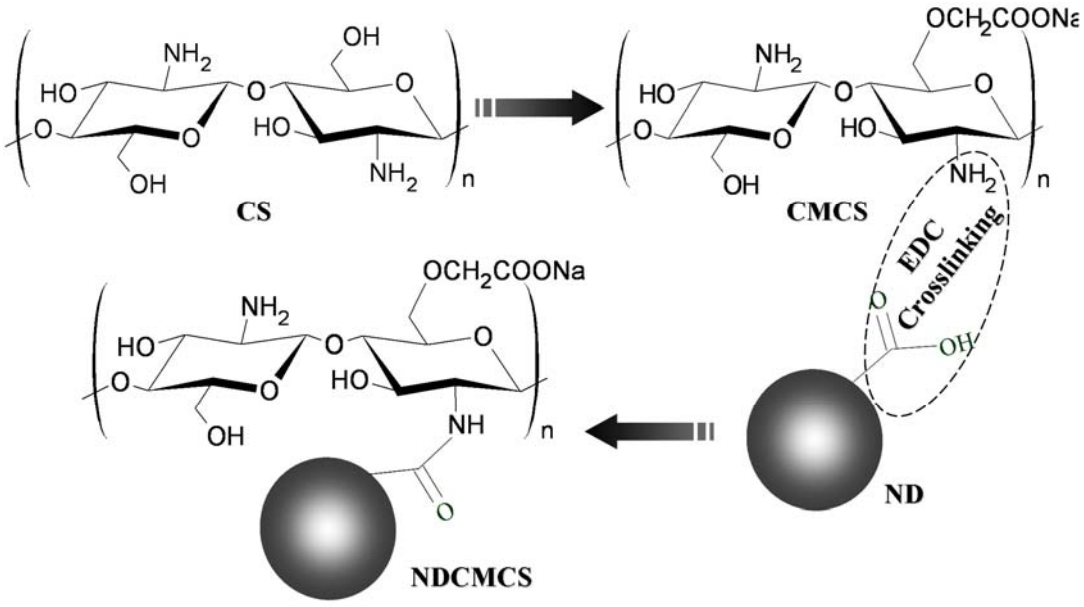

Figure 3.4 Schematic illustration of the NDCMCS synthesis process.

The FT-IR spectra of pristine ND, CMCS, and NDCMCS are given in Figure 3.5.

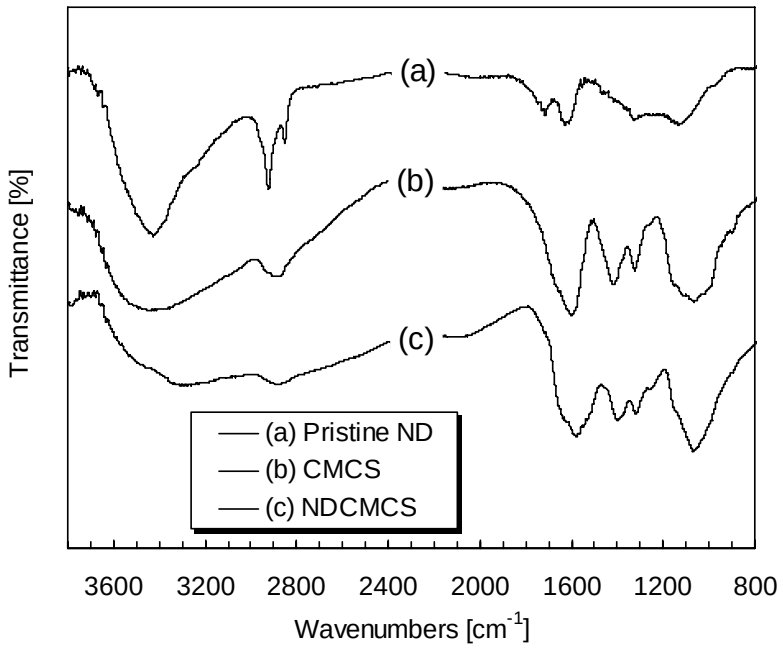

Figure 3.5 FT-IR spectra of pristine ND (a), CMCS (b), and NDCMCS (c).

Pristine ND is rich in oxygen-containing surface groups such as hydroxyls and carboxyls as evidenced in Figure 3.5 (*ca.* 3460 cm^{-1} for hydroxyl stretching vibration and ca. 1730 cm^{-1} for

carbonyl stretching vibration). These surface groups could be conjugated with primary amines on CMCS with the aid of EDC. After introducing carboxyls onto chitosan, the obtained chitosan derivative (CMCS) is characteristic of COONa (*ca.* 1620 cm^{-1}) as well as glucopyranose ring (*ca.* 1080 cm^{-1}) from chitosan. As can be seen from Figure 3.5, all the typical peaks on CMCS are found on the NDCMCS, indicating that CMCS has been successfully introduced onto pristine ND surface. The mass ratio of CMCS on NDCMCS is approximately 30 % by TGA analysis (Figure 3.6).

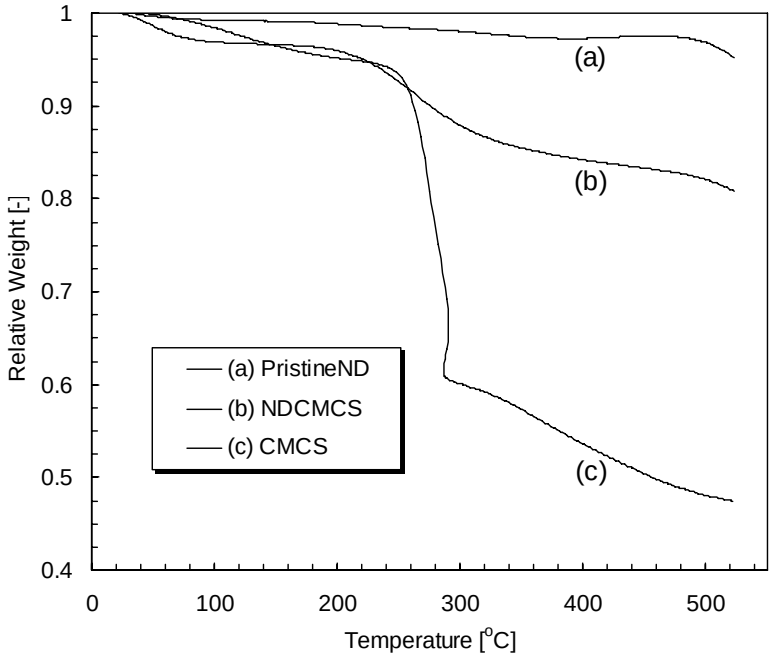

Figure 3.6 TGA curves of Pristine ND (a), NDCMCS (b), and CMCS (c).

Another evidence of chemical immobilization of CMCS on pristine ND surface is the dispersibility improvement of NDCMCS in acidic and alkaline conditions (Table 3.1). It is found that pristine ND is relatively difficult to be dispersed in 0.1 M HCl aqueous solution and almost impossible to be dispersed in 1.0 M NaOH aqueous solution. After introducing CMCS onto

pristine ND surface, due to the existence of polyampholyte CMCS on the ND particle surface, NDCMCS can be well dispersed in 0.1 M HCl, deionized water as well as 1.0 M NaOH. The NDCMCS shows the same dispersibility with CMCS in different solvents, indicating that the CMCS might dominate the NDCMCS surface after the modification process.

Table 3.1 Dispersibility of CMCS, NDCMCS and pristine ND in different solvents [a].

Solvents	CMCS	NDCMCS	Pristine ND
0.1 M HCl [b]	++	++	+
Deionized Water	++	++	++
1.0 M NaOH [b]	++	++	—

[a] Dispersibility: ++ dispersible; + less dispersible; — not dispersible.

[b] aqueous solution.

Therefore, the findings suggest that the functionalization of ND surface with CMCS could improve its dispersibility in acidic and alkaline conditions, which will definitely expand its applications in solution system since NDCMCS possesses excellent dispersibility in both acidic and alkaline conditions.

Figure 3.7 shows the Raman spectra of pristine ND and NDCMCS. The Raman spectrum of pristine ND is composed of two bands, approximately at 1330 cm^{-1} and 1600 cm^{-1}. The 1330 cm^{-1} band (D band) is the characteristic of sp^3 bonded carbon of nanostructure while the 1600 cm^{-1}

band (G band) corresponds to sp^2 bonded carbon [17]. For both pristine ND and NDCMCS, the D and G bands can be clearly seen. It is noted that after immobilizing CMCS onto pristine ND surface, the peak intensity ratio of I_D/I_G almost remains the same (from ca. 0.94 for pristine ND to ca. 0.9 for NDCMCS), suggesting that the chemical modification of pristine ND by CMCS under mild conditions in the present work could keep intact the pristine ND sp^3 and sp^2 structure.

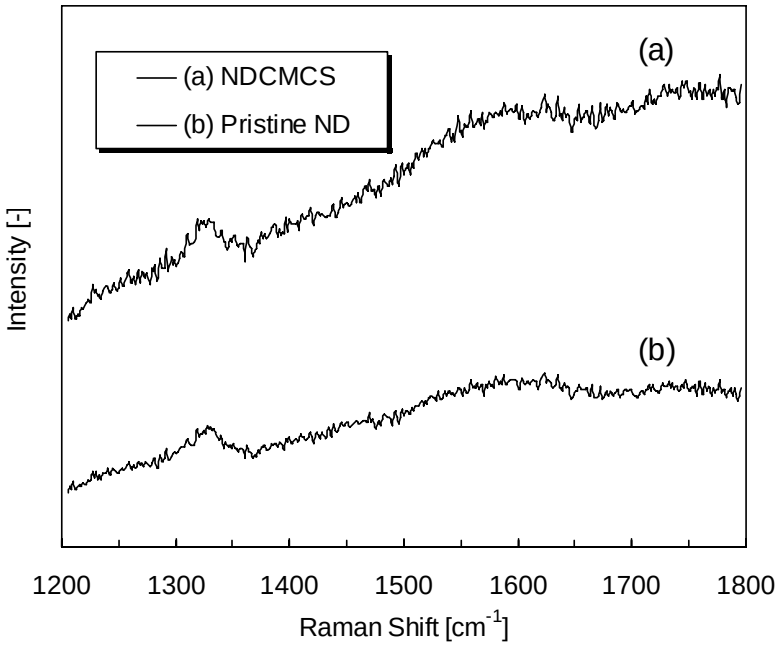

Figure 3.7 Raman spectra of NDCMCS (a) and pristine ND (b).

Zeta-potential measurements further demonstrate the existence of CMCS on ND surface as given in Figure 3.8. The pristine ND shows negative zeta-potentials throughout the whole pH range in the measurement since the pristine ND surface is dominated by a large quantity of negatively charged groups, e.g. hydroxyls and carboxyls. It can also be found that the charge density on the ND surface is relatively low since the absolute value of zeta-potential is low over the whole pH range. For CMCS, due to the fact that it is polyampholyte, the zeta potential shows

both negative and positive values with isoelectric point (pI) being 5.37. After chemical immobilization of CMCS onto pristine ND surface, the surface charge property of the modified product NDCMCS is totally different from that of pristine ND but similar to that of CMCS suggesting that CMCS polymer chains dominate the ND surface after the modification. The pI of NDCMCS is determined as 5.51 by zeta-potential measurement.

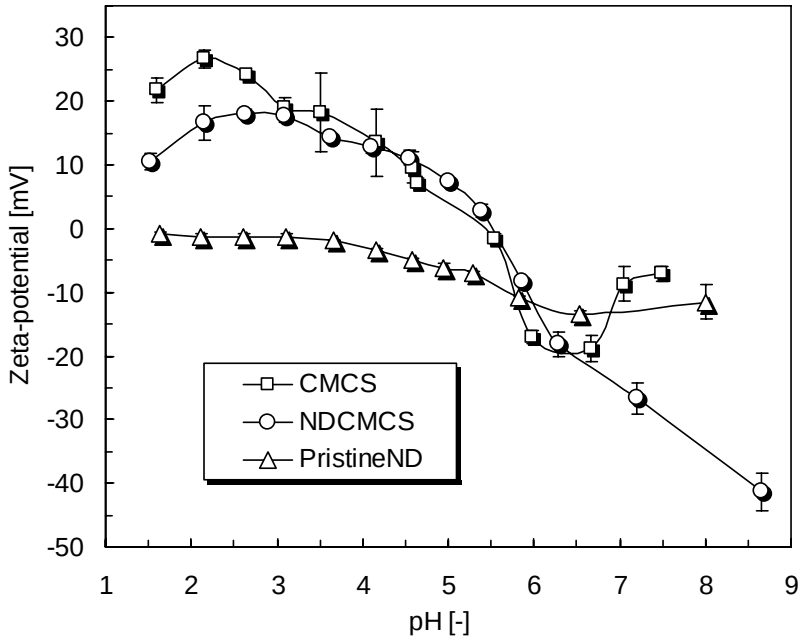

Figure 3.8 Effect of pH on the zeta-potential of pristine ND, CMCS, and NDCMCS. The error bar represents standard deviation.

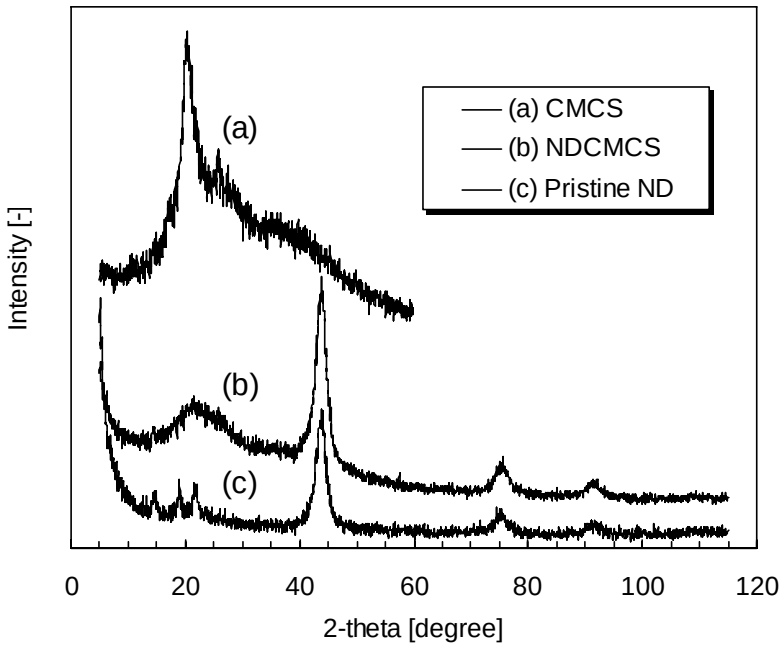

Figure 3.9 XRD diffraction patterns of CMCS (a), NDCMCS (b), and pristine ND (c).

The XRD diffraction patterns are shown in Figure 3.9. Pristine ND exhibits typical peaks at 44.2^{o}, 75.8^{o}, and 92.1^{o} (2θ) which are attributable to the diffractions of (111), (220), and (311) planes of diamond crystal, consistent with a previous report [189]. CMCS shows typical semicrystalline structure with a broadened peak at around 20^{o}. For NDCMCS, the XRD pattern shows all the 3 typical peaks of pristine ND and a broadened peak at around 20^{o}, further confirming the immobilization of CMCS onto pristine ND to form the final product NDCMCS.

3.4 Summary

The ND used in the present work is already rich in oxygen-containing surface groups and therefore further oxidizing acid treatment is not necessary. Functionalization of ND with CMCS has been conducted by EDC chemistry and the final product NDCMCS was characterized by a

series of analyses including FT-IR spectroscopy, Raman spectroscopy, Zeta-potential measurement and X-ray diffraction. All the results obtained have clearly demonstrated that CMCS is successfully immobilized onto ND surfaces and the functionalization has been proved to be effective. The functionalization with CMCS improves the dispersity of ND especially in low and high pH aqueous solutions. Moreover, the rich content of primary amine and hydroxyl on CMCS backbone would make further physical or chemical functionalization of ND more flexible and versatile.

CHAPTER 4

STUDY ON PROTEIN CONFORMATION AND ADSORPTION BEHAVIORS IN NANODIAMOND PARTICLE-PROTEIN COMPLEXES

This chapter has been published in *Nanotechnology*:

Wang H.D.; Niu C.H.; Yang Q.; Badea I. Study on protein conformation and adsorption behaviors in nanodiamond particle-protein complexes. *Nanotechnology* **2011**, 22, 145703.

Contribution of the Ph.D. Candidate

Under the guidance of Prof. Yang and Prof. Niu, Hai-Dong Wang designed and conducted the experiment for this chapter as well as prepared manuscript for publication. Prof. Badea has also provided guidance in both experiment and manuscript revision.

4.1 Introduction

Chapter 3 deals with chemical immobilization of polysaccharide onto ND surface. In this chapter, the immobilization of protein, which is another important biomacromolecule, is studied in detail. This chapter is focusing on the protein adsorption behaviors onto ND surface as well as whether protein could retain its structural features upon immobilization. To this end, bovine serum albumin (BSA) was chosen as a model protein for the study of protein conformation and the interaction between ND and protein in their complex. BSA is a well-characterized protein, which is the so called “soft” protein with low internal stability and therefore could easily undergo

conformational changes upon environment changes [190]. The results have demonstrated that ND is an excellent platform for protein immobilization with high affinity and most of BSA structural features could be preserved upon immobilization, suggesting that ND holds great potential for biosensor applications.

4.2 Materials and Methods

4.2.1 Materials

Detonation nanodiamond particles (NDs), which have an average crystal size of 3-5 nm, were purchased from Nanostructured & Amorphous Materials Inc. and used without further treatment. Bovine serum albumin (BSA), purchased from Bio Basic (purity>98 %), was used as received. All other reagents were of analytical grade and used without further purification. The water used in the present research is from a Milli-Q system.

4.2.2 Fourier Transform Infrared (FT-IR) Studies

To investigate the influence of ND-BSA interaction on conformational changes of BSA in ND-BSA complex, FT-IR spectra were recorded on a JASCO FT/IR-4100 spectrometer.

The ND-BSA complex was obtained by mixing ND suspension (in pH 7.4 phosphate buffer, 0.1 M) and BSA solution (in pH 7.4 phosphate buffer, 0.1 M) and then separating ND-BSA complex from the solution by centrifugation. The complex was repeatedly rinsed with Milli-Q water to remove unbound BSA. The ND-BSA complex was lyophilized to dryness. 1 mg of ND-BSA complex was then ground with 100 mg of dried KBr to form homogeneous powder.

After that approximately 25 mg of powder was made into pellets which were subjected to FT-IR measurement for absorbance spectrum. For each measurement, a total of 64 scans were averaged with a resolution of 4 cm^{-1}. This KBr-based method has been proved not to introduce artificial structural change to protein in previous analyses [191, 192]. For the measurement of ND-BSA complex, the reference spectrum (the ND/KBr mixture possessing identical amount of ND with that in ND-BSA complex) was recorded in the identical manner and subtracted from that of ND-BSA complex. For BSA, the BSA/KBr powder used for the measurement has the same BSA content as that in ND-BSA/KBr powder and pure KBr was employed as reference. Baselines of spectra were corrected according to the criterion that a straight baseline was obtained in the region from 1750 to 2000 cm^{-1}, which is critical to obtain correct structural information using the second-derivative analysis method [191, 193]. Second derivatives were then obtained using spectrum analysis software on JASCO FT-IR spectrometer.

4.2.3 Ultraviolet-visible (UV-Vis) Absorption Spectra

UV-Vis spectra were recorded on a UV-Vis spectrophotometer (Shimadzu UVmini-1240) with wavelength ranging from 240 to 310 nm. The contribution of light scattering from ND was determined by plotting $\log_{10}$(absorbance) as a function of $\log_{10}$(wavelength) above 310 nm and then extrapolating linearly to shorter wavelengths since BSA doesnot show absorbance at wavelength higher than *ca*. 310 nm [194]. Then the effect of light scattering from ND particles was removed from the UV-Vis spectra. The BSA concentration was fixed at 1.5×10^{-6} M in both ND-BSA complex solutions (buffered at pH 7.4 by 10 mM phosphate buffer) where ND

concentrations were 1.5×10^{-7} and 4.5×10^{-7} M, respectively. The sample solutions were prepared at room temperature right before the experiment. Each spectrum presented was the average of 3 scans. All measurements were performed at 25 ^{o}C.

4.2.4 Circular Dichroism (CD) Spectroscopy

The circular dichroism (CD) spectra of BSA in the absence and presence of ND were recorded on a PiStar-180 Spectrometer (Applied Photophysics Ltd., UK) at 25 ^{o}C. All CD spectra were collected in a wavelength range from 200 to 250 nm using a rectangular quartz cell with 10 mm path length. Each spectrum was measured in triplicate with the data presented being the average. The BSA concentration was fixed at 2.5×10^{-7} M with ND concentration ranging from 2.5×10^{-9} to 10^{-8} M. CD backgrounds were corrected for each measurement. All samples were buffered at pH 7.4 by 10 mM phosphate buffer. The α-helix content of BSA is determined by Equation (4.1) [195, 196]:

$$\%\alpha Helix = \frac{(-[\theta_{208}] - 4000)}{(33000 - 4000)} \times 100 \tag{4.1}$$

Where $[\theta_{208}]$ is the mean residue ellipticity at 208 nm in $\deg \cdot cm^2 \cdot dmol^{-1}$.

4.2.5 Fluorescence Quenching Measurements

Fluorescence measurements were performed on a fluorescence spectrophotometer (Cary Eclipse, Varian) at 25 ^{o}C. All the emission spectra were collected at the excitation wavelength of 295 nm using 5 nm/10 nm (excitation/emission) slit widths and a rectangular quartz cell with 10

mm path length. Each spectrum presented was the average of at least 3 scans. To avoid the inner filter effects, highly diluted solutions ([BSA]=1.5×10^{-6} M and [ND]=1.2×10^{-8} to 8.2×10^{-8} M) were used for all measurements. Fluorescence backgrounds were corrected for blank buffer solutions in each measurement.

4.2.6 Equilibrium Adsorption of BSA onto ND Surface

ND was dispersed, with ultrasonic treatment (Branson 2510 Sonication Bath), in phosphate buffer solution (0.1 M) at a concentration of 2.0 mg/ml. After that 5 ml of ND suspension was mixed with 5 ml of BSA solution buffered at the same pH by phosphate buffer (0.1 M). The ND-BSA suspension was then mixed thoroughly with a Multitron Incubator Shaker at 25 ^{o}C and 180 rpm for 2 hour which was confirmed to be more than adequate to establish adsorption equilibrium under the conditions of present research. Finally the suspension was subjected to centrifugation on a Beckman Coulter Allegra X-22R centrifuge (15,000 rpm, 30 min) and the BSA concentration in supernatant was analyzed on a UV/Vis spectrophotometer (Shimadzu UVmini-1240) at a wavelength of 280 nm. All the samples were run in duplicates with data presented being the average. Blank reference was used during adsorption experiment to confirm the influence of floating ND in supernatant was negligible. The BSA uptake was determined by the concentration difference between the initial BSA solution and final supernatant, as expressed in Equation (4.2):

$$q = \frac{(C_0 - C)\cdot V}{m} \tag{4.2}$$

Where q is BSA uptake (mg/g dry ND), C_0 and C are BSA concentrations in initial solution

(mg/ml) and final supernatant (mg/ml), respectively. V is the solution volume (ml) and m the dry net weight of ND (g).

4.2.7 Zeta-potential Measurements

Zeta-potential measurements were carried out on a Zetasizer Nano ZS instrument (Malvern) over a pH range from approximately 9.0 to 3.0 at 25 ^{o}C. Zeta-potential was determined by measuring the electrophoretic velocity of the nanoparticles by Laser Doppler Velocimetry technique. The pH of the solution measured was adjusted by an autotitrator using NaOH and HCl solutions. After reaching the desired pH by titration, the solution was left to equilibrate for 1 min before taking measurement. Each measurement was performed in triplicate with the data presented being the average. For all measurements, the ND concentration was fixed at 0.005 mg/ml. The BSA concentrations in ND-BSA complex solutions were 0.00125 and 0.005 mg/ml, respectively. The samples were prepared at room temperature right before the measurements. For ND-BSA samples no centrifugation was used in order to retain the original conformation of BSA in complex.

4.3 Results and Discussion

4.3.1 FT-IR Characterizations

FT-IR spectroscopy is a widely used technique to study protein conformation [197-199]. Different amide bond orientations within peptide backbone can be attributable to various secondary structures such as α-helix, β-sheets, β-turns, and unordered structures (or referred to as

random coil) [196, 200]. Among all amide bands (amide I, II, and III), amide I region (1600~1700 cm^{-1}, mainly due to C=O stretching vibration) has been proved to be helpful for protein conformational studies since it is the most sensitive to protein secondary structure changes [196]. According to previous research [191, 196, 197, 200-202], the assignment of secondary structures is as the following: 1695-1663 cm^{-1} for β-sheet or β-turn structures, 1662-1650 cm^{-1} for α-helices, 1648-1644 cm^{-1} to random chains, 1642-1618 cm^{-1} for β-sheets. Bands at lower wavenumbers (*ca.* 1616 cm^{-1}) have been assigned to side chain moieties.

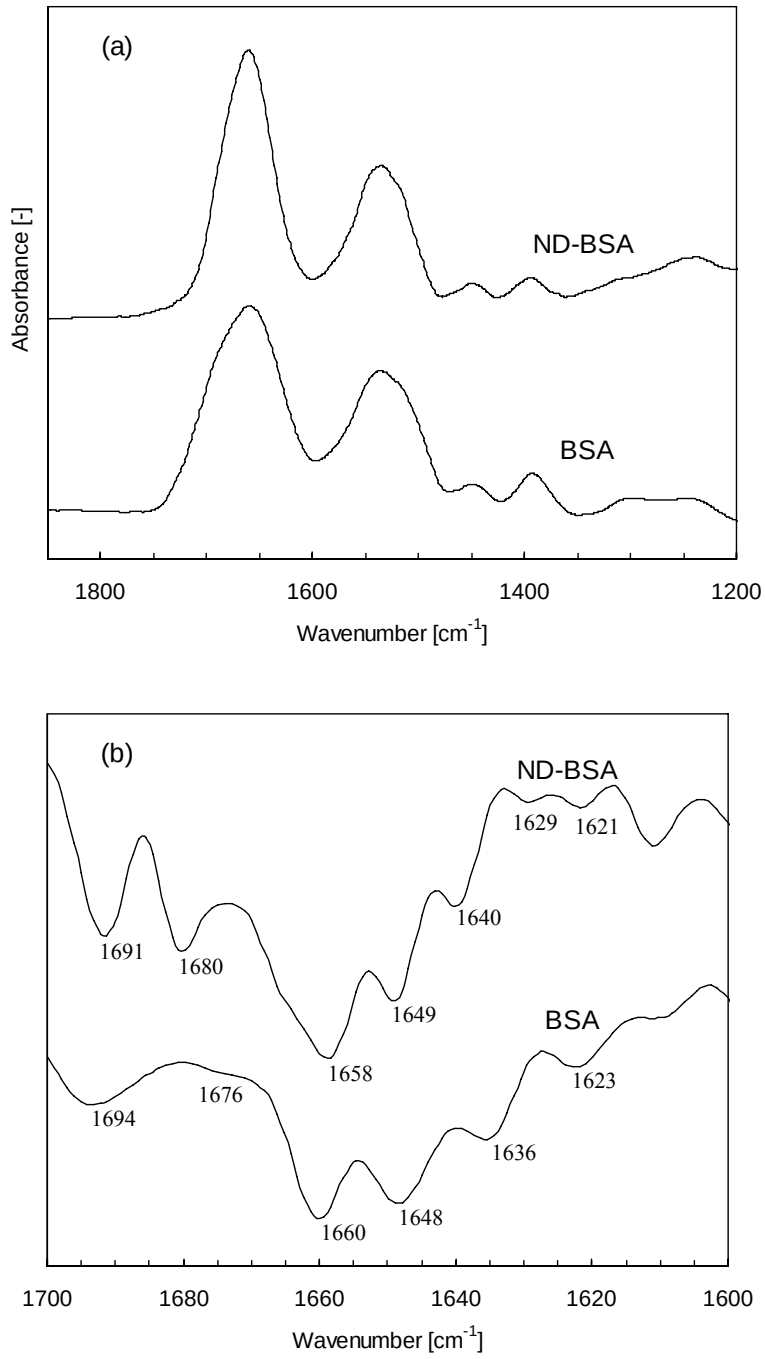

Figure 4.1 FT-IR spectra of (a) native BSA and BSA in ND-BSA complex as well as (b) the corresponding second derivative spectra in amide I region.

The FT-IR spectra of native BSA as well as BSA in ND-BSA complex are given in Figure 4.1 (a), where the amide I and II bands are shown. From Figure 4.1 (a), both native BSA and BSA in

ND-BSA complex show noticeable peptide bonds indicating that BSA has been attached onto ND surface. Figure 4.1 (b) further shows the specific difference in secondary structures by comparing second derivative spectra of native BSA and BSA in ND-BSA complex. For native BSA, α-helix dominates the spectra at *ca.* 1660 cm^{-1} which is also true with that of ND-BSA complex where α-helix appears at *ca.* 1658 cm^{-1}. The intensity of unordered structure (*ca.* 1649 cm^{-1}) is higher in the complex than that in native BSA. The intensities for β-turn (1694 and 1676 cm^{-1}) and β-sheet (1636 cm^{-1}) structures in native BSA are also found to increase in ND-BSA complex. For most peaks, the peak position changes slightly after the formation of complex. Moreover, a new peak at *ca.* 1629 cm^{-1}, which could be assigned to β-sheet structure, appears in the complex. All these changes in BSA second derivative spectra indicate the strong interaction between ND and BSA.

4.3.2 UV-Vis and CD Spectroscopies

The UV-Vis spectroscopy could provide information regarding whether there is major structural change occurred in proteins. The absorbance of protein in the 230~300 nm range is mainly attributable to aromatic residues, including tryptophan, tyrosine, and phenylalanine. The absorption spectra of the aromatic residues depend on their molecular environment which could give rise to the change in wavelength and intensity. In general, the shift in wavelength predominates. An evident blue-shift in the spectrum is likely to occur if the aromatic residue is exposed to an environment with more polarity. In the present work, as shown in Figure 4.2, BSA absorption spectra at *ca.* 278 nm (aromatic residue) nearly have no shift upon forming complex with ND indicating that the formation of ND-BSA complex might not result in major BSA

unfolding.

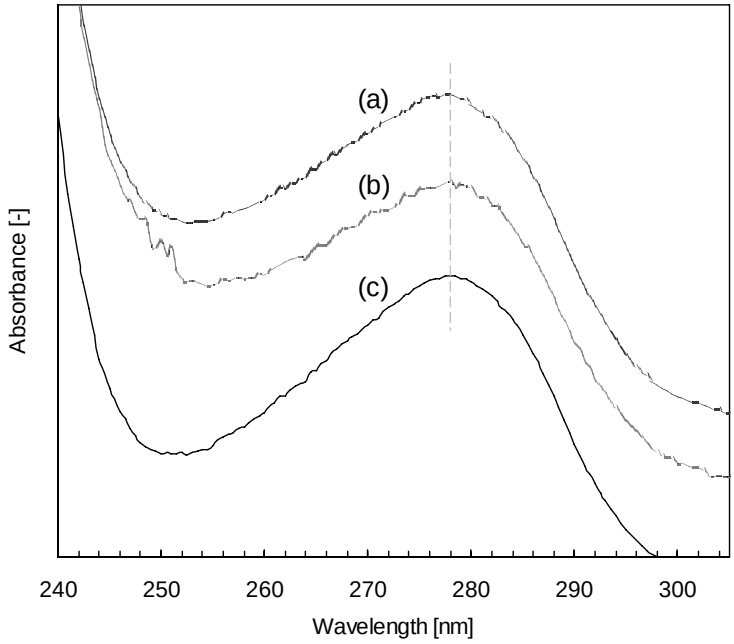

Figure 4.2 UV-Vis absorption spectra of (a) BSA in ND-BSA complex (ND concentration: 1.5×10^{-7} M), (b) BSA in ND-BSA complex (ND concentration: 4.5×10^{-7} M), and (c) native BSA. The BSA concentration is fixed at 1.5×10^{-6} M.

For a quantitative analysis of to what extent BSA structural features could be preserved upon binding to ND surface, CD spectroscopy is used to further study BSA conformation and conformational changes. The protein structural features determine its biological functionality so the study on CD spectra of protein could shed light on whether protein could retain its biological functionality. For albumin which features a dominant content of α-helix in its secondary structure actually α-helix content is a good indicative of its structural features and a major loss of α-helix content probably suggests the loss of protein biological functionality [203, 204]. In CD spectroscopy, the α-helix features negative CD signals at 208 nm and 222 nm.

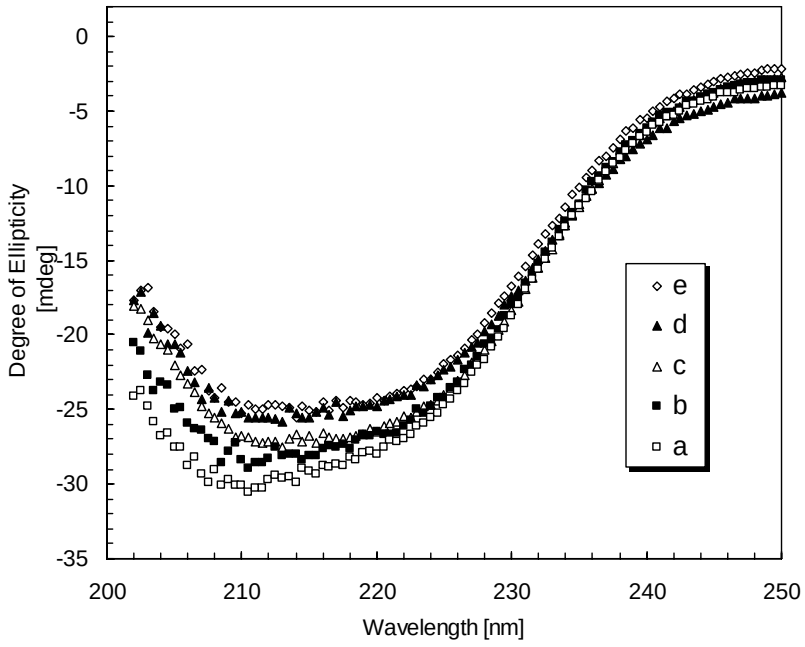

Figure 4.3 The CD spectra of 2.5×10^{-7} M BSA (curve a) with the regular addition of ND at pH 7.4. ND concentration is from 2.5×10^{-9} to 10^{-8} M (curves b~e).

The CD spectra of native BSA in the absence or presence of ND are given in Figure 4.3. According to Figure 4.3, native BSA at pH 7.4 (buffered by 10 mM phosphate buffer solution) has an α-helix content of *ca.* 55% which is consistent with previous report [200]. With the regular addition of ND suspension (buffered at pH 7.4 by 10 mM phosphate buffer solution), the ellipticities of BSA at both 208 and 222 nm are gradually decreased indicating loss of BSA secondary structure upon forming complex with ND. However, BSA still has an α-helix content of *ca.* 43% (nearly 80% of its original α-helix content) even when ND concentration is increased up to 10^{-8} M. Obviously most of α-helix content in BSA is preserved after forming complex with ND even at a high ND concentration (10^{-8} M), which suggests it is very likely that protein could retain its biological functionality upon complexing with ND since its structural features are

preserved to a large extent. From the second derivative spectra as shown in Figure 4.1 (b), BSA in ND-BSA complex doesnot show a major decrease in its α-helix intensity (*ca.* 1660 cm^{-1}) upon forming complex with ND, which agrees well with the findings from CD spectra.

It is noteworthy that gold nanoparticles have been extensively studied in nanoparticle-biomolecule related work [205]. However, previous research [196] revealed that when gold nanoparticle concentration is increased to 1.1 nM protein BSA could only retain *ca.* 75% of its original structure while in the present work BSA could retain nearly 80% of its structural features even when ND concentration is increased up to 10^{-8} M, which could probably attributable to the relatively less binding force involved in ND-protein than that in gold nanoparticle-protein complex.

4.3.3 Fluorescence Quenching Studies

Fluorescence spectroscopy could provide useful information regarding the structural changes of protein [206]. Normally the interaction between a fluorophore and a molecule induces perturbation or modification in the fluorescence parameters such as intensity, peak position, etc. and these perturbations in fluorescence parameters will allow to obtain the information about the environment of the fluorophore which enables the understanding of the nature and origin of interactions between the fluorophore and other molecules [206, 207]. Tryptophan, tyrosine and phenylalanine are three intrinsic fluorophores which are responsible for the fluorescence properties of proteins. The tryptophan (Trp) fluorescence is the most sensitive to the environment change [206]. BSA in the present work is a widely used model protein [208, 209], which

possesses two Trp residues [210]. By analyzing the fluorescence emission spectra of Trp in ND-BSA complex, the BSA structural change in the region of Trp residues can be obtained. In the present fluorescence analysis, 295 nm is used as excitation wavelength instead of 280 nm to avoid the tyrosine residue fluorescence [210, 211]. Therefore the Trp is the only fluorophore studied in the present work.

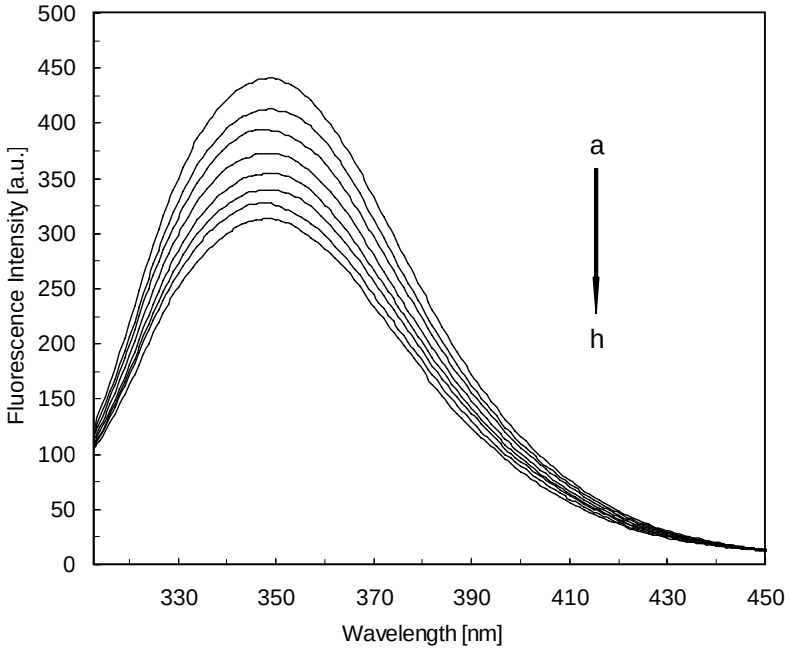

Figure 4.4 The fluorescence emission spectra of 1.5×10^{-6} M BSA (curve a) with the regular addition of ND at pH 7.4. ND concentration is from 1.2×10^{-8} to 8.2×10^{-8} M (curves b~h).

Figure 4.4 shows the typical fluorescence emission spectra of the BSA in the absence and presence of ND at pH 7.4. Originally at pH 7.4 BSA emission spectrum peaks at *ca.* 350 nm while with the regular addition of ND the emission spectra undergo a considerable intensity decrease as well as a slight blue shift in emission maximum. Obviously the fluorescence emission of Trp in BSA is quenched in the presence of ND.

Fluorescence quenching process could be described by Stern-Volmer equation as in Equation (4.3) [206]:

$$\frac{F_0}{F} = 1 + k_q \tau_0 [Q] = 1 + K_{SV}[Q] \tag{4.3}$$

where F_0 and F are the maximum fluorescence intensities of BSA in the absence and presence of ND, respectively while K_{SV} the Stern-Volmer constant (M^{-1}) which is a measure of quenching efficiency and Q is the quencher (ND) concentration (M). k_q and τ_0 are the bimolecular quenching constant ($M^{-1}s^{-1}$) and the mean fluorescence lifetime of the fluorophore in the absence of quencher (s).

Plot $\frac{F_0}{F}$ against $[Q]$ then we have K_{SV} as the slope of the linear regression curves, which is given in Table 4.1. According to the $\frac{F_0}{F} \sim [Q]$ curve, the Stern-Volmer constant K_{SV} is determined, which shows that all the Stern-Volmer constants are in the order of 10^6 M^{-1}. For BSA, the lifetime of fluorophore τ_0 is approximately 5×10^{-9} s [196, 212]. Then the bimolecular quenching constant k_q could be determined, from Equation (4.3), to be in the order of 10^{14}~10^{15} $M^{-1}s^{-1}$ which is much higher than the maximum bimolecular quenching constant for a diffusion-controlled quenching process (*ca.* 10^{10} $M^{-1}s^{-1}$). The high k_q obtained in the quenching process suggests that there is specific strong interaction between ND and BSA and the dominating quenching mechanism involved is static quenching by complex formation [213, 214].

Table 4.1 The Stern-Volmer constant K_{SV} and the slope of the trend line in double-wavelength method K_{slope}.

pH	K_{SV} [M^{-1}]	K_{slope} [-]
3.5	$4.75\times10^{6} \pm 0.1\times10^{6}$	$8.51\times10^{-3} \pm 0.68\times10^{-3}$
4.7	$5.5\times10^{6} \pm 0.05\times10^{6}$	$3.16\times10^{-3} \pm 0.38\times10^{-3}$
6.0	$4.92\times10^{6} \pm 0.1\times10^{6}$	$2.05\times10^{-3} \pm 0.29\times10^{-3}$
7.4	$4.91\times10^{6} \pm 0.08\times10^{6}$	$4.29\times10^{-3} \pm 0.68\times10^{-3}$
9.0	$6.63\times10^{6} \pm 0.22\times10^{6}$	$1.06\times10^{-2} \pm 0.24\times10^{-2}$

The Stern-Volmer constant K_{SV}, as given in Table 4.1, peaks at pH 9.0 which is followed by that of pH 4.7. For pHs 3.5, 6.0, and 7.4, K_{SV} almost has the same values. To illustrate the Stern-Volmer constant changes with regard to pH, the change in the position of Trp emission maximum is studied. Protein tertiary structure is held together primarily by hydrophobic interactions. The fluorescence spectroscopy could detect the hydrophobicity of the fluorophore buried inside the hydrophobic region of protein so that the information regarding the protein tertiary structural change could be revealed. Changes in protein tertiary structure (such as unfolding) very often lead to large change in fluorescence emission maximum. Normally, once protein undergoes unfolding, the emission maximum is red-shifted to a longer wavelength [194], which could be attributable to the exposure of fluorophore to solvent. In the present study, the blue shift in the position of BSA emission maximum means the complexation with ND might not perturb the BSA tertiary structure significantly suggesting major unfolding of BSA tertiary

structure is unlikely to occur. This is consistent with some previous work dealing with fluorescence spectroscopy study on protein tertiary structure changes [215, 216].

Actually the shift in the position of BSA emission maximum is small, as shown in Figure 4.4. In order to determine the pH effect on emission maximum more accurately, the double-wavelength method is employed to give quantitative evaluations as used in the previous research [217]. This method makes use of the ratio of fluorescence intensities at two wavelengths: the one on the left (F_L) to the one on the right (F_R) slopes of the spectrum. The wavelengths of F_L and F_R are 20 nm away from the emission maximum of native BSA at different pHs. In this study, to make double-wavelength method more quantitative, the slope for trend line of data points is used to evaluate the emission maximum shift: the greater the slope, the more the emission maximum shift. The trend lines obtained from double-wavelength method are given in Figure 4.5. The slope for each trend line is denoted as K_{slope} and listed in Table 4.1, which shows noticeable blue shifts for all pHs. Sharp contrasts could be seen for emission maximum shift among different pHs with pH 9.0 the highest and pH 3.5 the second highest while for pHs 4.7, 6.0, and 7.4 the shifts are much lower. BSA undergoes conformational changes at different pHs [214, 218-220]. At pH lower than 4.3 BSA is in expanded form (E form, pH<2.7) and fast form (F form, pH 2.7~4.3) while between pH 4.3~8 it shifts to normal form (N form). As pH increases further, the BSA experiences basic (B form, pH 8~10) and aged forms (A form, pH >10). Among all these forms, the normal form is the most stable and compact. With pH shifting either up or down beyond normal form, the BSA undergoes structural changes becoming less stable in its structure. Because of the structural changes when BSA is in fast and basic forms, it is relatively

less compact so that the environment of Trp residue might be relatively easily influenced by ND which forms complex with BSA. For pHs 4.7, 6.0, and 7.4, the compact structure of BSA in normal form makes the environment of Trp residue not as easily influenced by ND as in case of pHs 3.5 and 9.0. Therefore for BSA forming complex with ND at pHs 3.5 and 9.0, its Trp residues are actually exposed to more hydrophobic environment than that at pHs 4.7, 6.0, and 9.0, which could well account for the data given in Figure 4.5 that the blue shifts for pHs 3.5 and 9.0 are much higher than those for other pHs in normal form.

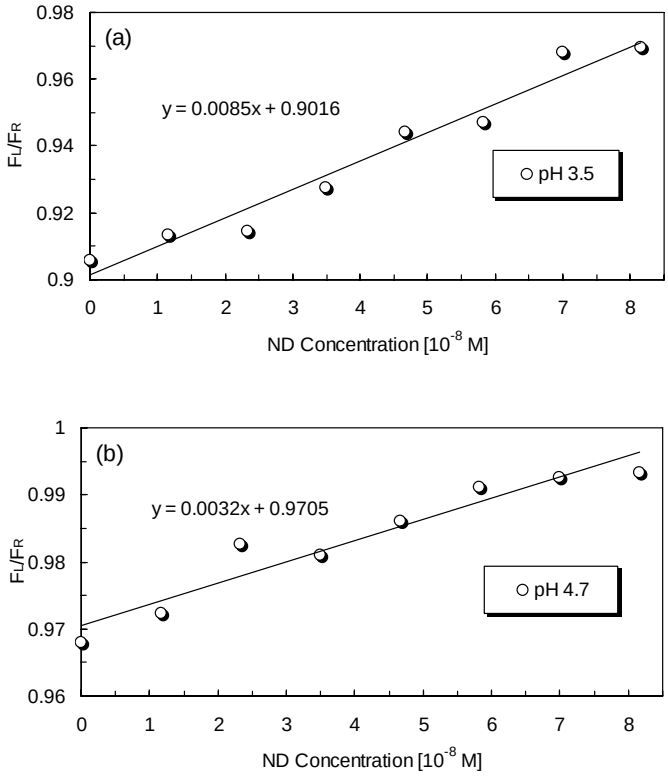

Figure 4.5 The influence of ND-BSA interaction on the position of emission maximum of BSA determined by the ratio of fluorescence intensities at two wavelengths: on the left (F_L) and on the right (F_R) slopes of the spectrum (20 nm away from emission maximum) at different pHs. Error bars are not shown since fluorescence intensities of different scans are highly consistent (variance

is within or around 1% of the average value).

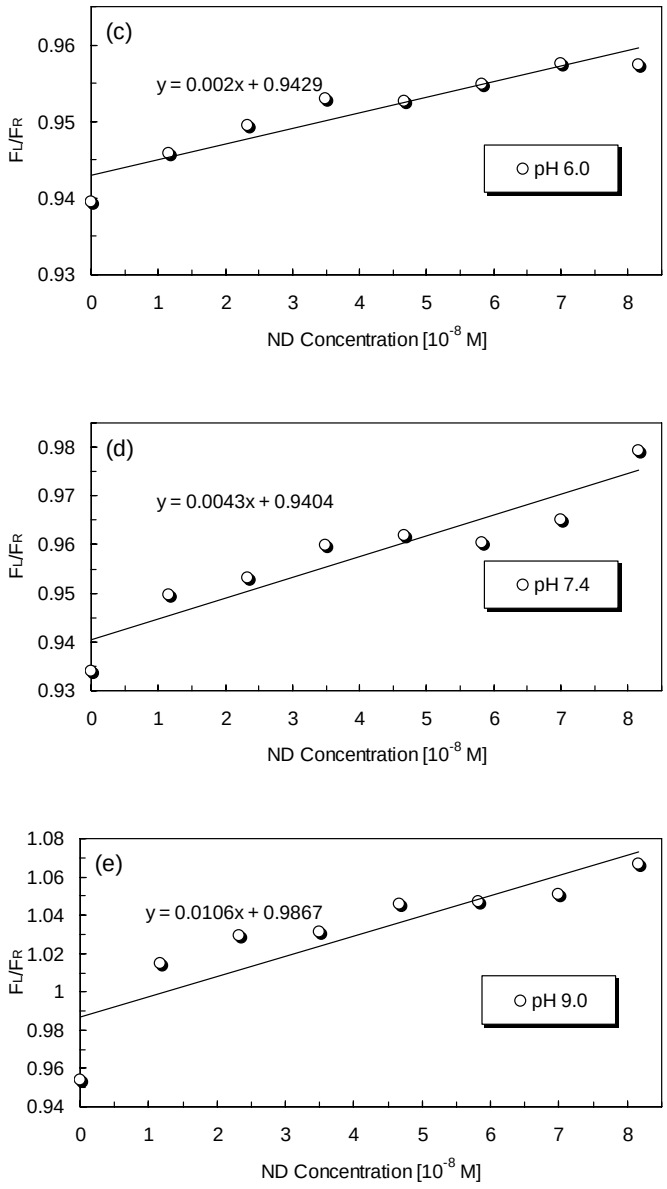

Figure 4.5 (*Continued*).

With the understanding of the emission maximum shift, the fluorescence quenching results given in Table 4.1 could be explained. At pH 9.0 the environment of Trp residue is relatively easily altered by binding with ND so the quenching is the most efficient. For pHs in normal form range (4.3~8), three pHs nearly have the same Stern-Volmer constants with that at pH 4.7

relatively higher than those at pHs 6.0 and 7.4. For pH 3.5, its Stern-Volmer constant is close to those in normal form but not as high as that at pH 9.0. That's probably because at pH 3.5 NDs tend to form large aggregates so that the number of BSA forming complex with ND is greatly reduced (Figure 4.6). Therefore the quenching of the overall BSA fluorescence at pH 3.5 is not as efficient as those at other pHs even though at pH 3.5 the environment of Trp residue might be more easily influenced by ND than those at pHs 4.7, 6.0, and 7.4.

According to the above spectroscopic studies, it is reasonable to believe that ND could provide sufficient affinity with protein for its immobilization and at the same time the binding force falls in an acceptable range in terms of preserving protein structural features. Actually there needs to be a trade-off between nanoparticle-biomolecule binding force and biomolecule structural integrity. On one hand, nanoparticles are expected to have high binding force with biomolecules; on the other hand, too strong binding force would definitely disrupt biomolecule structural features.

The retention of original structure of proteins (albumin, lysozyme, and etc.) in the nanoparticle-protein complex could possibly be attributable to the high curvature of nanoparticles (ND in the present work), which has been evidenced by some previous research [118, 221]. The ND particle in the present work has a single crystal size of *ca.* 5 nm. Thus the ND aggregates consisting of ND crystals would exhibit very high local curvature, facilitating the retention of albumin structural features. In addition, some previous research devoted to biosensor applications using ND have already demonstrated that ND could preserve the biological functionality of biomolecules immobilized on its surface to a large extent such as α-bungarotoxin (α-BTX) [86]

and lysozyme [25].

4.3.4 Equilibrium Adsorption of BSA

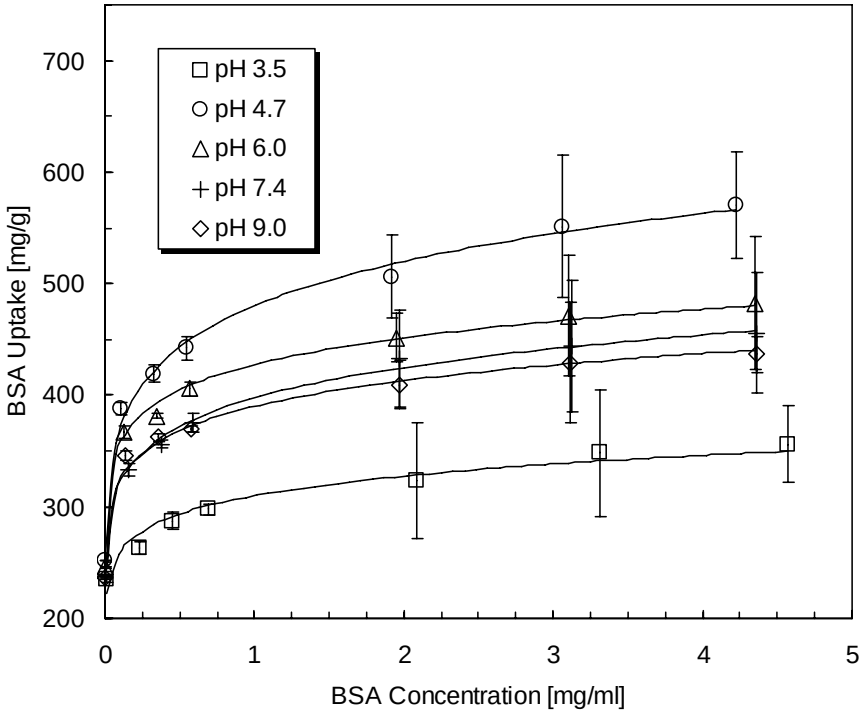

Figure 4.6 Adsorption isotherms of BSA onto ND at different pHs. The solid curves are the best fits of the experimental data to the Freundlich adsorption model (Equation 4.4). The error bar represents standard deviation.

BSA adsorption behavior on ND surface was studied by adsorption isotherms at different pHs. As can be seen from Figure 4.6, most adsorption isotherms for BSA onto ND surface show a steep slope at low BSA concentrations suggesting a strong interaction between ND and BSA. Obviously ND has the highest BSA uptake at the isoelectric point (pI) of BSA (*ca.* pH 4.7) and the lowest at pH 3.5. For each isotherm, the BSA uptakes of the last two points only differ by less

than 5% so it might be reasonable to conclude that the adsorption reaches saturation at high concentration range under the current adsorption conditions. Based on this fact, the maximum BSA uptake q_m is determined as the average of the last two BSA uptakes on each isotherm, which is listed in Table 4.2.

As shown in Table 4.2, the maximum saturated BSA uptake is *ca.* 560.5 mg/g, which is obtained at pH 4.7. According to the data given by the manufacturer, the surface area of the ND is *ca.* 300 m^2/g. Combining these two gives a BSA adsorption density of 1.9 mg/m^2 (1.7×10^{16} BSA molecules/m^2, considering that BSA molecular weight is *ca.* 67,000 Da [222]) for BSA adsorbed on the ND surface at saturation. It is known that BSA has geometric dimensions of 9.5×5.0×5.0 nm^3 [222]. Therefore for BSA adsorption onto a surface there are two possibilities: "side-on" adsorption mode with an adsorption area of 9.5×5.0 nm^2 and "end-on" adsorption mode with an adsorption area of 5.0×5.0 nm^2 [223]. The BSA adsorption density required for an adsorption monolayer on the ND surface is determined as 1.9×10^{16} BSA molecules/m^2 for side-on mode and 3.31×10^{16} BSA molecules/m^2 for end-on mode, which corresponds to 2.1 mg/m^2 and 3.6 mg/m^2 for side-on and end-on modes, respectively. The actual maximum BSA adsorption density in the present work is 1.9 mg/m^2 which is very close to the minimum BSA density required for side-on monolayer. The proposed "side-on/end-on" adsorption mode is based on the ideal situation where no change occurs in terms of protein structural features so it cannot be exactly accurate since protein is always subjected to structural changes once adsorbed onto a surface. However, the spectroscopic studies in the present work have proved that most of BSA structural features are preserved upon being attached to the ND surface, which means the BSA structural change is not

significant. In addition, BSA is prone to be adsorbed in a side-on fashion to cover the whole nanoparticle surface according to previous research [223]. Therefore the use of side-on mode to determine the density of adsorbed BSA on nanoparticle surface could be a close approximate as demonstrated by the BSA adsorption data in the present research.

Table 4.2 Maximum BSA uptake q_m, Freundlich constant K_f, and the affinity of ND to BSA $1/n$.

pH	q_m [mg/g]	K_f [-]	$1/n$ [-]
3.5	352.1 ± 5.7	310.1 ± 3.8	$7.92\times10^{-2} \pm 0.78\times10^{-2}$
4.7	560.5 ± 13.3	480.2 ± 4.0	$1.15\times10^{-1} \pm 0.05\times10^{-1}$
6.0	476.7 ± 8.1	427.4 ± 2.5	$7.91\times10^{-2} \pm 0.29\times10^{-2}$
7.4	449.9 ± 8.1	397.9 ± 2.1	$9.51\times10^{-2} \pm 0.3\times10^{-2}$
9.0	432.7 ± 5.4	390.1 ± 3.5	$8.23\times10^{-2} \pm 0.49\times10^{-2}$

It is found that Langmuir model can not fit the adsorption data. That might be attributable to the interaction (such as steric hindrance) among adsorbed BSA molecules on ND surface, considering the relative large molecular size of BSA. In addition, the ND surface might not be ideally uniform.

Freundlich model can provide desirable fit for the adsorption data, as shown in Figure 4.6. The Freundlich model is given in Equation (4.4):

$$q_e = K_f \cdot C_e^{(1/n)} \tag{4.4}$$

Where q_e and C_e are equilibrium BSA concentration on the ND surface (mg/g) and in the solution (mg/ml), respectively. K_f is the Freundlich constant related to the binding capacity of ND for BSA and $1/n$ the affinity of ND to BSA [224]. K_f and $1/n$ are determined by nonlinear regression of Equation (4.4).

K_f and $1/n$ are then summarized in Table 4.2. Both K_f and $1/n$ show similar strong pH dependence as q_m, reaching maximum at the pI of BSA and approaching minimum at pHs 3.5 and 6.0.

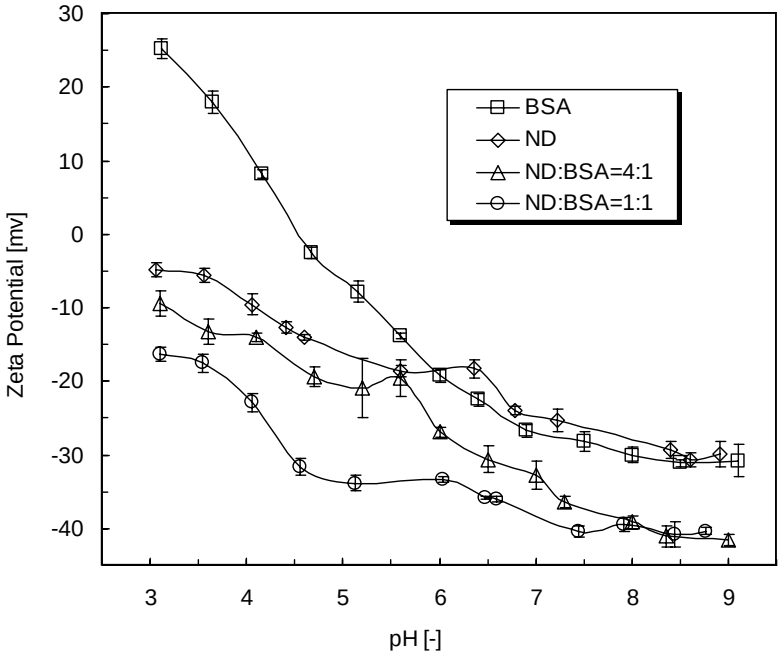

Figure 4.7 The zeta-potentials of native BSA, ND, and ND-BSA complex (with ND:BSA mass ratio of 4:1 and 1:1) over the pH range of 3~9. The error bar represents standard deviation.

The ND surface used in the present research mainly contains carboxyl and hydroxyl groups, as demonstrated in our previous work [225]. According to the zeta-potential measurements as

shown in Figure 4.7, the ND surface is always negatively charged over the whole pH range under investigation while BSA shows an isoelectric point (pI) at pH 4.6. These results agree well with previous reports [223, 226].

As shown in Figure 4.7, the zeta-potential of ND decreases with the decrease of pH, which might result from the protonation of negatively charged groups on ND surface. The interaction between protein and surface includes hydrophobic interaction, ionic interaction, hydrogen boding, and Van der Waals interaction [226, 227]. The van der Waals force is usually negligible in comparison with other forces as detailed in the previous research [227]. If electrostatic interaction is dominant in ND-BSA interaction, the highest BSA uptake would be at pH 3.5. That is because only at pH 3.5 BSA has electrostatic attraction with ND. The fact that the BSA uptake at pH 3.5 is the lowest suggests that the electrostatic interaction would not be the dominating force. It is known that nanodiamond surface is covered by a thin layer of graphite [64], which is hydrophobic in nature. Due to the hydrophobic nature on nanodiamond surface, the hydrophobic force tends to dominate the BSA adsorption process especially when the BSA molecule contains less or none surface charge. Previous research [227] revealed that for surface containing low density of carboxyl groups the hydrophobic force is dominant in protein adsorption process which is pH sensitive while for the surface high in carboxyl density hydrogen bond dominates. Dynamic light scattering measurements show that ND particles exist in the form of aggregates ranging from *ca.* 300 to 680 nm in size as pH changes from *ca.* 9.0 to 3.5 (data not shown), suggesting that the carboxyl density on ND surface is relatively low. Actually for zeta-potential with absolute value lower than 30 mV, the crystals might tend to form aggregates because of the

relatively low surface charge [228], which is the case of the present work. Because of the hydrophobic nature of ND surface graphite layer and relatively low ND surface charge, hydrophobic force tends to dominate the BSA adsorption process. Accordingly, the BSA uptake and ND-BSA affinity peak approximately at the pI of BSA.

At pH 3.5 ND has the lowest BSA uptake and lowest affinity with BSA. This could be attributable partly to the fact that hydrophobic force dominates the ND-BSA interaction and partly to the relatively larger size of ND aggregates at low pH. The size of ND aggregates is kept at *ca.* 300 nm in the pH range of 6~8.5 while increases sharply to nearly 680 nm as pH is reduced to *ca.* 3.5 (data not shown). The relatively larger particle size of ND aggregates at low pH would reduce the actual surface area available for the BSA adsorption, and thus reduce the BSA uptake and ND-BSA affinity.

Due to low surface charge and high surface energy, ND in the solution is in the form of aggregates rather than single crystals. Therefore the BSA adsorption behavior on ND is more dependent on the properties of ND aggregates. However, the surface properties of ND single crystal (such as surface hydrophobicity and charge) actually affects BSA adsorption behavior indirectly since ND aggregate is composed of single ND crystals.

It is interesting to find that, as shown in Figure 4.7, by adding BSA to ND suspension (ND:BSA=4:1, mass ratio) the zeta-potential is decreased to a lower level in comparison with either ND or native BSA. A further addition of BSA brings the zeta-potential even lower (ND:BSA=1:1, mass ratio). The addition of BSA into ND suspension gives rise to the formation of ND-BSA complex by virtue of high affinity of ND with BSA. For the conformation of

ND-BSA complex, it is possible that BSA is attached on the surface of ND aggregates but there must be other forms of ND-BSA complex because if BSA only exists on the ND surface the zeta-potential of ND-BSA should be residing between those of ND and BSA instead of decreasing to a lower level as shown in Figure 4.7. According to the previous research, proteins such as BSA could facilitate the dispersion of carbon nanotube (CNT) at the individual nanotube level by protein-assisted CNT exfoliation process [229-231]. The CNT aggregates were debundled in the presence of BSA so that CNT could be well-dispersed in solution. In view of the role that BSA plays in CNT dispersion, it is very likely that after attaching to BSA the strong binding force between ND and BSA might result in partial breakup of ND aggregates into relatively small ND-BSA aggregates. In case that ND aggregates break up into relatively small ND-BSA aggregates, more negative surface charge of ND might be exposed to the solution and then becomes “surface charge”. The zeta-potential measurement is performed by measuring the electrophoretic velocity of the nanoparticles in the solution. For ND aggregate, by binding with BSA to form relatively small ND-BSA aggregates, more negative surface charge exposition to the solution might be able to enhance the electrophoretic velocity of ND-BSA complex as compared with single ND aggregate. Therefore the zeta-potential of the ND-BSA is more negative.

4.4 Summary

In this chapter, the conformation of BSA in ND-BSA complex was investigated by a series of characterization techniques. The Fourier transform infrared spectroscopy shows an evident change in BSA secondary structure upon binding with ND. The UV-Vis and CD spectroscopies

further indicate that most BSA structural features could be preserved in ND-BSA complex. The fluorescence spectroscopy reveals that Trp residues in BSA are placed in a more hydrophobic environment in ND-BSA complex suggesting major protein unfolding is unlikely to occur. For the adsorption isotherms obtained at different pHs (3.5, 4.7, 6.0, 7.4, 9.0), both BSA uptake and the affinity between ND and BSA peak at pH 4.7 which suggests that hydrophobic force dominates the BSA adsorption process. The adsorption isotherms can be well fit by Freundlich but not Langmuir model. The zeta-potential measurements further suggest that after binding with BSA the strong binding force between ND and BSA might result in partial breakup of ND aggregates into relatively small ND-BSA aggregates. The results obtained have demonstrated that ND is able to preserve the albumin structural features to a large extent in ND-albumin complex and is very promising to be used for biosensor applications.

CHAPTER 5

PROTEIN-MODIFIED NANODIAMOND PARTICLES FOR LAYER-BY-LAYER ASSEMBLY

This chapter has been published in *Diamond and Related Materials*:

Wang H.D.; Yang Q.; Niu C.H.; Badea I. Protein-modified nanodiamond particles for Layer-by-Layer assembly. *Diamond Relat. Mater.* **2011**, 20, 1193-1198.

Contribution of the Ph.D. Candidate

Under the guidance of Prof. Yang and Prof. Niu, Hai-Dong Wang designed and conducted the experiment for this chapter as well as prepared manuscript for publication. Prof. Badea has also provided guidance in both experiment and manuscript revision.

5.1 Introduction

As discussed in Chapter 2, the conjugation of nanoparticles with biomacromolecules is an attractive area of research within nanobiotechnology [117]. In Chapter 4, it has been demonstrated that ND is an excellent platform for protein immobilization with high affinity and most of BSA structural features could be preserved upon immobilization. The nanoparticle-biomacromolecule complex, such as nanodiamond-biomacromolecule complex, is promising to be applied to the field of biosensor [26, 45, 232-234]. The assembly of nanoparticle-biomacromolecule on a surface could construct an ordered architecture with new

functionalities, which is important for bioelectronic, electronic, optobioelectronic, and photonic applications [117].

In this chapter, we report on the fabrication of ND-protein coatings on glass substrate through LBL assembly method. The LBL assembly technique has been widely used for thin film fabrication, which is convenient and economic to perform and easy to tune the film thickness [130]. Since ND has high affinity with biomacromolecules [24, 25], it might be possible that the ND-biomacromolecule complex is able to assemble on a substrate. In this work, the protein BSA was immobilized onto ND surface through chemical method and then the LBL assembly of NDBSA and ND was successfully performed on glass substrate. The work of this chapter has demonstrated the feasibility of using LBL assembly technique to prepare diamond coatings for protein immobilization, which has great potentials to be employed for biosensor applications.

5.2 Materials and Methods

5.2.1 Materials

ND particles with an average crystal size of 3-5 nm were purchased from Nanostructured & Amorphous Materials, Inc. They were produced by detonation method. BSA was purchased from Bio Basic (purity>98 %) and used as received. 1-(3-dimethylaminopropyl)-3-ethylcarbodiimide hydrochloride (EDC), *N*-hydroxysuccinimide (NHS), and 2-(*N*-Morpholino)ethanesulfonic acid (MES) were purchased from Sigma-Aldrich. All other chemicals and reagents are of analytical grade and used as received. The microscope glass slides were purchased from VWR International.

5.2.2 Immobilization of BSA onto ND Surface

BSA was chemically immobilized onto the surface of the pristine ND particles using zero-length crosslinker EDC, which is schematically illustrated in Figure 5.1.

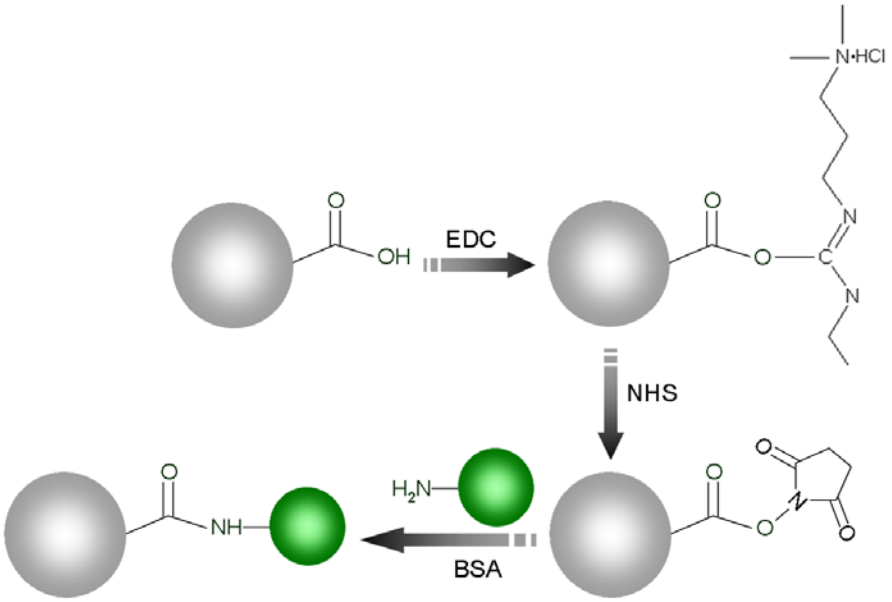

Figure 5.1 Schematic illustration of NDBSA synthesis process.

The synthesis procedure is detailed as follows: 0.75 g of BSA was dissolved in 100 ml of MES buffer (50 mM, pH 5.6) with stirring. 0.15 g of pristine ND was dispersed with ultrasonic treatment (Branson 2510 Sonication Bath) in another 100 ml of MES buffer (50 mM, pH 5.6) and then 0.345 g of NHS and 0.288 g of EDC were added in. The pristine ND suspension was then stirred at 4 ^{o}C for 1 h. After that the EDC-activated NDs were collected by centrifugation (15,000 rpm, 10 min) and quickly rinsed with MES buffer to remove unreacted EDC and NHS. The ND was finally dispersed into the BSA solution with ultrasonic treatment (Branson 2510 Sonication Bath) and stirred at 4 ^{o}C for 1.5 h. The as-prepared NDBSA was repeatedly centrifuged and

rinsed with deionized water (DI water) until the supernatant nearly has no UV-Vis absorbance at 280 nm (BSA has typical UV absorbance at 280 nm due to its aromatic moieties). Some NDBSA suspension was centrifuged and lyophilized immediately before the FT-IR and elemental analyses.

5.2.3 Layer-by-Layer Assembly of NDBSA and ND

Prior to LBL assembly, the glass slides were thoroughly cleaned with ethanol and dried by air flow. Then the NDBSA suspension (*ca.* 0.6 mg/ml) was dropped onto a glass slide and dried at room temperature to form a base layer for the following process. After that the glass slide with NDBSA base layer was dipped into ND suspension (*ca.* 0.6 mg/ml) for 10 min, rinsed in DI water for 1 min after no solution is dripping, and air dried to form an ND layer on NDBSA base layer. The glass slide with an ND layer on top of NDBSA base layer was then dipped into NDBSA suspension (*ca.* 0.6 mg/ml) for 10 min, rinsed in DI water for 1 min after no solution is dripping, and air dried. This cycle makes one bilayer of ND and NDBSA, denoted as $(NDBSA/ND)_1$ where the subscript 1 means one bilayer. The cycle was repeated until desired number of bilayers of coatings was reached, which is denoted as $(NDBSA/ND)_n$. In order to prevent the precipitation of NDBSA and ND suspensions, mild magnetic stirring was applied during the overall LBL assembly process.

The preparation of NDBSA/ND coatings is schematically illustrated in Figure 5.2. The NDBSA was deposited onto glass slides as base layer and then ND and NDBSA were alternately deposited to increase the coating thickness. The major force involved in the deposition process is

the hydrophobic interaction between ND and BSA [18, 88]. Please note that Figure 5.2 only shows one bilayer of NDBSA/ND deposited on NDBSA base layer.

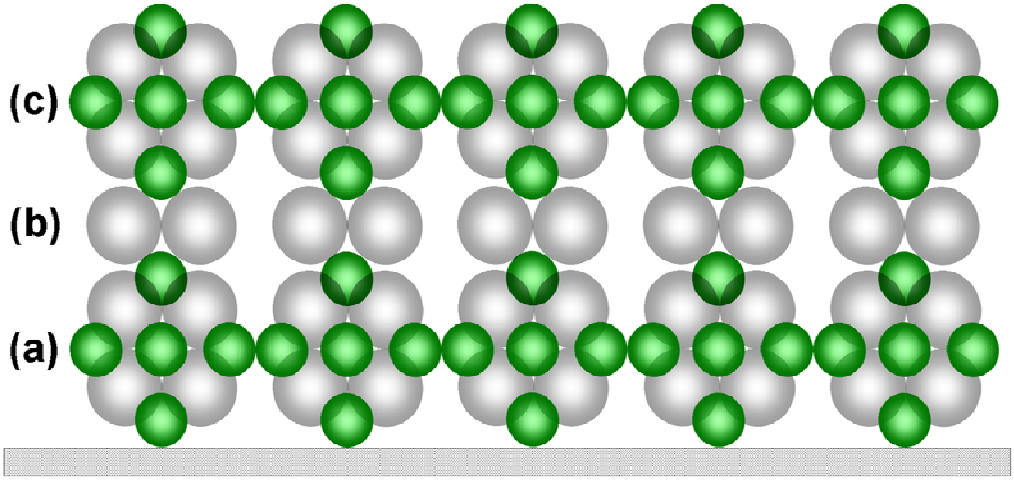

Figure 5.2 The schematic illustration of NDBSA/ND coating preparation process. (a) NDBSA base layer; (b) ND layer deposited through ND-BSA interaction; (c) NDBSA layer deposited through ND-BSA interaction.

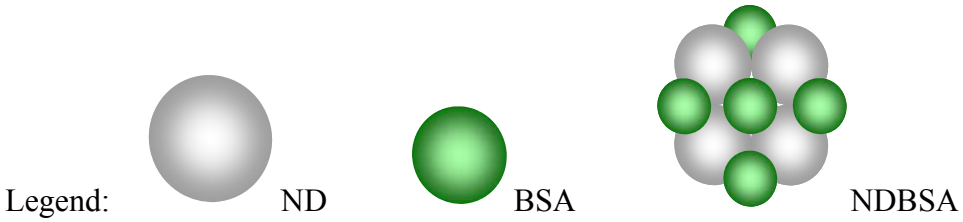

5.2.4 Characterizations

Fourier transform infrared spectrum (FT-IR) was recorded on a JASCO FT/IR-4100 spectrometer by KBr method (KBr:Sample = 100:1, mass ratio). For each measurement, a total of 64 scans were averaged with a resolution of 4 cm^{-1}. This KBr-based method has been proved not to introduce artificial structural changes to protein in previous analyses [191, 192]. For the second derivative spectrum of BSA in NDBSA, the reference spectrum (the ND/KBr mixture

possessing identical amount of ND with that in NDBSA/KBr mixture) was recorded in the identical manner and subtracted from that of NDBSA. Then the baseline of spectrum was corrected according to the criterion that a straight baseline was obtained in the region from 1750 to 2000 cm^{-1}, which is critical to obtain correct structural information using the second-derivative analysis method [191, 193]. Second derivative spectra were obtained using spectrum analysis software on JASCO FT-IR spectrometer.

Absorption spectra of NDBSA suspensions (*ca.* 0.02 mg/ml) and NDBSA/ND coatings on glass substrate were monitored using a UV-Vis spectrophotometer (Shimadzu UVmini-1240). For the spectrum of BSA in NDBSA, in order to remove the light scattering effect, the contribution of light scattering from ND is determined by plotting $\log_{10}$(absorbance) as a function of $\log_{10}$(wavelength) above 310 nm and then extrapolating linearly to shorter wavelengths since BSA doesnot show absorbance at wavelength higher than *ca*. 310 nm [235]. Since the growth of NDBSA/ND coatings during LBL assembly process might result in the increase in coating density and thickness, the absorption spectra measurement was used to characterize this coating growth process. Each measurement (for both solution and coating) was performed in triplicate and the spectrum provided was the average. For the spectra of NDBSA/ND coatings, the glass slide without coating was used as reference.

Zeta-potential and size measurements of ND and NDBSA were performed on a Malvern Zetasizer Nano ZS instrument over a pH range approximately from 9.0 to 3.0 adjusted by an autotitrator using HCl and NaOH aqueous solutions. After reaching the desired pH by titration, the solution was left to equilibrate for 1 min before taking measurement. Each measurement was

performed in triplicate with the data presented being the average.

Surface morphology of NDBSA/ND coatings was observed using a scanning electron microscope (SEM, Philips 505). The coatings to be observed were sputter-coated with a gold film prior to the SEM observation.

5.3 Results and Discussion

5.3.1 FT-IR Characterization

The FT-IR spectra of ND and NDBSA are given in Figure 5.3 (a). Pristine ND surface contained oxygen-containing surface groups such as hydroxyls and carboxyls as evidenced in Figure 5.3 (a) (*ca.* 3450 cm^{-1} for hydroxyl stretching vibration and *ca.* 1730 cm^{-1} for carbonyl stretching vibration). These oxygen-containing surface groups could be easily conjugated with primary amines on BSA with the aid of zero-length crosslinker EDC. After the chemical immobilization of BSA onto pristine ND surface, NDBSA showed strong characteristic peaks of BSA: amide I (*ca.* 1660 cm^{-1}) and amide II (*ca.* 1550 cm^{-1}), which suggests that BSA was successfully introduced onto ND surface. According to the results of elemental analysis (Heraeus Vario EL III Elemental Analyzer), the mass ratio of BSA in NDBSA was approximately 42%, which is 20% higher than the BSA immobilized by physical adsorption in our recent work [18] and more than 2.5 times that of the protein immobilized on NDs using physical methods in other research [22, 88].

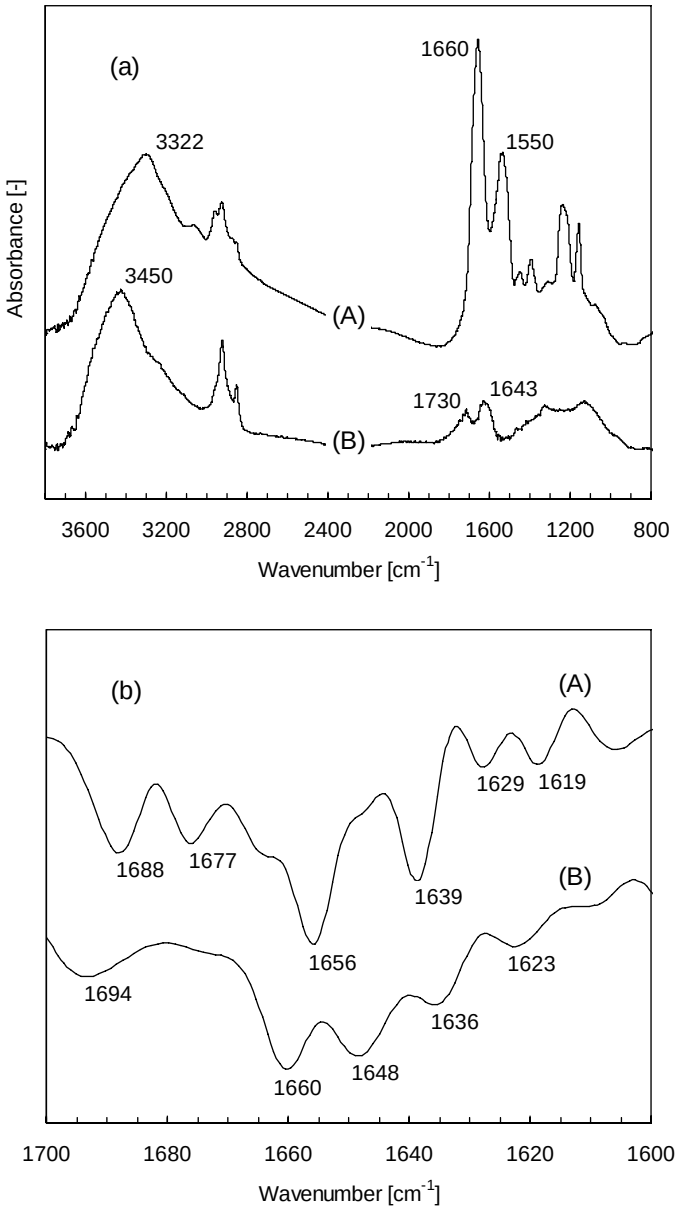

Figure 5.3 (a) FT-IR spectra of NDBSA (A) and pristine ND (B); (b) Second derivative spectra of BSA in NDBSA (A) and native BSA (B).

To further investigate the BSA conformational changes upon chemical immobilization onto ND surface, the second derivative spectra were taken and given in Figure 5.3 (b). Among all amide bands (amide I, II, and III), amide I region (1600~1700 cm^{-1}, mainly due to C=O stretching vibration) has been proved to be helpful for protein conformational studies since it is

the most sensitive to protein secondary structure changes [196]. According to previous research [200, 202], the assignment of secondary structures in amide I region is as the following: 1695-1663 cm^{-1} for β-sheet or β-turn structures, 1662-1650 cm^{-1} for α-helices, 1648-1644 cm^{-1} to random chains, 1642-1618 cm^{-1} for β-sheets. Bands at lower wavenumbers (*ca.* 1616 cm^{-1}) have been assigned to side chain moieties. For both native BSA and NDBSA, α-helix dominated the spectra. Compared with native BSA, the BSA in NDBSA underwent changes in both shape and peak position. Peak intensities for all structures (α-helices, β-sheets, and β-turns) in NDBSA were found to be relatively higher than that of native BSA. Moreover, a new peak at *ca.* 1677 cm^{-1}, which could be assigned to β-turn structure, appeared in NDBSA; while random chain structure (1648 cm^{-1}) in native BSA disappeared in NDBSA. All these changes occurred in the secondary structure of protein after being chemically immobilized onto ND surface suggest that chemical immobilization of protein onto ND surface provides strong linkage between ND and protein.

5.3.2 Absorption Spectra

The absorption spectra of NDBSA and ND are given in Figure 5.4 (a). Since pure diamond is a wide bandgap semiconductor (5.45 eV), it should not have any optical absorption beyond 300 nm (4.13 eV) [19]. However, because of the existence of sp^2 carbon on ND surface, its optical absorption actually extends from UV to near-IR range. As can be seen from Figure 5.4 (a), similar to pristine ND, the NDBSA showed a featureless spectrum, which might be attributable to the light scattering of ND particles. After removing the light scattering effect, the absorption spectrum of BSA in NDBSA is given in Figure 5.4 (b) where BSA showed an aromatic residue

absorption band at *ca*. 295 nm. The inset of Figure 5.4 (b) is the absorption spectrum of native BSA whose aromatic residue resided at *ca.* 280 nm. The BSA immobilized onto ND surface showed a red-shift for aromatic absorption in comparison with native BSA. The red-shift means that after the chemical immobilization of BSA on ND surface, the aromatic residue of BSA was located in a more hydrophobic environment due to tertiary structure changes of BSA upon immobilization onto ND surface. This also suggests that BSA unfolding did not occur and its structure remained stable because no blue-shift in aromatic absorption band was observed. This is of great importance when it comes to biosensor applications because preventing protein tertiary structure from unfolding could help retaining its functions. These findings are consistent with our previous research [18], where it was found that most of BSA structural features could be reserved upon being physically adsorbed onto ND surface. The retention of original structure of proteins (albumin, lysozyme, and etc.) in the nanoparticle-protein complex could possibly be attributable to the high curvature of nanoparticles (ND in the present work) [118, 221]. The ND particle in the present work had a single crystal size of *ca.* 5 nm. Thus the ND aggregates consisting of ND crystals would exhibit very high local curvature, facilitating the retention of albumin structural features.

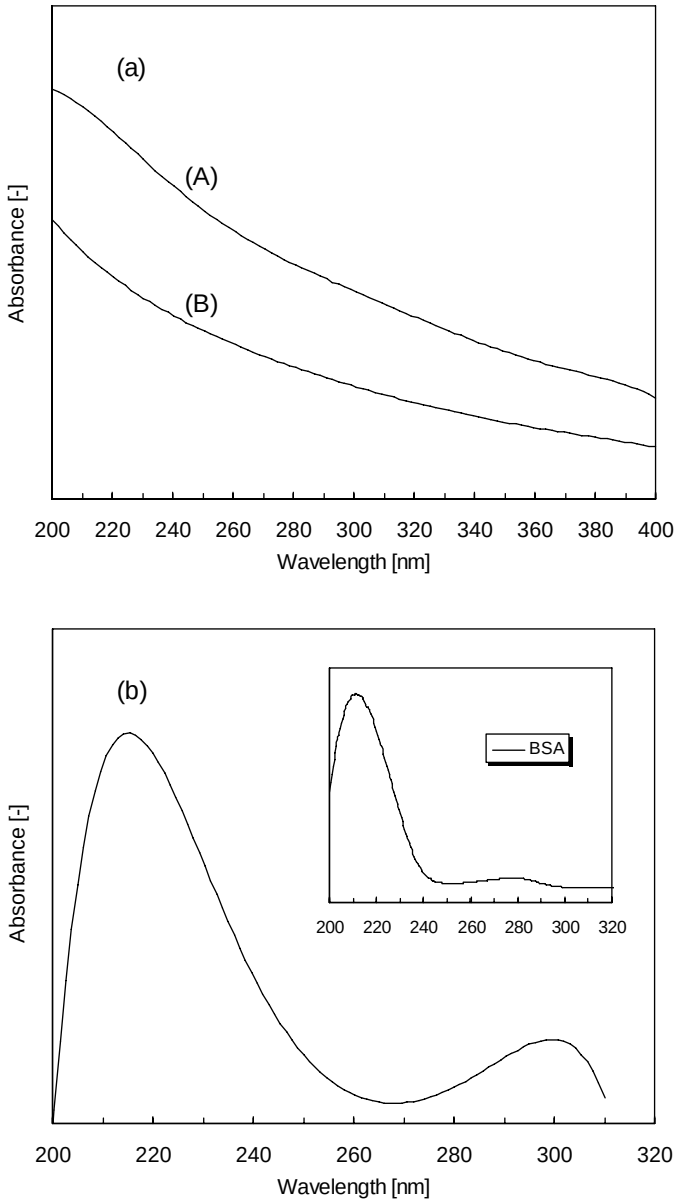

Figure 5.4 (a) Absorption spectra of NDBSA (A) and pristine ND (B); (b) Absorption spectra of BSA in NDBSA (after removing the light scattering effect) and native BSA (inset).

5.3.3 Zeta-potential and Size Measurements

The results of zeta-potential measurements are shown in Figure 5.5 (a). The ND surface was always negatively charged over the whole pH range under investigation while BSA showed an

isoelectric point (pI) at pH 4.6, which is consistent with previous report [226]. The negatively charged ND surface was attributable to the existence of oxygen-containing surface groups such as carboxyls and hydroxyls. With the decrease of pH, the zeta-potential of ND increased sharply, which might be attributable to the protonation of negatively charged groups on ND surface. It is interesting to note that after immobilizing BSA onto ND surface, the NDBSA showed an even lower zeta-potential in comparison with pristine ND over the whole pH range under investigation. As shown in Figure 5.5 (b), the ND had a particle size ranging from *ca.* 300 to 900 nm when pH changed from 9.0 to 3.0 as determined by dynamic light scattering. According to manufacturer's data, the single ND crystal is approximately 5 nm in diameter and therefore the size given by dynamic light scattering indicates that ND particles formed aggregates in suspension. According to the previous research [230], proteins such as BSA could facilitate the dispersion of carbon nanotube (CNT) at the individual nanotube level by protein-assisted CNT exfoliation process, where the CNT aggregates were debundled in the presence of BSA. Similarly, in the present work, the chemically immobilized BSA might be able to break up the ND aggregates and then more negative ND surface charge was released. As a result, the electrophoretic velocity of NDBSA in the solution increased so that the zeta-potential of the NDBSA was more negative.

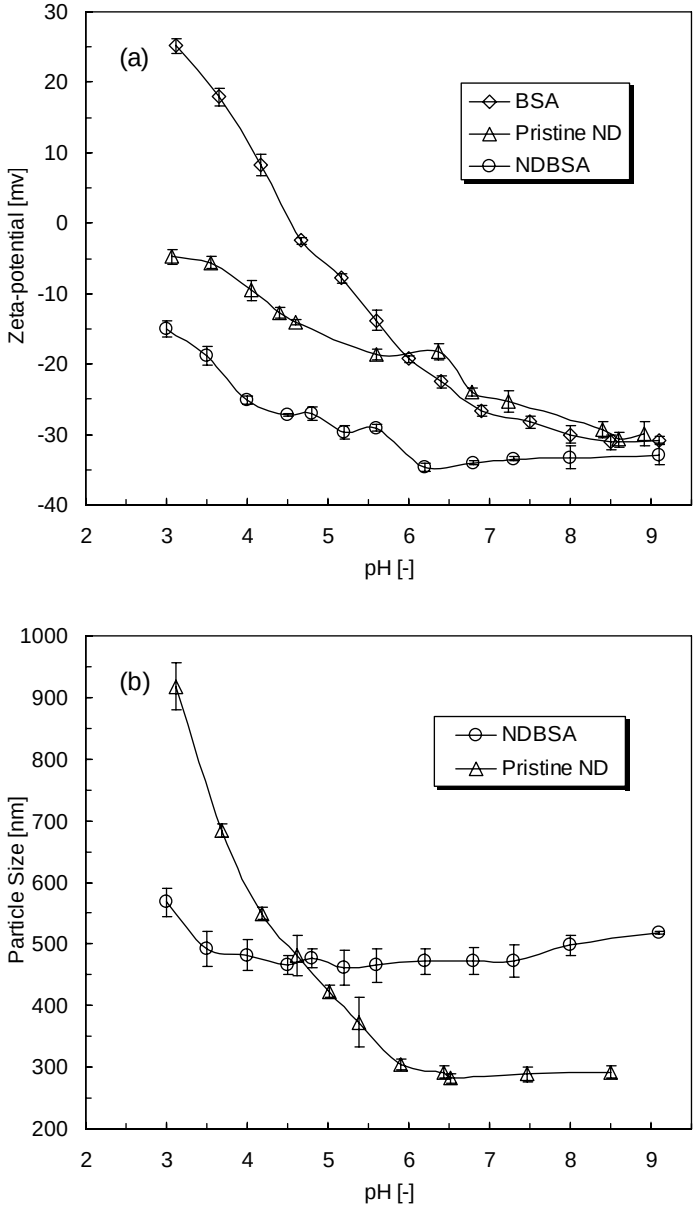

Figure 5.5 (a) Zeta-potentials of BSA, pristine ND, and NDBSA; (b) Particle sizes of NDBSA and pristine ND. The error bar represents standard deviation.

5.3.4 NDBSA Self-assembly in Solution and Layer-by-Layer Assembly on Glass Substrate

The functionalization of nanoparticles with biomolecules could lead to biomolecule-nanoparticle recognition interactions and thus to self-assembly [117] as shown in

Figure 5.5 (b). For a single BSA molecule, it has geometric dimensions of 9.5×5.0×5.0 nm^3 [222]. Previous research indicated that BSA could be adsorbed onto a surface in a side-on fashion (adsorption area: 9.5×5.0 nm^2) or end-on fashion (adsorption area: 5.0×5.0 nm^2) [223]. Considering a specific surface area of *ca.* 300 m^2/g for ND (given by manufacturer), the BSA adsorption density required for an adsorption monolayer on the ND surface was determined as 2.1 mg/m^2 and 3.6 mg/m^2 for side-on and end-on modes, respectively. The BSA packing density on ND surface in this work was determined to be *ca.* 2.3 mg/m^2, which means it might be a mix of side-on and end-on modes, leaving part of ND surface unoccupied. The unoccupied ND surface could interact with BSA due to strong ND-protein interaction [18, 88]. Therefore, the NDBSA particle size was *ca.* 470 nm at around neutral pH, which is much higher than that of pristine ND (*ca.* 280 nm) at the same pH (Figure 5.5 b), suggesting the occurrence of self-assembly among different NDBSA particles through ND-protein interactions. It is known that BSA has the most compact structure in normal form (*ca.* pH 4.3~8.0) while as pH shifts higher or lower the BSA molecule would experience less compact conformation till unfolding [219, 220]. In the present work, as pH shifted higher than *ca.* 7.5 or lower than *ca.* 4.5, the NDBSA particle size increased rapidly to approximately 600 nm. This size change agreed very well with pH-dependence of BSA conformational changes, suggesting that the pH-induced BSA conformational changes were able to affect the NDBSA assembly.

Though NDBSA could assemble by itself through ND-BSA interaction, in the present work pristine ND was used to perform LBL assembly with NDBSA because pristine ND has unoccupied surface, which would enhance the ND-protein interaction and facilitate the coating

fabrication by LBL assembly.

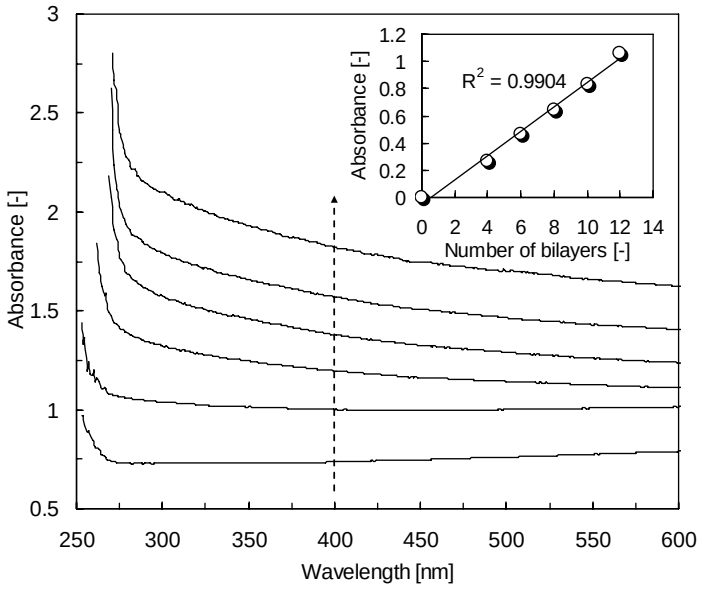

Figure 5.6 Absorption spectra of NDBSA base layer and NDBSA/ND LBL assembled coatings with 4, 6, 8, 10, and 12 bilayers of NDBSA/ND deposited on NDBSA base layer (from bottom to top as indicated by arrow). Inset: the absorbance of coating increases linearly with the increase of bilayers at 400 nm (the NDBSA base layer absorbance is subtracted from each measurement).

The growth of coating by LBL assembly is evidenced by UV-Vis absorption spectra (Figure 5.6). The NDBSA/ND coatings showed sharp absorption band extending until *ca.* 300 nm, which was mainly attributable to ND absorption in UV range. The absorption above 300 nm was mostly from sp^2 carbon present on ND surface since BSA nearly has no absorption in this range. The glass slide with only NDBSA base layer had the lowest absorbance while with the increase of coating thickness to 4, 6, 8, 10, and 12 bilayers of ND and NDBSA, the absorbance increased obviously. The absorbance of coating was found to increase linearly at 400 nm with the increase of bilayers (inset in Figure 5.6), suggesting that a constant amount of NDBSA/ND was deposited

for each bilayer deposition. Moreover, the coatings produced by this method could resist repeated washing by DI water, suggesting that the coatings were stable and the non-covalent interaction between NDBSA and ND was strong.

The surface morphology of the fabricated coatings by LBL assembly is shown in Figure 5.7. The coating with only NDBSA base layer featured loose structures with interconnected narrow pores. After 12 bilayers of NDBSA/ND being deposited onto the base layer, the number of interconnected pores was reduced to a large extent so that the coating becomes denser. Since the increase of coating thickness resulted in a denser structure, more densely-organized coatings could be obtained by increasing the number of bilayers deposited. Cross-sectional SEM observation showed that the NDBSA base layer had a thickness of *ca.* 1.0 μm while the thickness for $(NDBSA/ND)_{12}$ was approximately 3 μm. Therefore each bilayer had an average thickness of *ca.* 170 nm, which was much smaller than the size of aggregates for NDBSA and pristine ND as shown in Figure 5.5 (b). It is likely that the large aggregates of NDBSA and pristine ND could be easily washed away and only small aggregates could stay on the coating in LBL assembly process. In addition, the NDBSA base layer was loosely-organized with interconnected pores (pore areas were less covered or even uncovered by NDBSA base layer), thus some of NDBSA or pristine ND aggregates were able to be deposited into the pores instead of on top of the NDBSA base layer during the following LBL assembly process, resulting in smaller thickness increase for each bilayer.

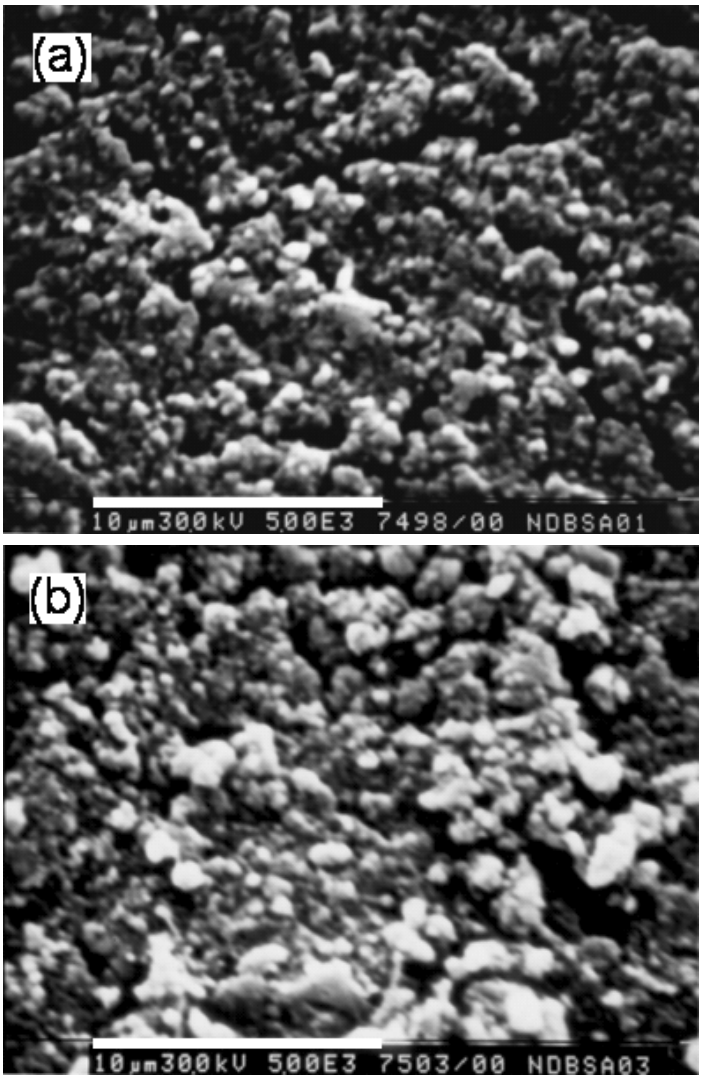

Figure 5.7 The surface SEM images of NDBSA base layer (a) and NDBSA/ND coatings with 12 bilayers of NDBSA/ND plus NDBSA base layer (b). The scale bar is 10 μm.

5.4 Summary

In this chapter, the protein BSA has been chemically immobilized onto pristine ND surface, which was evidenced by FT-IR and UV-Vis spectroscopies. The LBL assembly properties of NDBSA with pristine ND were investigated on glass substrates. The NDBSA/ND coatings

fabricated by LBL assembly method were stable and more densely-organized coating structures could be obtained by increasing the number of bilayers deposited. The present LBL assembly method for ND-protein coating fabrication could be easily employed to prepare biomacromolecule-functionalized ND films for biosensor applications. This work has demonstrated that the LBL assembly is a facile approach to fabricate ND coatings and it could be a desirable substitute for the traditional CVD process to prepare diamond coatings for biological applications.

CHAPTER 6

PREPARATION OF NANODIAMOND THIN FILMS BY LAYER-BY-LAYER ASSEMBLY

This chapter has been submitted as:

Wang H.D.; Yang Q.; Niu C.H. Preparation of nanodiamond thin films by Layer-by-Layer assembly. 2011.

Contribution of the Ph.D. Candidate

Under the guidance of Prof. Yang and Prof. Niu, Hai-Dong Wang designed and conducted the experiment for this chapter as well as prepared manuscript for publication.

6.1 Introduction

In Chapter 5, the ND-protein complexes were successfully assembled, in an LBL assembly fashion, into films on glass substrate through strong ND-protein interaction. In Dai *et al.*'s work [17], ND films were prepared on glass substrates by simply drying ND aqueous dispersion and they suggested that the hydrogen bonding among NDs could be a major force accounting for the ND assembly into films. Since NDs have strong hydrogen bonding for assembly, it might be feasible to combine hydrogen bonding among NDs with LBL assembly technique to prepare ND thin films.

In this chapter, we report on the preparation of ND thin films by LBL assembly technique. The

ND thin films were deposited on glass slide mainly by virtue of hydrogen bonding among ND particles (Figure 6.1), where the film morphology could be tuned by changing the number of bilayers deposited. In addition, the film growth mechanism and morphology with different preparation conditions were discussed in detail.

6.2 Materials and Methods

6.2.1 Materials

Detonation nanodiamond particles (NDs), which have an average crystal size of 3-5 nm, were purchased from Nanostructured & Amorphous Materials Inc. and used without further treatment. The microscope glass slides were purchased from VWR International and used as substrate materials. All other reagents are of analytical grade and used as received. The water used throughout the experiment is from a Milli-Q system.

6.2.2 Preparation of ND Thin Films by Layer-by-Layer (LBL) Assembly

Prior to LBL assembly, the glass slides were cleaned by piranha solution using method similar to previous reports [236, 237]. The microscope glass slides were dipped into piranha solution (concentrated sulfuric acid and 30% hydrogen peroxide, 3:1 by volume) and then boiled for 90 min. After reaction the glass slides were rinsed with a large amount of Milli-Q water and then dried by nitrogen gas.

LBL assembly of NDs was performed on piranha-solution-treated glass slides. First, ND aqueous dispersions (*ca.* 0.45 mg/ml) were prepared with ultrasonic treatment using Milli-Q

water and the dispersion pH was adjusted by HCl or NaOH solution. Second, the treated glass slide was dipped into ND dispersion (pH 3.5) for 10 min and dried at ambient condition, which was then rinsed with Milli-Q water for 1 min and dried by nitrogen gas. Third, the glass slide was then exposed to ND dispersion (pH 4.0 or pH 7.5) again for 10 min and dried at ambient condition, which was then rinsed with Milli-Q water for 1 min and dried by nitrogen gas. The second and third steps make one bilayer of NDs. These two steps were repeated until the desired number of bilayers was reached. The films prepared were denoted as ND $(3.5/4.0)_n$ and ND $(3.5/7.5)_n$, respectively where subscript *n* represents the number of bilayers deposited while two numbers denote two successive dispersion pHs in the preparation of one bilayer. In order to prevent the precipitation of ND dispersions, mild magnetic stirring was applied throughout the LBL assembly process. The ND thin film formation through LBL assembly is schematically illustrated in Figure 6.1, where hydrogen bonding might be the major force involved in the LBL assembly process.

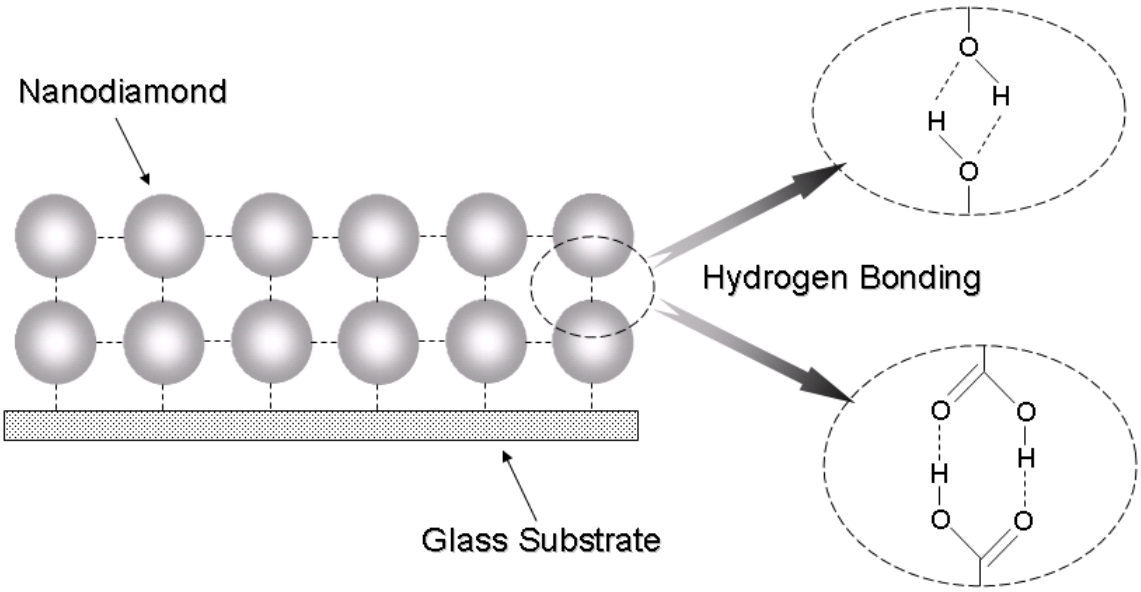

Figure 6.1 The ND thin film formation through LBL assembly, where the hydrogen bonding might mainly account for the LBL assembly process.

As control group, ND aqueous dispersions (*ca.* 0.45 mg/ml) at pHs 3.5, 4.0 and 7.5 were also made into cast films on piranha-solution-treated glass slides at ambient condition, respectively. They are denoted as ND (3.5), ND (4.0), and ND (7.5).

6.2.3 Characterizations

FT-IR spectrum of ND was recorded on a JASCO FT/IR-4100 spectrometer. 1 mg of sample was ground with 100 mg of dried KBr to form homogeneous powder. After that approximately 25 mg of powder was made into pellet which was subjected to FT-IR measurement. For each measurement, a total of 32 scans were averaged with a resolution of 4 cm^{-1}. Raman analysis of ND was carried out on a Renishaw inVia Raman spectroscope with excitation wavelength at 514 nm. The UV-Vis spectra of the ND LBL films and cast films were recorded on a UV-Vis

spectrophotometer (Shimadzu UVmini-1240). Before measurement, the baseline was corrected for glass slide to guarantee that the glass slide has no interference with absorption spectra of ND LBL films and cast films in the entire wavelength range under investigation. Each spectrum was measured in triplicate with the data presented being the average. The size and zeta-potential measurements were performed on a Zetasizer Nano ZS instrument (Malvern) over a pH range from approximately 7.5 to 3.5 at 25 ^{o}C. Each data point is the average of 3 measurements. The morphologies of ND LBL thin films and cast films prepared were observed on a scanning electron microscope (JEOL JSM 840A). The morphology of ND particles was observed on a transmission electron microscope (Philips CM10).

6.3 Results and Discussion

6.3.1 Chemical and Physical Characterizations on ND

The FT-IR spectrum of ND is given in Figure 6.2 (a). The surface of detonation ND was functionalized with oxygen containing groups in the process of strong oxidizing acid treatment by manufacturer. As a result, the ND in this work is rich in oxygen-containing surface groups such as hydroxyls and carboxyls as evidenced in Figure 6.2 (a) (*ca.* 3460 cm^{-1} for hydroxyl stretching vibration and *ca.* 1730 cm^{-1} for carbonyl stretching vibration). The carboxyl and hydroxyl could participate in hydrogen bonding formation which might be the major force involved in the LBL assembly of ND films. In Raman spectrum as shown in Figure 6.2 (b), the spectrum is composed of two bands, approximately at 1330 cm^{-1} and 1600 cm^{-1}. The 1330 cm^{-1} band (D band) is the characteristic of sp^3 bonded carbon while the 1600 cm^{-1} band (G band)

corresponds to sp^2 bonded carbon [17]. The existence of sp^2 bonded carbon could give rise to π-π interaction among NDs, which might also contribute to ND-ND interaction during LBL assembly process to some extent. In addition, there might be a certain extent of van der Waals force contributing to ND-ND interaction for LBL assembly process.

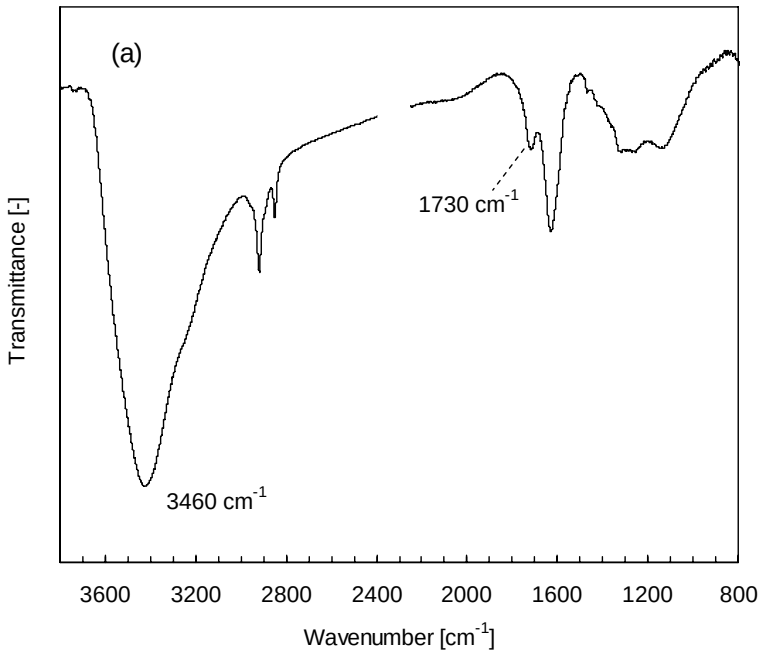

Figure 6.2 FT-IR spectrum (a) and Raman spectrum (b) of ND.

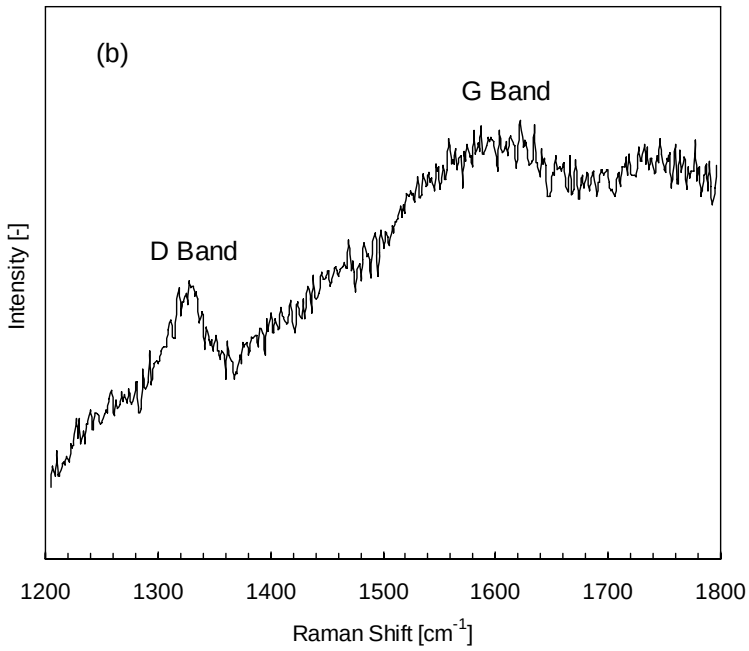

Figure 6.2 (*Continued*).

In the present work, the ND surface is terminated by carboxyls and hydroxyls which render its surface negatively charged over the entire pH range under investigation as shown in Figure 6.3 (a).

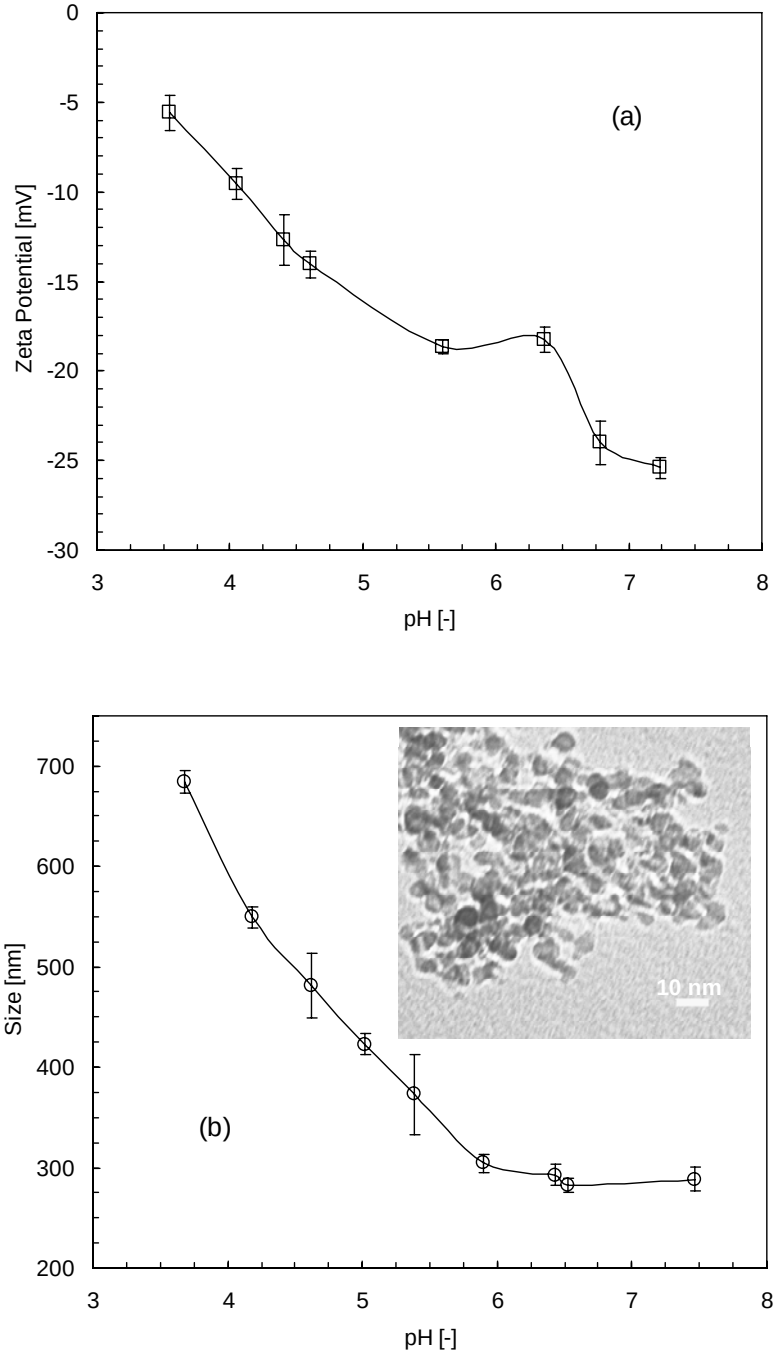

Figure 6.3 Zeta-potential (a) and particle size (b) of ND with pH changes. The inset in (b) is TEM image of NDs. The error bar represents standard deviation.

With decrease of pH, the ND surface zeta potential becomes less negative due to the protonation of carboxyls (Figure 6.3 a). The ND has a near spherical morphology as clearly

shown in TEM images (inset, Figure 6.3 b). The single ND crystal size from TEM image (inset, Figure 6.3 b) is smaller than 10 nm which is reasonably consistent with the data provided by ND manufacturer (average crystal size: 3-5 nm). The small crystal size of NDs would give rise to a strong tendency to form aggregates by interactions among NDs such as hydrogen bonding, π-π interaction, and van der Waals force, as indicated by size measurement (Figure 6.3 b). It could be seen from Figure 6.3 (b) that with pH decrease ND gradually forms aggregates, suggesting the importance of surface charge state in stabilizing ND crystals. As pH shifts to *ca.* 3.5, the zeta potential drops down to as low as *ca.* -5 mV resulting in large ND aggregates with average size of *ca.* 700 nm while at around neutral pH (*ca.* 7.5) highly negatively charged ND crystal (*ca.* -30 mV) is relatively well dispersed with average size of *ca.* 280 nm.

6.3.2 Preparation of ND Thin Films by Layer-by-Layer (LBL) Assembly

In the preparation of ND thin films by LBL assembly, three pHs were used for ND dispersions: pHs 3.5, 4.0, and 7.5. At pHs 3.5 and 4.0, ND surface negative charge is relatively low with larger aggregates while at pH 7.5 relatively high surface negative charge results in smaller ND aggregates. To investigate the influence of ND surface charge state on ND LBL assembly process, one ND dispersion was kept at pH 3.5 while the second one had a pH of 4.0 or 7.5.

The surface morphologies of two LBL films with 3 and 15 bilayers are given in Figure 6.4.

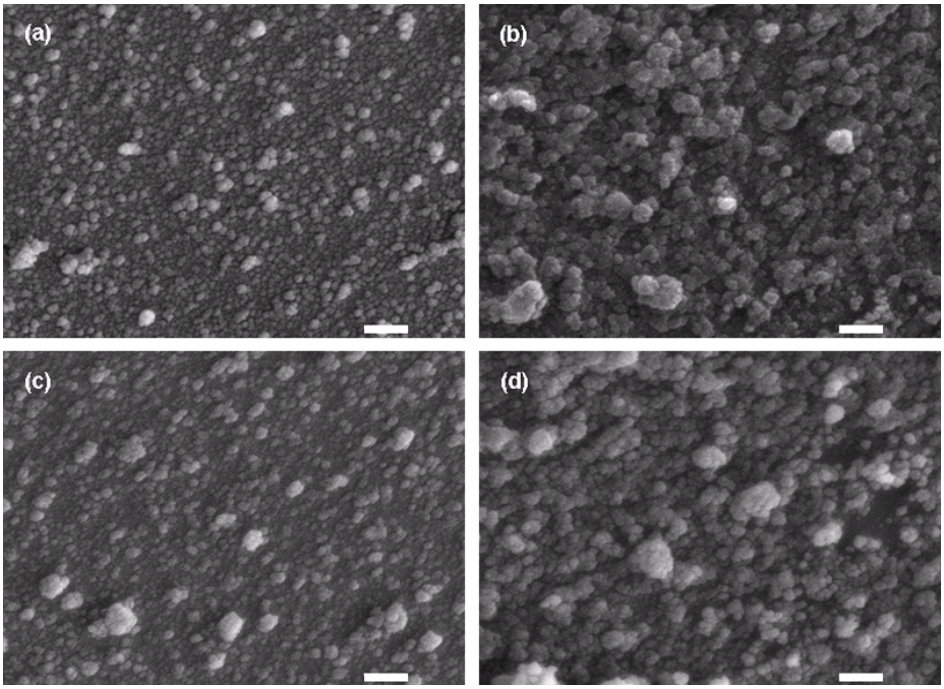

Figure 6.4 Surface SEM images for ND $(3.5/4.0)_3$ (a), ND $(3.5/4.0)_{15}$ (b), ND $(3.5/7.5)_3$ (c), and ND $(3.5/7.5)_{15}$ (d). Size bar represents 1 micron in length.

The ND (3.5/4.0) films have relatively higher particle density than ND (3.5/7.5) films of the same number of bilayers. For ND (3.5/4.0) LBL assembly, the two ND dispersions were kept at pHs 3.5 and 4.0, rendering electrostatic repulsion among NDs very low so that hydrogen bonding is given full play. As a result, relatively more ND could be deposited in LBL assembly by hydrogen bonding compared with ND (3.5/7.5). In addition, it can be seen from morphologies of ND thin films with 3 and 15 bilayers that ND LBL films have nanostructures which could be tuned by adjusting the number of bilayers deposited. The high surface curvature of nanostructure has been reported to be able to retain the structural features of biomacromolecules attached on the surface [18, 118, 221]. Therefore it is reasonable to believe that the ND LBL film could be a promising candidate for biomacromolecule immobilization. As control group, the surface

morphologies of cast films are given in Figure 6.5, which all feature micron-sized aggregates due to strong interactions among NDs.

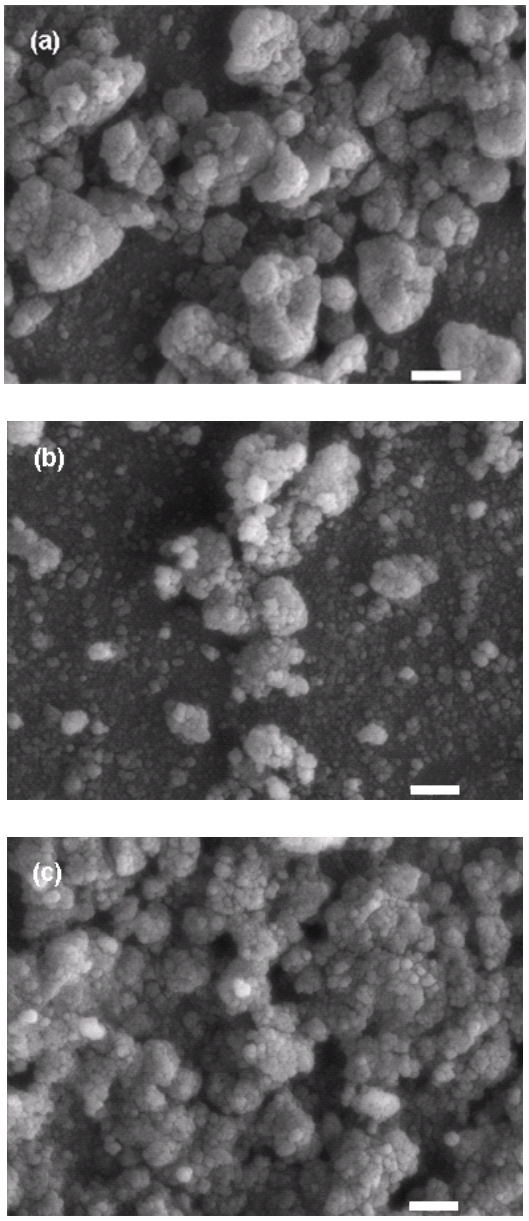

Figure 6.5 Surface SEM images for cast films ND (3.5) (a), ND (4.0) (b), and ND (7.5) (c). Size bar represents 1 micron in length.

Figure 6.6 shows cross-sectional image of ND (3.5/4.0) LBL film with 15 bilayers. The film shows densely-organized cross-sectional structures with a film thickness of *ca.* 2 μm. ND

$(3.5/7.5)_{15}$ film shows similar cross-sectional structure and thickness. Based on this, averagely, each bilayer deposition contributes to an increment of *ca.* 130 nm in film thickness. As given in Figure 6.3 (b), the average size of ND aggregates is in the range of hundreds of nanometers which indicates that only small ND aggregates could be deposited onto the film during LBL assembly.

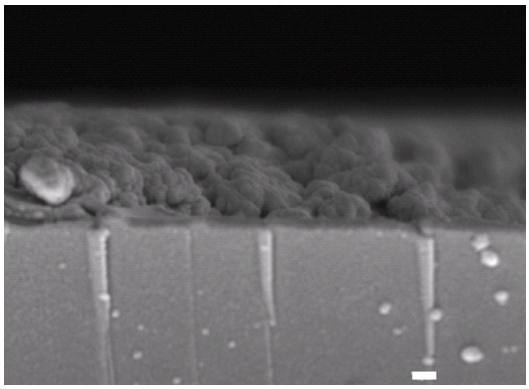

Figure 6.6 Cross-sectional SEM image for ND LBL film ND $(3.5/4.0)_{15}$. Size bar represents 1 micron in length.

The ND thin film growth during the LBL assembly process is demonstrated by UV-Vis absorption spectra as illustrated in Figure 6.7. Since pure diamond is a wide bandgap semiconductor (5.45 eV), it should not have any optical absorption beyond 300 nm (4.13 eV) [19]. However, because of the existence of sp^2 carbon on ND surface, its optical absorption actually extends from UV to near-IR range. For ND (3.5/4.0) films, there is a broad band ranging from 275~340 nm while for ND (3.5/7.5) films all spectra feature absorption bands at 295~300 nm, which might be assigned to π-π^* transition of ND surface graphite layer [238]. The broader ND (3.5/4.0) absorption bands, in comparison with those of ND (3.5/7.5), might be attributable to more densely distributed particles in ND (3.5/4.0) structure as illustrated and discussed in Figure

6.4. Due to relatively higher particle density, a higher level of conjugation renders the π-π^* transition of ND surface graphite layer in ND (3.5/4.0) films lower in energy than that of ND (3.5/7.5) films. Therefore, the ND (3.5/4.0) films show a broader absorption band. The above observations are consistent with previous work dealing with UV absorption spectra of gold nanoparticles [239]. For cast films, the absorption band of ND (7.5) film (*ca.* 273 nm) has a slight red shift compared with that of ND (3.5) and ND (4.0) films (*ca.* 270 nm), which could be explained in the same manner taking into the consideration that ND (7.5) has a relatively higher particle density than those of ND (3.5) and ND (4.0) (see Figure 6.5).

In order to have an understanding of the film growth rate for two LBL film preparation conditions during the LBL assembly process, the absorbance for two LBL films at 300 nm in Figure 6.7 is plotted against number of bilayers in LBL films (see Figure 6.8), using the similar method as employed by previous work dealing with LBL films of carbon nanotube and polyelectrolyte [141, 240, 241].

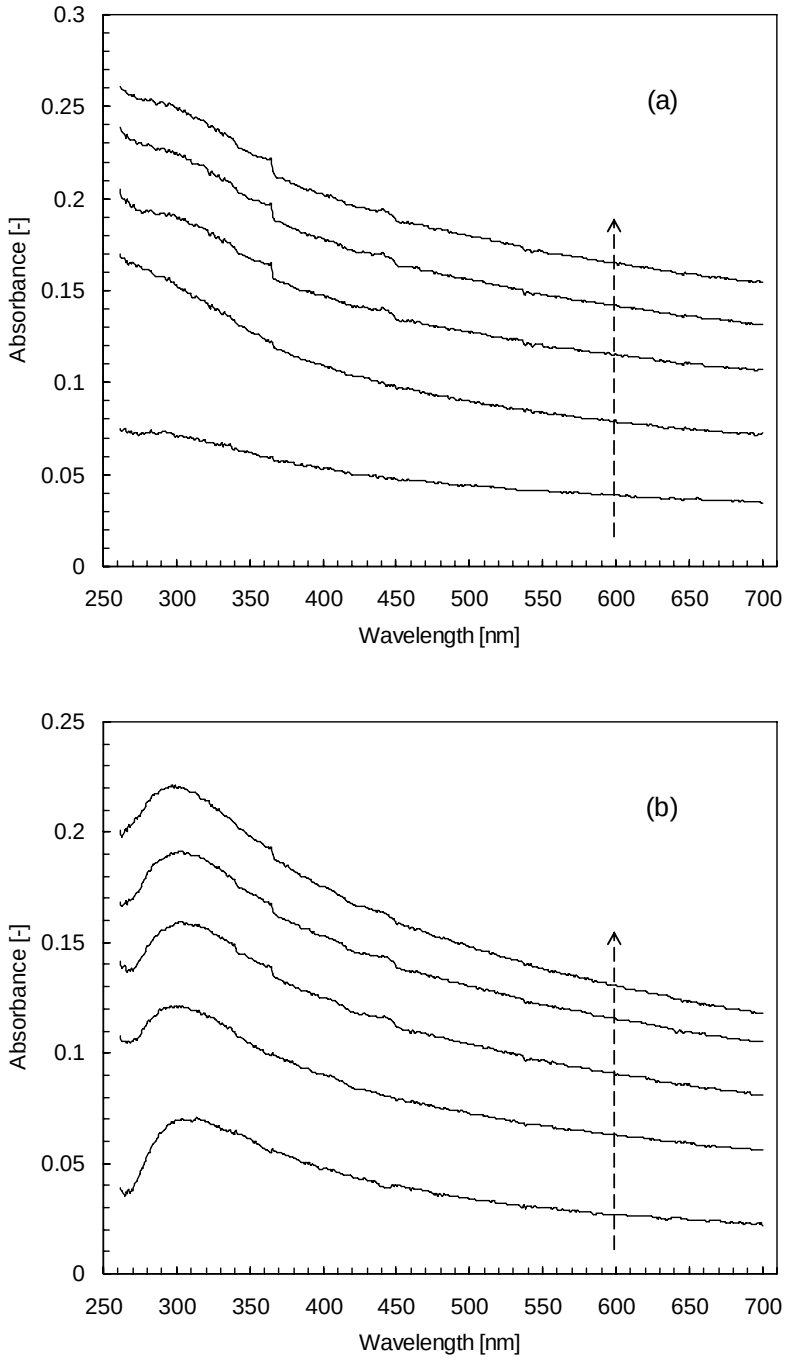

Figure 6.7 Absorption spectra of ND (3.5/4.0) (a), ND (3.5/7.5) (b), and ND cast films (c). The curves from bottom to top are 3, 6, 9, 12, and 15 bilayers of ND LBL films in (a) and (b); the curves from bottom to top are cast films ND (4.0), ND (3.5), and ND (7.5) in (c).

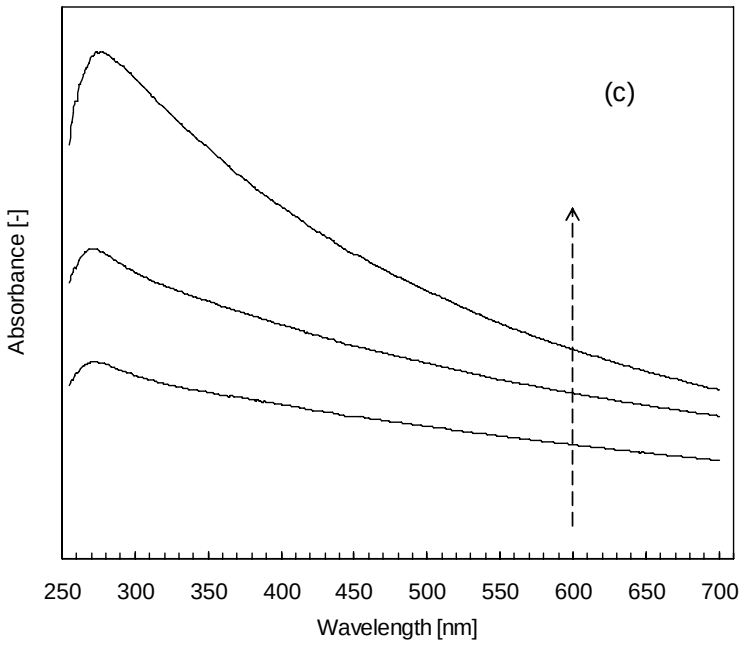

Figure 6.7 (*Continued*).

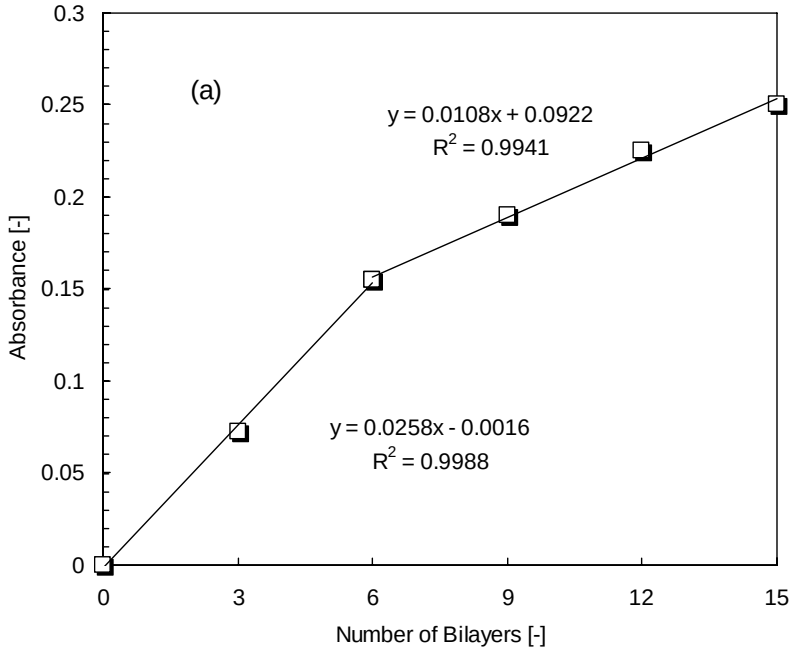

Figure 6.8 Absorbance for ND (3.5/4.0) (a) and ND (3.5/7.5) (b) at 300 nm with different bilayers.

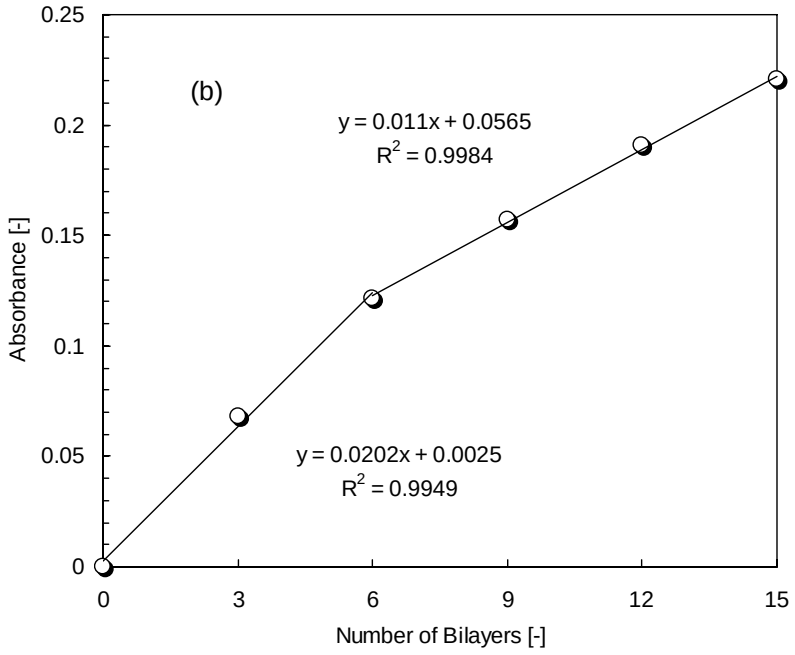

Figure 6.8 (*Continued*).

It is interesting to find that both two LBL films have a two-step film growth mode with each step having good absorbance-number of bilayers lineality. This probably means the way the LBL films grow for the first 6 bilayers might be different from that of the rest of bilayers. During the LBL assembly, the very first layer was deposited from ND dispersion at pH 3.5 which is able to interact with piranha-solution-treated glass slide through hydrogen bonding. The second layer was deposited from ND dispersion at pH 4.0 or 7.5. After the deposition of the first bilayer, the following bilayers were deposited in a similar manner. However, as the LBL film grows, the NDs gradually form relatively larger aggregates due to intra-layer and/or inter-layer interactions among NDs through hydrogen bonding, π-π interaction, and van der Waals forces (Figure 6.4, difference in the sizes of aggregates for LBL films with 3 and 15 bilayers). In addition, the surface coverage of the film is also increased as ND LBL film grows. Accordingly, the ND LBL

film morphologies actually experience some subtle changes in LBL assembly: in the deposition of the first few bilayers, the ND LBL film is high in effective surface area (low surface coverage) that is available for the deposition of following NDs to continue LBL assembly due to small ND aggregate size; but as the film grows in LBL assembly process, the NDs deposited tend to grow larger in size by growing aggregates and meanwhile surface coverage is increased so that the effective film surface area left for the following ND deposition is decreased. Consequently, the number of NDs that could be deposited at each time of deposition is correspondingly reduced as the number of bilayers increases. Finally, as the number of bilayers continues increasing to an upper limit (corresponding to a high surface coverage of film), the number of NDs that could be deposited at each time of deposition could no longer be kept up at a high level and as a result the LBL film growth rate is reduced to a lower level (second step as opposed to the first step where film grows at a faster rate due to relatively larger effective surface area available for the following ND deposition). This is different from existing LBL assembly based on polyelectrolytes or nano/polyelectrolyte systems which features linear or exponential film growth [241, 242]. In case of LBL assembly involving polyelectrolytes, the polyions are able to adsorb on a larger number of surface sites to yield conformal coatings more readily than nanoscale objects [240]; while for the assembly of nanoscale objects such as NDs in the present work, it takes multiple cycles in the first step of film growth to reach a high (or complete) surface coverage for the film growth of the second step. Therefore, the present work shows two distinct film growth steps, which is different from linear film growth commonly seen in polyelectrolyte LBL assembly.

The film growth rate observed in the present work suggests that ND LBL film might be able to retain good nanostructures until 6 bilayers. For films with more than 6 bilayers, the large ND aggregate size might be retarding the film growth, which is consistent with the work by Fermin *et al.* dealing with LBL assembly of diamond particle/polyelectrolyte [142]. In Fermin *et al.*'s work [142], the LBL films began to slow down growth rate or lose already deposited diamond particles after 4 bilayers' deposition of diamond particle/polyelectrolyte. Some previous research also reported on a similar two-step film growth during LBL assembly of polyelectrolytes or carbon nanotube/gold nanoparticle [141, 240, 242]. However, in these work dealing with polyelectrolytes or carbon nanotube/gold nanoparticle LBL films, the second step showed higher film growth rates, which might be attributable to the increased film thickness after full surface coverage is reached [240]. On the contrary, the present work shows that for the assembly of NDs, the higher film surface coverage would give rise to a lower film growth rate, which might result from the growth of ND aggregates during LBL assembly as detailed previously. Actually the proposed two-step film growth mode could be further evidenced from Figure 6.7 (b). The ND (3.5/7.5) films with 3 and 6 bilayers have absorption bands located at *ca.* 295 nm while those with 9~15 bilayers reside at *ca.* 300 nm, indicating an evident increase in the size of ND aggregates after 6 bilayers of deposition. In Hammond *et al.*'s work [240], they also found noticeable aggregation in LBL assembly after full surface coverage is reached, which agrees well with our findings.

It is also interesting to note that for the first step of deposition, ND (3.5/4.0) LBL films grow more quickly than ND (3.5/7.5) films, as indicated by the slope of their respective trend lines

(Figure 6.8). One major reason might be that in ND (3.5/4.0) LBL film deposition, ND surface negative charge is rather limited compared with that in ND (3.5/7.5) film deposition process. Because of limited surface negative charge, NDs in dispersion could have relatively easy access to the ND films through hydrogen boding while for ND (3.5/7.5) films both NDs in dispersion and on the films are relatively more negatively charged so NDs in the dispersion could not have easy access to the ND films. However, in the second step of deposition, two LBL films nearly exhibit the same growth rate, which could be attributable to the following: during ND (3.5/4.0) preparation process its film growth rate is higher than ND (3.5/7.5) due to less surface negative charge of ND. Accordingly, its effective surface area for deposition is decreased more quickly than that of ND (3.5/7.5). Therefore, in the second step of deposition, the growth rate of ND (3.5/7.5) might be able to "catch up" with that of ND (3.5/4.0).

Through the above discussion, it can be clearly seen that ND thin film could be prepared in an LBL fashion, which could have a flexible control over film morphology. Moreover, the further functionalization of LBL films prepared is also flexible because of the presence of oxygen-containing surface groups. The LBL assembly process for ND thin film preparation could be a promising substitute for traditional CVD technique for biomacromolecule immobilization because of high curvature of nanostructures on the film as well as ease and low cost in film preparation.

6.4 Summary

In this chapter, the ND thin films have been prepared by LBL assembly of NDs on glass slides

mainly by hydrogen bonding. For the LBL assembly of ND thin films, the film growth mechanism was studied and discussed in detail. The observed two-step growth mode of ND films was attributable to the increase of ND aggregate size and film surface coverage as the film thickness gains. The LBL films feature regularly-organized nanostructures, which could be tuned by adjusting the number of bilayers deposited as demonstrated in the present work. Moreover, the oxygen-containing surface groups on LBL films make possible the further functionalization by chemical or physical approach.

CHAPTER 7

ADSORPTION OF AZO DYE ONTO NANODIAMOND SURFACE

This chapter has been submitted as:

Wang H.D.; Yang Q.; Niu C.H.; Badea I. Adsorption of Azo Dye onto Nanodiamond Surface. 2011.

Contribution of the Ph.D. Candidate

Under the guidance of Prof. Yang and Prof. Niu, Hai-Dong Wang designed and conducted the experiment for this chapter as well as prepared manuscript for publication. Prof. Badea has also provided guidance in both experiment and manuscript revision.

7.1 Introduction

Through the discussion of the above chapters, it could be clearly seen that large specific surface area, oxygen-containing surface groups as well as chemical and physical inertness endow ND with excellent surface properties promising for many applications such as biomacromolecule immobilization. In this chapter, the application of surface properties of ND is further extended to azo dye contaminant adsorption.

The main objective of this chapter is to investigate the mechanism accounting for the adsorption of dye molecule onto ND surface. To this end, acid orange 7 (AO7) was chosen as a model textile azo dye (azo dyes have been extensively used worldwide in textile industry) to

study its adsorption behaviors and mechanism on ND surface. As control groups, another azo compound sulfasalazine (SSZ), together with 5-aminosalicylic acid (5-ASA) and sulfapyridine (SPY), were studied for their adsorption behaviors on ND surface, respectively. SSZ is a widely used azo antibiotic and it has been detected in various bodies of water throughout the world [243, 244] so the study of SSZ adsorption behavior on ND also facilitates this antibiotic removal from aquatic environment. More importantly, the study on the adsorption of SSZ, 5-ASA and SPY on ND might help ascertain whether or to what extent the azo bond contributes to the azo dye adsorption process since 5-ASA and SPY could be obtained through the cleavage of azo bond in SSZ molecule using colonic bacteria (Azoreductases) [245]. Detailed discussion is then given on specific adsorption behavior and mechanism for azo dye adsorption onto ND surface.

7.2 Materials and Methods

7.2.1 Materials

Detonation nanodiamond particles (NDs), which have an average crystal size of 3-5 nm, were purchased from Nanostructured & Amorphous Materials Inc. and used without further treatment. AO7 (dye content > 85%) and 5-ASA (purity > 99%) were purchased from Sigma-Aldrich. SSZ (purity > 98%) and SPY (purity > 99%) were from Fluka. All other reagents are of analytical grade and used without further purification. The water used in the present research is from a Milli-Q system.

7.2.2 Adsorption Isotherms

ND was dispersed at a concentration of 1.0 mg/ml, with ultrasonic treatment (Branson 2510 Sonication Bath), in adsorbate solutions buffered by phosphate buffer (0.1 M) or 0.1 M HCl. The phosphate buffer was used for the pH range of *ca.* 3 to 11 while 0.1 M HCl for *ca.* pH 1.0. The ND-adsorbate suspension was then mixed thoroughly on a Multitron Incubator Shaker in the dark at 25 ^{o}C and 180 rpm for 4 h (AO7 and SSZ) or 12 h (5-ASA and SPY) which was confirmed to be adequate to establish adsorption equilibrium for each adsorbate under the conditions of present research. Finally the suspension was subjected to centrifugation on a Beckman Coulter Allegra X-22R centrifuge (15,000 rpm, 30 min) and the adsorbate concentration in the supernatant was analyzed on a UV/Vis spectrophotometer (Shimadzu UVmini-1240). The detecting wavelengths used are as the following: AO7 (485 nm), SSZ (360 nm), 5-ASA (296 nm for pHs 1.0, 3.0, 5.0; 330 nm for pHs 7.0 and 9.0; 320 nm for pH 11.0), and SPY (310 nm for pHs 1.0, 3.0, 5.0, and 7.0; 280 nm for pHs 9.0 and 11.0). All samples were run in duplicates with data presented as the average. Blank reference (ND dispersed in buffers) was used during adsorption experiment to confirm the influence of floating ND in supernatant was negligible. The uptake of adsorbate was determined by adsorbate concentration difference between the initial solution and final supernatant, as expressed in Equation (7.1):

$$q = \frac{(C_0 - C) \cdot V}{m} \tag{7.1}$$

Where q is adsorbate uptake (mmol/kg dry ND), C_0 and C are adsorbate concentrations in initial solution (mmol/ml) and final supernatant (mmol/ml), respectively. V is the solution volume (ml) and m the dry net weight of ND (kg).

7.2.3 Fourier Transform Infrared (FT-IR) Studies

FT-IR spectra of ND-AO7 and ND-SSZ complexes were recorded on a JASCO FT/IR-4100 spectrometer. The complex was obtained by dispersing ND in AO7 or SSZ solution (*ca.* 7.5 mmol in pH 7.0 phosphate buffer, 0.1 M) at a concentration of 1 mg/ml and then separating the solid from the solution by centrifugation. The unbound adsorbate was removed by repeatedly rinsing the complex with Milli-Q water. The ND-AO7 or ND-SSZ complex was then lyophilized to dryness in the dark. For FT-IR sample preparation, 1 mg of ND-AO7 or ND-SSZ complex was ground with 100 mg of dried KBr to form homogeneous powder. The powder (*ca.* 25 mg) was made into pellet which was subjected to FT-IR measurement for transmittance spectrum. For each measurement, a total of 64 scans were averaged with a resolution of 4 cm^{-1}. For free AO7 and SSZ FT-IR spectra, the sample powders were used directly for measurements, using the identical manner as described above.

7.2.4 Zeta-potential Measurements

Zeta-potential measurements were performed on a Zetasizer Nano ZS instrument (Malvern) over a pH range from approximately 9.0 to 2.0 at 25 ^{o}C. Zeta-potential was determined by measuring the electrophoretic velocity of the nanoparticles by Laser Doppler Velocimetry technique. The pH of the solution was adjusted by an autotitrator using NaOH and HCl solutions. After reaching the desired pH by titration, the solution was left to equilibrate for 1 min before taking measurement. Each measurement was performed in triplicate with the data presented as an average. For sample preparation, the ND concentration was fixed at 0.005 mg/ml while both AO7

and SSZ had a concentration of 30 μM. The ND/AO7 and ND/SSZ dispersions were then stirred at room temperature in the dark for at least 4 h before the measurements.

7.3 Results and Discussion

7.3.1 FT-IR Characterizations

The molecular structures of adsorbates used in this work are schematically illustrated in Figure 7.1.

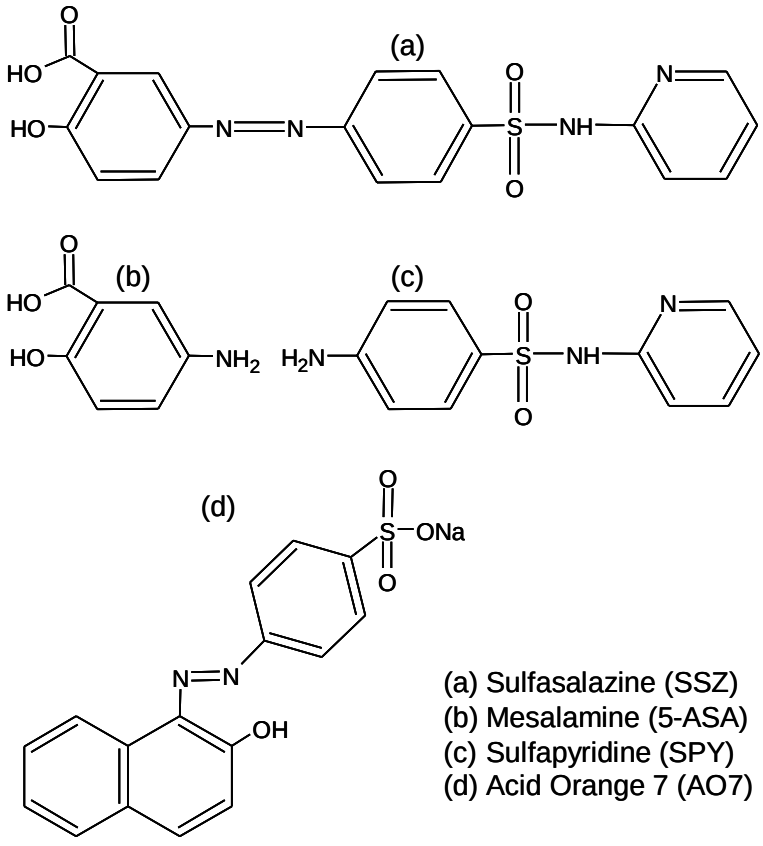

Figure 7.1 Molecular structure of adsorbates.

To illustrate the interaction of ND with AO7 and SSZ, the FT-IR analysis was performed on AO7/ND-AO7 and SSZ/ND-SSZ. These measurements could also facilitate the analysis of

adsorption behaviors of the AO7 and SSZ (as well as the 5-ASA and SPY) in adsorption isotherm studies. In the FT-IR measurements, the ND-AO7 and ND-SSZ complexes were first rinsed with Milli-Q water to remove any loosely-bound/unbound AO7 or SSZ on ND surface so that the AO7 or SSZ left in the complex is bound onto ND surface through strong specific interactions. In order to accurately reflect the changes in IR bands of AO7 and SSZ after forming complex with ND, no ND FT-IR background was deducted from the spectra since any error in the determination of AO7/ND or SSZ/ND ratio might give rise to inaccuracy in background deduction. Fortunately, the characteristic bands of AO7 and SSZ do not interfere with those of ND in the IR spectra of complexes, giving a clear illustration of how AO7 and SSZ interact with ND surface.

The FT-IR spectrum of AO7 (Figure 7.2 a) features azo bands at 1509 and 1563 cm^{-1} which can be assigned to vibration mode δ(N–H) of the H form of the azo bond (N=N) and a combination of vibrations involving N–H bending and –N=C stretching [246, 247]. The sulfonate group (SO_3^-) has intense bands at 1042 and 1126 cm^{-1} due to coupling between benzene and $\nu_s(SO_3^-)$ while the 1192 and 1212 cm^{-1} bands can be assigned to $\nu_{as}(SO_3^-)$ [246]. After being adsorbed onto ND surface, both azo and sulfonate IR bands have undergone noticeable changes. For azo bond, the 1509 and 1563 cm^{-1} bands in AO7 down-shift to 1503 and 1552 cm^{-1} in ND-AO7 complex. For sulfonate, 1042 and 1126 cm^{-1} bands also have a shift to lower wavenumbers (1038 and 1117 cm^{-1}, respectively) upon forming ND-AO7 complex while the 1192 and 1212 cm^{-1} bands in AO7 remains unchanged in wavenumbers for ND-AO7 complex. All these down-shifts of wavenumbers in IR bands clearly indicate that azo and sulfonate might account for the interaction between ND and AO7. The participation of sulfonate in the adsorption

of AO7 onto titanium dioxide surface has been evidenced by previous work [246, 247], wherein the two oxygen atoms of AO7 form bidentate surface complex with titanium dioxide. In our previous work, it was found that ND surface is rich in oxygen containing groups (carboxyl and hydroxyl) [18]. Therefore, it might be possible that the sulfonate could form hydrogen bonding with oxygen containing groups on ND surface which could partly account for ND-AO7 interaction.

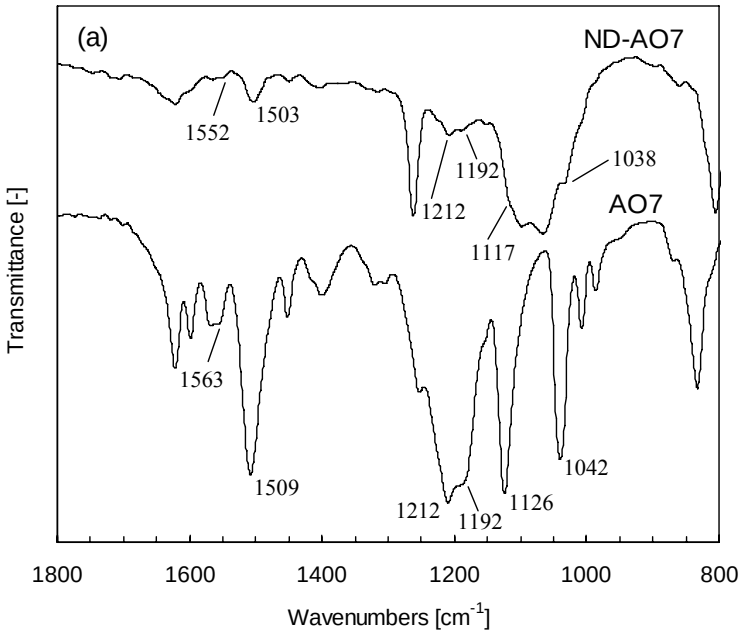

Figure 7.2 FT-IR spectra of (a) AO7 and ND-AO7; (b) SSZ and ND-SSZ.

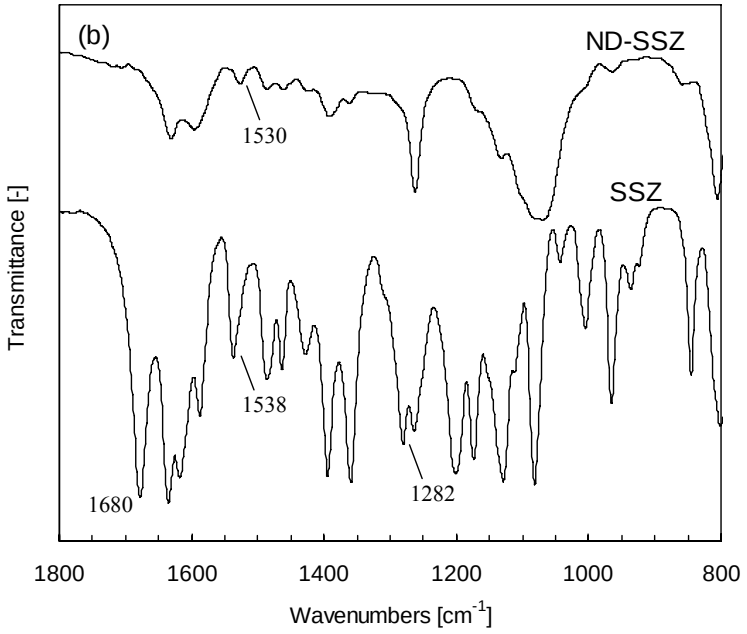

Figure 7.2 (*Continued*).

The FT-IR spectra of SSZ and ND-SSZ are presented in Figure 7.2 (b). SSZ also has strong azo band which is situated at 1538 cm^{-1} and can be assigned to vibration mode δ(N–H) of the H form of the azo bond. After being adsorbed onto ND surface, the band has an obvious downshift to 1530 cm^{-1}. The ν(C-O) in SSZ (1282 cm^{-1}) nearly disappears in ND-SSZ complex, suggesting that phenolic group might be also involved in the ND-SSZ interaction by forming hydrogen bonding with ND surface oxygen containing groups. Another notable change in SSZ IR spectra is the carbonyl group, which is located at 1680 cm^{-1} for pure SSZ but nearly disappears in ND-SSZ complex. The disappearance of carbonyl bands indicates its participation in the SSZ adsorption onto ND surface, which might occur through forming hydrogen bonding with ND surface hydroxyl and/or carboxyl groups.

Clearly, the FT-IR spectra for both AO7/ND-AO7 and SSZ/ND-SSZ suggest that azo bond

might play an important role in the adsorption process. It has been well documented that the azo bond could act as strong π electron acceptor [248, 249]. On the other hand, it is known that the ND surface is covered by a thin layer of graphite [64] and the graphite has been reported to have π-donor capability [250, 251]. Therefore it is likely that the π-donor-acceptor interaction is built up between electron-rich surface graphite of ND and azo bonds of AO7 and SSZ during the adsorption process.

7.3.2 Adsorption Isotherms

The adsorption isotherm quantitatively investigates the adsorption behaviors of AO7 and SSZ onto ND surface. From the above discussion on the FT-IR spectra of complexes formed between ND and AO7/SSZ, it was concluded that the azo bond might participate in the strong π-donor-acceptor interaction with the graphite layer on the ND surface. To have a clear understanding of whether the above mentioned π-donor-acceptor interaction does exist and how strong this interaction is, 5-ASA and SPY were also studied for adsorption behaviors in addition to AO7 and SSZ. In fact, SSZ could be cleaved from azo bond using colonic bacteria (Azoreductases) into two compounds: 5-ASA and SPY (Figures 7.1 a, b and c) [245]. The p*K*a values of all four adsorbates are listed in Table 7.1.

Table 7.1 The pKa values of AO7, SSZ, 5-ASA, and SPY.

Compounds	pK_a	References
AO7	pK_{a1} 1.0 (Sulfonate) pK_{a2} 11.4 (Naphthalene OH)	[252]
SSZ	pK_{a1} 2.9 (Carboxyl) pK_{a2} 7.0 (Sulfonamide) pK_{a3} 12.5 (Phenol)	[253]
5-ASA	pK_{a1} 2.3 (Carboxyl) pK_{a2} 5.7 (Amino) pK_{a3} 12.0 (Phenol)	[254, 255]
SPY	pK_{a1} 2.3 (Anilinium) pK_{a2} 8.4 (Sulfonamide)	[256]

The ND used in the present research has a surface area of *ca.* 300 m^2/g and average crystal size of 3-5 nm (data provided by Nanostructured & Amorphous Materials Inc.), which is desirable for adsorption applications. The ND surface is rich in oxygen containing groups (carboxyl and hydroxyl) according to FT-IR spectra in our previous studies [18]. In addition, its surface possesses a graphite layer as evidenced in our previous study [225] as well as other research [64]. Therefore the ND used in this work features large surface area, surface graphite layer as well as surface oxygen containing groups.

The adsorption isotherms of all adsorbates are given in Figure 7.3.

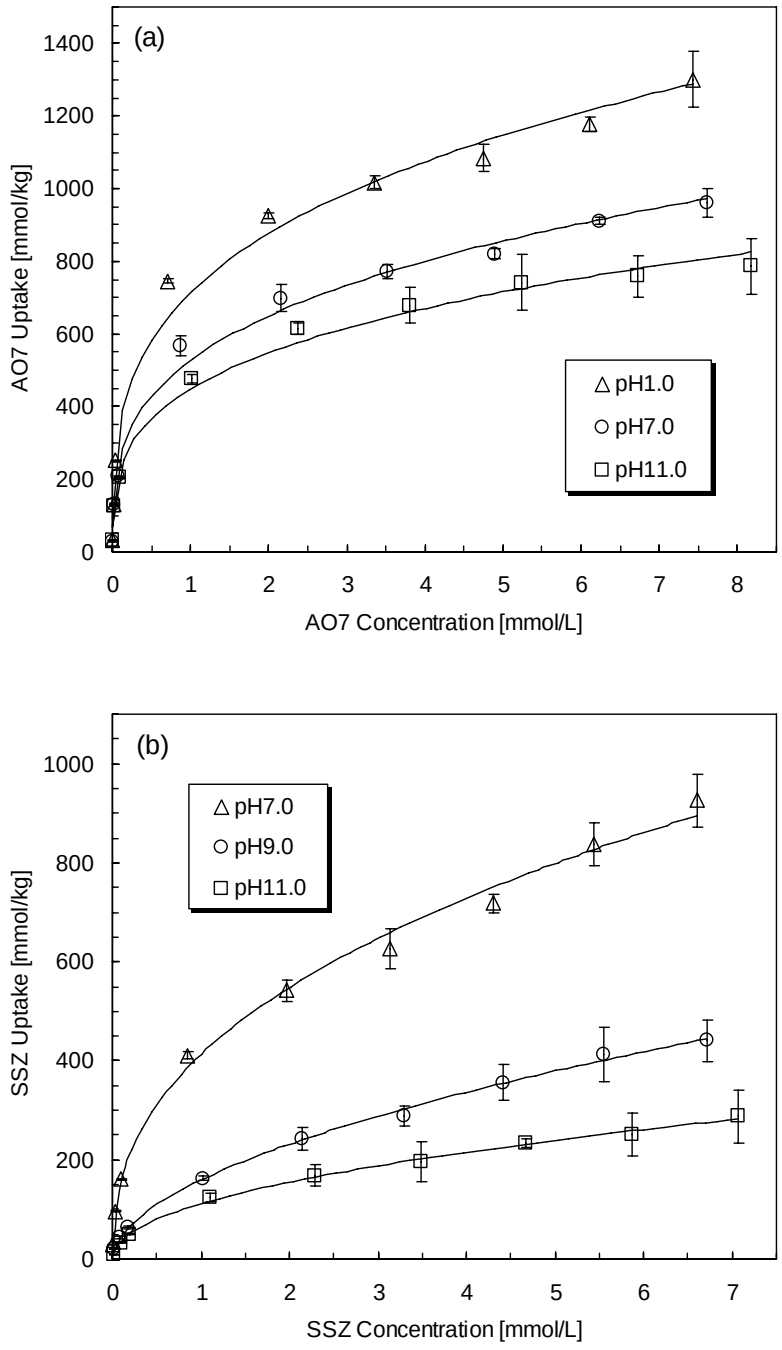

Figure 7.3 Adsorption isotherms of (a) AO7, (b) SSZ, (c) 5-ASA, and (d) SPY. The 5-ASA and SPY isotherms were obtained at pH 7.0. The error bar represents standard deviation.

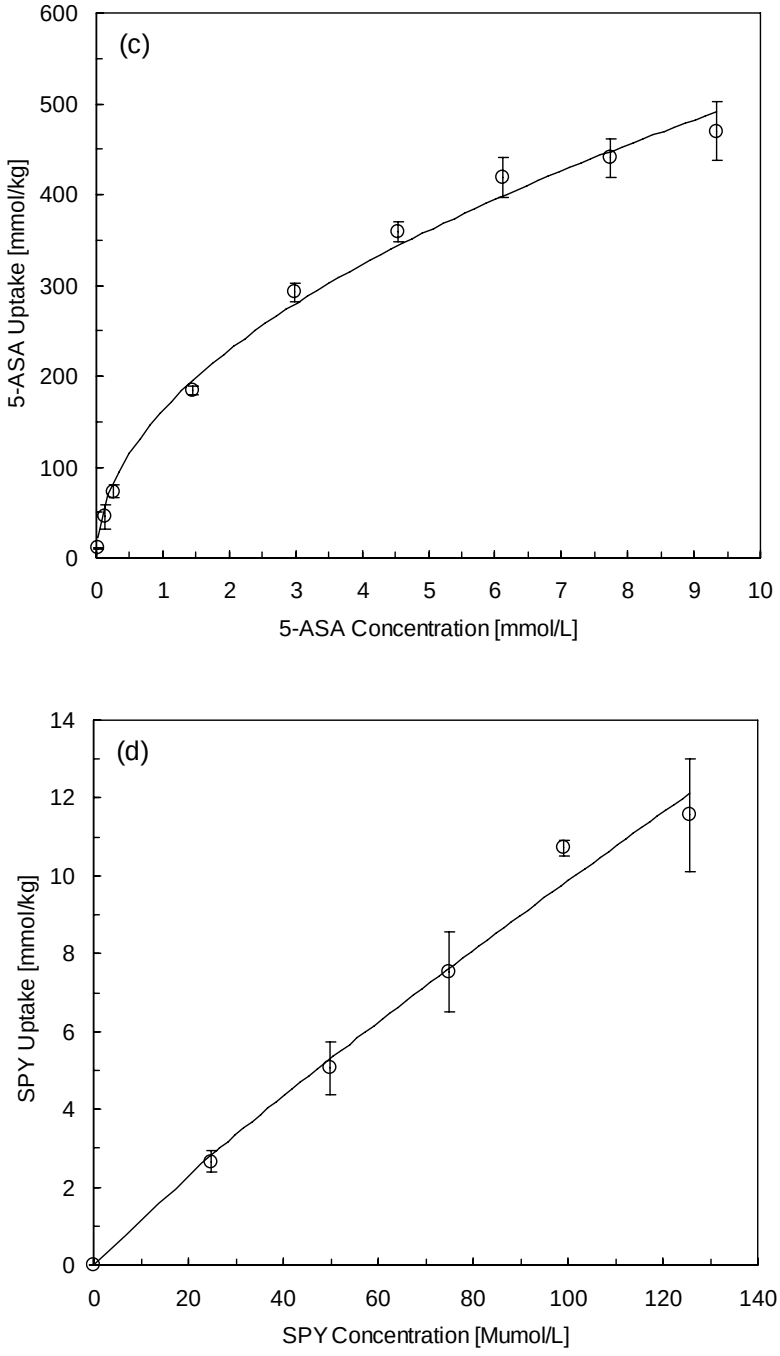

Figure 7.3 (*Continued*).

All isotherms could be well fit by Freundlich adsorption model with R^2 higher than 0.97:

$$q_e = K_f \cdot C_e^{(1/n)} \tag{7.2}$$

Where q_e and C_e are equilibrium adsorbate concentration on the ND surface (mmol/kg) and in

the solution (mmol/L), respectively. K_f is the Freundlich constant and $1/n$ the measure of nonlinearity [256, 257]. K_f and $1/n$ are determined by nonlinear regression of Equation (7.2).

To compare the adsorption coefficients K_d (L/kg) among all four adsorbates with pH changes, the exponent $1/n$ is set to one and the adsorption coefficient is determined as:

$$K_d = \frac{q_e}{C_e} \tag{7.3}$$

For the determination of adsorption coefficient K_d, the initial concentration for all adsorbates are kept at 30 μM with ND concentration fixed at 1 mg/ml. Then K_d could be determined through Equation (7.3).

Since the solubility of SSZ becomes extremely low as pH drops below *ca.* 5.0 (saturated SSZ aqueous solution nearly has no detectable UV absorbance as pH drops below *ca.* 5.0), the present work only studied its adsorption behavior at and above pH 5.0. AO7, used in the form of sulfonate salt which renders the whole molecule more hydrophilic than SSZ, is quite soluble in water throughout the entire pH range under investigation (pH values of 1 to 11). Due to the very low solubility of SPY in water, only a narrow concentration range was investigated for adsorption isotherm.

As shown in Figure 7.3, most adsorption isotherms for AO7 and SSZ (especially those at low pH values) show a steep slope at low concentration ranges, suggesting a strong interaction between ND and AO7/SSZ. The maximum uptakes for AO7 and SSZ, in the experimental conditions of the present work, are 1288 mmol/kg and 925 mmol/kg, respectively. Considering that the ND in this work has not reached its maximum capacity for AO7 and SSZ adsorptions

(see Figures 7.3 a and b), the actual maximum uptakes should be even higher if ND surface is totally saturated with AO7 of higher initial concentration. In Liu *et al.* and Li *et al.*'s work [157, 159], where granular activated carbons (AC) were used for AO7 adsorption, both of their maximum uptakes for AO7 were well below 280 mmol/kg. In Gercel *et al.*'s work [158], the maximum AO7 uptake on activated carbon was close to 1100 mmol/kg. In these work [157-159], the specific surface areas for ACs were *ca.* 605-982 m^2/g [159], *ca.* 459-864 m^2/g [157], and *ca.* 1048 m^2/g [158] while the ND in this work only has a specific surface area of *ca.* 300 m^2/g, suggesting that ND is a more effective adsorbent over AC in dye adsorption due to its easily-accessed exterior surface. For using CNT in AO7 adsorption, Rodriguez *et al.* [258] have reported the maximum AO7 uptakes on CNT at pHs 3.0, 5.0, 7.0, and 9.0 were all below 280 mmol/kg, which is significantly lower than the findings in this work. The above comparisons positively indicate that ND has higher capacity for azo dye adsorption than AC and CNT.

Compared with titanium dioxide nano particle which is often used for dye adsorption [247], ND shows considerably higher AO7 uptake (titanium dioxide only has maximum AO7 uptakes of *ca.* 200 and 50 mmol/kg at pHs 2.0 and 5.7, respectively [247]). The AO7 uptake on ND is also comparable with those on hematite and goethite [252] (*ca.* 800 mmol/kg and 100 mmol/kg respectively at equilibrium dye concentration of 3.5 mM at pH 3.5). ND in this work has AO7 uptakes of *ca.* 1100 mmol/kg (at pH 1.0) and *ca.* 780 mmol/kg (at pH 7.0) with the same equilibrium dye concentration (3.5 mM). It is noteworthy that titanium dioxide, hematite, and goethite have the maximum AO7 uptake at very acidic operating conditions and nearly no uptake at pH values close to and higher than 7.0. However, the textile wastewater is generally at a pH of

ca. 8.0 [160], thus to increase the efficiency of the dye removal the pH of the wastewater needs to be adjusted from alkaline to acid, giving rise to additional processing cost. Moreover, the acidification process would definitely increase the salinity which is another serious environmental issue. In stark contrast, in the present work, ND has high affinity with AO7 from acid to mild alkaline conditions, suggesting that ND could be used directly for textile wastewater treatment without adding additional cost and posing additional environmental issues. Other adsorbents used for dye-removal such as spent brewery grain [259] only has an AO7 uptake of *ca.* 28 mmol/kg with initial AO7 concentration of 0.1 g/L while ND in the present work has an AO7 uptake of over 200 mmol/kg at acid (pH 1.0), neutral (pH 7.0), and alkaline (pH 11.0) conditions with the same initial dye concentration.

As a control group, ND also shows high affinity and uptake with azo compound SSZ which might be mainly due to strong π-donor-acceptor interaction between ND surface graphite layer and azo bond of SSZ. The adsorption data (Figure 7.3 b) suggest that ND could also be a potential desirable adsorbent for removing the antibiotic SSZ from the aquatic environment.

In comparison with AO7 and SSZ, ND interacts with 5-ASA at a relatively lower level which is evidenced by lower uptake as well as mild slope at low concentration range (Figure 7.3 c). For SPY, its affinity with ND is considerably lower compared with the other three adsorbates. The relatively lower interactions between ND and 5-ASA/SPY, as compared with those between ND and AO7/SSZ, demonstrate the significance of the proposed π-donor-acceptor interaction in the adsorption of azo dye AO7 and azo antibiotic SSZ onto ND surface.

The Freundlich constants K_f as well as the measure of nonlinearity $1/n$ for each adsorption

isotherm in Figure 7.3 are listed in Table 7.2.

Table 7.2 Freundlich constant K_f and Freundlich exponent $1/n$.

Adsorbate	pH [-]	K_f [$mmol^{1-1/n}L^{1/n}kg^{-1}$]	$1/n$ [-]
AO7	1.0	714.44± 28.99	0.29 ± 0.02
	7.0	526.72 ± 18.00	0.30 ± 0.02
	11.0	448.16 ± 15.02	0.29 ± 0.02
SSZ	7.0	412.20 ± 12.81	0.41 ± 0.02
	9.0	159.68 ± 4.57	0.54 ± 0.02
	11.0	111.41 ± 3.21	0.48 ± 0.02
5-ASA	7.0	162.37 ± 8.75	0.50 ± 0.03
SPY	7.0	0.16 ± 0.07	0.90 ± 0.10

At pH 7.0, both AO7 and SSZ show much higher K_f than those of 5-ASA and SPY. The Freundlich exponent $1/n$ of AO7 and SSZ varies in the range of *ca.* 0.3 to 0.5, suggesting very strong nonlinearity in adsorption isotherms. Similarly, the 5-ASA adsorption isotherm at pH 7.0 also shows a relatively strong nonlinearity ($1/n$: *ca.* 0.5). On the contrary, the adsorption isotherm of SPY is nearly linear ($1/n$: *ca.* 0.9), implying that the affinity between ND and SPY is rather weak. The strong ND-AO7 and ND-SSZ interactions are consistent with the FT-IR measurements (Figures 7.2 a and b) which suggest a remarkable π-donor-acceptor interaction in

ND-AO7 and ND-SSZ complexes. According to FT-IR spectrum of SSZ (Figure 7.2 b), the carbonyl and phenolic groups have strong interaction with ND surface which might be able to account for the fact that 5-ASA also has a relatively high affinity with ND, though not as strong as those of AO7 and SSZ.

Taking the pH effect into consideration, the adsorption coefficients (K_d) of the four adsorbates were also calculated (Figure 7.4). Both AO7 and SSZ have high adsorption coefficients, considerably higher than those of 5-ASA and SPY. For AO7, the K_d only decreases slightly as pH increases from 1.0 to 11.0 while SSZ has a more pH-sensitive adsorption coefficient which is lowered by 2 orders of magnitude as pH shifts from 5.0 to 11.0. The high adsorption coefficient of ND toward SSZ is comparable with Zhu *et al.*'s work on the affinity between carbon nanotube/graphite and sulfonamide antibiotics [256]. However, K_d of SPY in this work is around two orders of magnitude lower than that in Zhu's work [256], suggesting that the π-π electron coupling and/or stacking between aromatic compounds and graphene surface of the carbon nanotube as proposed by some previous researchers [260] might not apply to the surface graphite of ND in this work. This suggests that the high K_d of SSZ might be largely attributable to the strong π-donor-acceptor interaction between the azo bond of SSZ and surface graphite of ND (together with the participation of carbonyl and phenolic groups in adsorption) as proposed from the FT-IR measurements. Both sulfonate on AO7 and sulfonamide on SSZ are known to be electron-attracting groups [256, 261]. As a result, the electron density of azo bonds on both AO7 and SSZ tends to decrease, which enhances the π-electron acceptor capability of the azo bond, thus the π-donor-acceptor interaction between AO7/SSZ and ND might be further strengthened.

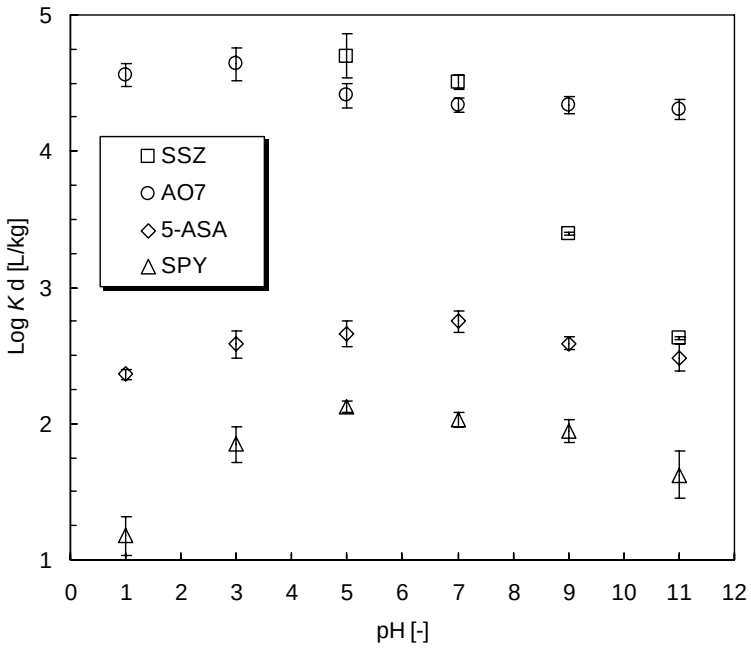

Figure 7.4 Adsorption coefficients with pH variations. The initial adsorbate concentration is fixed at 30 μM for all pH values. The error bar represents standard deviation.

SPY does not have strong specific interaction with ND, which might be adsorbed onto ND surface through weak hydrophobic interaction. In this work, it was found that SPY only has appreciable solubility in acid or alkaline environment (solubility at neutral and weak acid pH values is rather low: below 150 μmol/L). As pH is increased from 1.0, SPY is gradually deprotonated (pK_{a1} 2.3 for anilinium) with less positive charge becoming more hydrophobic, so K_d is kept at relatively higher level considering that SPY might interact with ND surface through weak hydrophobic interaction. However, as pH shifts higher than 7.0 where a substantial amount of sulfonamide is deprotonated (pK_{a2} 8.4 for sulfonamide), a more hydrophilic SPY renders K_d drop back to a lower level.

The decrease of K_d for AO7 and SSZ as pH is increased might also be explained in the

similar manner. AO7 has p*K*a values of 1.0 (sulfonate) and 11.4 (naphthalene OH) while SSZ has similar p*K*a values (2.9 for carboxyl, 7.0 for sulfonamide, and 12.5 for phenol). Thus, in highly acidic conditions both AO7 and SSZ exist largely in the neutral form of molecules and is less hydrophilic. As the pH increases, sulfonate (p*K*a 1.0) in AO7 and carboxyl (p*K*a 2.9) in SSZ begin to be deprotonated so that hydrophilicity increases correspondingly. In this work, it was found that at pH lower than 5.0 SSZ solubility in water is rather limited and then is considerably enhanced in near neutral to alkaline region, which might be corresponding to the deprotonation of sulfonamide (p*K*a: 7.0). This is a good reflection of considerable increase in hydrophilicity of the SSZ as pH increases. Moreover, with pH increase the deprotonated sulfonate and sulfonamide gradually become less electron-attracting and thus the π-electron acceptor capability of azo bond suffers correspondingly. The joint effect of increased hydrophilicity and deprotonation of sulfonate and sulfonamide tends to counteract the strong π-donor-acceptor interaction between AO7/SSZ and ND by redistributing more AO7 and SSZ into solution instead of onto ND surface. Therefore, the increased pH finally gives rise to a decrease of K_d. As pH is approaching neutral, sulfonamide of SSZ (p*K*a 7.0) is subjected to major deprotonation which brings about a substantial increase in hydrophilicity, resulting in major decrease of K_d. Compared with SSZ, the more hydrophilic AO7 does not change hydrophilicity drastically as pH increases therefore its K_d only experiences a slight decrease. In addition, the increased surface negative charge of AO7 and SSZ as pH increases might be partly contributing to the decrease of K_d because the ND surface is also more negatively charged at high pH values (Figure 7.6).

The 5-ASA has lowest solubility from *ca.* pH 2 to 6 which might be due to its isoelectric point

(p*I*) of *ca.* 4.0 [254, 262, 263]. Below p*I* the positively charged 5-ASA shows a decreased K_d which might be attributable to the increased solubility of 5-ASA (increase of hydrophilicity) with pH decrease. The low K_d of 5-ASA at high pH (pH values of 9 and 11) might be due to the increase in solubility and hydrophilicity of 5-ASA as well as charge repulsion from both negatively charged 5-ASA and ND.

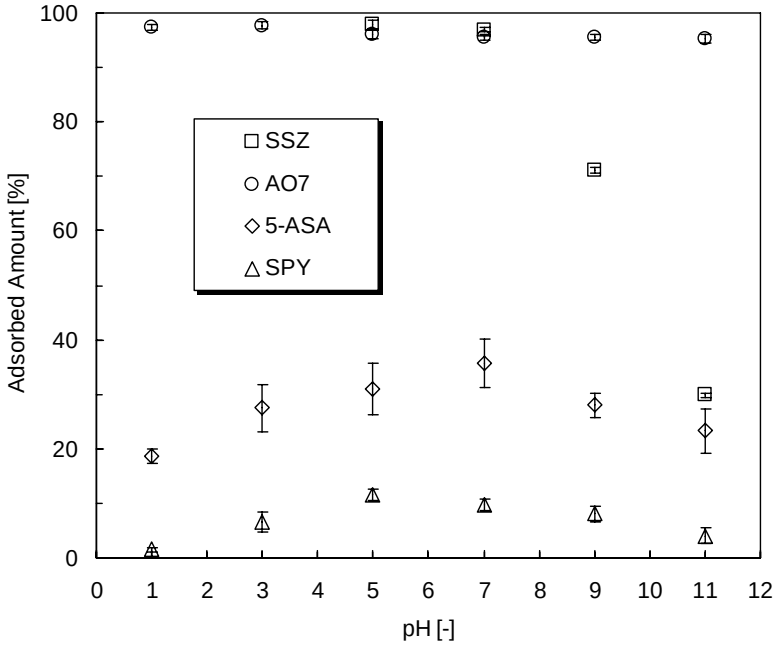

Figure 7.5 Percentage of adsorbate adsorbed onto ND surface at equilibrium. The initial adsorbate concentration is fixed at 30 μM for all pH values. The error bar represents standard deviation.

Converting K_d to the percentage of adsorbates adsorbed, Figure 7.4 is transformed into Figure 7.5 to show how much adsorbate could be removed at different pH conditions with initial adsorbate concentration fixed at 30 μM. As high as *ca.* 98% of AO7 could be removed from solution phase from pH 1.0 to 11.0. For SSZ this value is also as high as *ca.* 98% in near neutral

to neutral pH ranges but drops to 30% in alkaline environment. The highest adsorbed amounts of 5-ASA and SPY are only 36% and 12%, respectively. Thereby, Figure 7.5 further demonstrates the efficiency of ND in azo dye and azo antibiotic adsorption.

7.3.3 Zeta-potential Measurements

The zeta-potentials of ND, ND-AO7, and ND-SSZ are given in Figure 7.6, which gives evidence of the presence of AO7 and SSZ on ND surface through adsorption. Due to the formation of complexes introducing more negative charge onto ND surface, the zeta potentials of both ND-AO7 and ND-SSZ are noticeably lower than that of ND. This down-shift is consistent with previous reports on particle-AO7 complex where AO7 was adsorbed onto hematite and titanium dioxide, respectively [247, 252]. However, for ND-SSZ there is an increase of zeta-potential as pH shifts lower than *ca.* pH 5.0. As mentioned above, SSZ has extremely low solubility at pH lower than 5.0. Therefore, in zeta-potential measurements it was found that a large amount of SSZ precipitates from the solution as pH drops below 5.0 which might reduce the SSZ density on ND surface and thus decrease the surface negative charge. As a result, reduced surface negative charge would give rise to a larger increase in zeta-potential compared with ND-AO7 complex as pH is decreased.

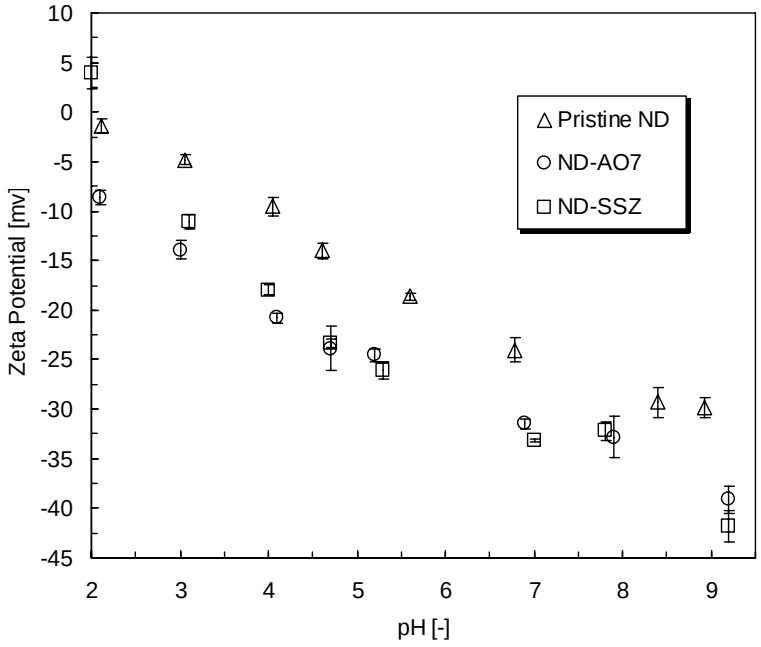

Figure 7.6 Zeta-potentials of ND, ND-AO7, and ND-SSZ with pH variations. The error bar represents standard deviation.

7.4 Summary

In this chapter, the adsorption of azo dye AO7 onto ND surface has been investigated in order to ascertain the adsorption behavior as well as the interaction involved in the adsorption process, where ND has been proved to have higher capacity in azo dye adsorption than widely used activated carbons and carbon nanotubes. As control groups, SSZ, together with 5-ASA and SPY (which could be cleaved from azo bond of SSZ), was also studied for the adsorption behavior. Due to strong π-donor-acceptor interaction between ND surface graphite layer and azo bond, ND shows considerably higher affinity with AO7 and SSZ than that with 5-ASA and SPY. Without azo bond participating in π-donor-acceptor interaction, ND only shows moderate and weak

interaction with 5-ASA and SPY, respectively. In addition, the interaction between ND and AO7/SSZ was found to be decreased as pH shifts from 1.0 to 11.0 which could be attributable to the increase in hydrophilicity and negative charges of AO7 and SSZ as the pH increases. Though affinity is slightly lower at high pH values, the adsorption coefficients of ND with AO7 at neutral to alkaline pHs are still of the same orders of magnitude with those of low pH values, suggesting that ND could be a desirable candidate for textile wastewater treatment which is normally at alkaline pH. The work in this chapter has demonstrated the great potential of using ND for textile wastewater treatment as well as azo antibiotic wastewater treatment.

CHAPTER 8
CONCLUSIONS AND FUTURE WORK

8.1 Conclusions

The major findings of the present thesis work are as the following:

(1) The ND used in the present work is already rich in oxygen-containing surface groups and therefore further oxidizing acid treatment is not necessary. Functionalization of ND with CMCS has been conducted by EDC chemistry and the final product NDCMCS has been characterized by a series of analyses including FT-IR spectroscopy, Raman spectroscopy, Zeta-potential measurement and X-ray diffraction. All the results obtained have clearly demonstrated that CMCS is successfully immobilized onto ND surfaces and the functionalization has been proved to be effective. The functionalization with CMCS improves the dispersity of ND especially in low and high pH aqueous solutions. Moreover, the rich content of primary amine and hydroxyl on CMCS backbone would make further physical or chemical functionalization of ND more flexible and versatile.

(2) The conformation of BSA in ND-BSA complex was investigated by a series of characterization techniques. The Fourier transform infrared spectroscopy shows an evident change in BSA secondary structure upon binding with ND. The UV-Vis and CD spectroscopies further indicate that most BSA structural features could be preserved in ND-BSA complex. The fluorescence spectroscopy reveals that Trp residues in BSA are placed in a more hydrophobic environment in ND-BSA complex suggesting major protein

unfolding is unlikely to occur. For the adsorption isotherms obtained at different pHs (3.5, 4.7, 6.0, 7.4, 9.0), both BSA uptake and the affinity between ND and BSA peak at pH 4.7 which suggests that hydrophobic force dominates the BSA adsorption process. The adsorption isotherms can be well fit by Freundlich but not Langmuir model. The zeta-potential measurements further suggest that after binding with BSA the strong binding force between ND and BSA might result in partial breakup of ND aggregates into relatively small ND-BSA aggregates. The results obtained have demonstrated that ND is able to preserve the albumin structural features to a large extent in ND-albumin complex and is very promising to be used for biosensor applications.

(3) The protein BSA has been chemically immobilized onto pristine ND surface, which was evidenced by FT-IR and UV-Vis spectroscopies. The LBL assembly properties of NDBSA with pristine ND were investigated on glass substrates. The NDBSA/ND coatings fabricated by LBL assembly method were stable and more densely-organized coating structures could be obtained by increasing the number of bilayers deposited. The present LBL assembly method for ND-protein coating fabrication could be easily employed to prepare biomacromolecule-functionalized ND films for biosensor applications. This work has demonstrated that the LBL assembly is a facile approach to fabricate ND coatings and it could be a desirable substitute for the traditional CVD process to prepare diamond coatings for biological applications.

(4) The ND thin films have been prepared by LBL assembly of NDs on glass slides mainly by hydrogen bonding. For the LBL assembly of ND thin films, the film growth mechanism

was studied and discussed in detail. The observed two-step growth mode of ND films was attributable to the increase of ND aggregate size and film surface coverage as the film thickness gains. The LBL films feature regularly-organized nanostructures, which could be tuned by adjusting the number of bilayers deposited as demonstrated in the present work. Moreover, the oxygen-containing surface groups on LBL films make possible the further functionalization by chemical or physical approach.

(5) The adsorption of azo dye AO7 onto ND surface has been investigated in order to ascertain the adsorption behavior as well as the interaction involved in the adsorption process, where ND has been proved to have higher capacity in azo dye adsorption than widely used activated carbons and carbon nanotubes. As control groups, SSZ, together with 5-ASA and SPY (which could be cleaved from azo bond of SSZ), was also studied for the adsorption behavior. Due to strong π-donor-acceptor interaction between the ND surface graphite layer and azo bond, ND shows considerably higher affinity with AO7 and SSZ than that with 5-ASA and SPY. Without azo bond participating in π-donor-acceptor interaction, ND only shows moderate and weak interaction with 5-ASA and SPY, respectively. In addition, the interaction between ND and AO7/SSZ was found to be decreased as pH shifts from 1.0 to 11.0 which could be attributable to the increase in hydrophilicity and negative charges of AO7 and SSZ as the pH increases. Though affinity is slightly lower at high pH values, the adsorption coefficients of ND with AO7 at neutral to alkaline pHs are still of the same orders of magnitude with those of low pH values, suggesting that ND could be a desirable candidate for textile wastewater treatment which

is normally at alkaline pH. The present work has demonstrated the great potential of using ND for textile wastewater treatment as well as azo antibiotic wastewater treatment.

8.2 Suggestions for Future Work

(1) In the present thesis work, it has been demonstrated that ND is an excellent platform for the immobilization of biomacromolecules such as protein and polysaccharide. The protein introduced onto ND surface could retain most of its structural features. Moreover, previous research has pointed out that ND has desirable biocompatibility with biomacromolecules. According to the above findings, it might be feasible to fabricate a biosensor system based on piezoelectric crystal. In a piezoelectric biosensor, the antibody is immobilized onto the sensor transducer surface (quartz crystal microbalance) to detect the analyte. This analytical method has been proved to have extremely high detection sensitivity [264]. For this type of biosensor, the high loading of biomolecules with reserved bioactivities is important for practical application [265]. Nano-structured surface on one hand could significantly increase the surface area and on the other hand could facilitate the retention of structural features of biomolecules. Therefore, to introduce ND onto piezoelectric crystal surface might be an effective way to enhance the loading of biomolecules and thus enhance the detection sensitivity. ND surface is negatively charged so it could be assembled onto positively charged amine-terminated piezoelectric crystal using similar approach as reported in previous study [266]. Then antibody could be immobilized onto ND surface for the detection of analyte (antigen) from the environment. The merits for the

use of ND in this biosensor system consist in that both high specific area (for high loading of antibody) and desirable biocompatibility of ND could be given full play.

(2) For the application of ND in azo dye contaminant adsorption, the present thesis work mainly focuses on the adsorption behaviors and mechanism of azo dye onto ND surface and has demonstrated that ND is an effective adsorbent for azo dye contaminant. Future work might need to further investigate the desorption of azo dye from ND surface, which is of great importance for practical use. The alkaline solution treatment, which is effective for desorption of azo dye from biomass [267], might not work on carbon materials [158]. The microwave irradiation has been proved to be effective in regeneration of dye exhausted activated carbon [159, 268] and it might be worth of trying this or similar approach for ND regeneration.

(3) For carbon nanomaterial application, their relatively high cost might be another concern. Though cheaper than CNT, it might still be necessary to seek more cost-effective way to apply ND to azo dye adsorption. A feasible approach might be doping ND into other adsorbent for dye removal, such as chitosan, to enhance the performance of this material. In this regard, a good case in point is that Lee *et al.* [269, 270] found that even chitosan hydrogel slightly doped with CNT (0.01wt%) has a significant increase in congo red uptake over undoped ones. Due to very small amount of doped CNT, the synthesis cost for the adsorbent actually doesnot change significantly. The present thesis work has demonstrated high affinity of ND with azo dye which is even higher than that of CNT. Moreover, the synthesis cost of ND is lower than that of CNT. Therefore it is reasonable to

believe that ND might be a promising candidate to be doped into other cost-effective adsorbents to enhance their performance in azo dye adsorption.

REFERENCES

[1] Shenderova, O. A.; Zhirnov, V. V.; Brenner, D. W. Carbon nanostructures. *Crit. Rev. Solid. State Mater. Sci.* **2002**, 27, 227-356.

[2] Liu, K. K.; Cheng, C. L.; Chang, C. C.; Chao, J. I. Biocompatible and detectable carboxylated nanodiamond on human cell. *Nanotechnology* **2007**, 18, 325102.

[3] Schrand, A. M.; Huang, H. J.; Carlson, C.; Schlager, J. J.; Osawa, E.; Hussain, S. M.; Dai, L. M. Are diamond nanoparticles cytotoxic? *J. Phys. Chem. B* **2007**, 111, 2-7.

[4] Jia, G.; Wang, H. F.; Yan, L.; Wang, X.; Pei, R. J.; Yan, T.; Zhao, Y. L.; Guo, X. B. Cytotoxicity of carbon nanomaterials: Single-wall nanotube, multi-wall nanotube, and fullerene. *Environ. Sci. Technol.* **2005**, 39, 1378-83.

[5] Cui, D. X.; Tian, F. R.; Ozkan, C. S.; Wang, M.; Gao, H. J. Effect of single wall carbon nanotubes on human HEK293 cells. *Toxicol. Lett.* **2005**, 155, 73-85.

[6] Smart, S. K.; Cassady, A. I.; Lu, G. Q.; Martin, D. J. The biocompatibility of carbon nanotubes. *Carbon* **2006**, 44, 1034-47.

[7] Warheit, D. B. What is currently known about the health risks related to carbon nanotube exposures? *Carbon* **2006**, 44, 1064-9.

[8] Huang, H.; Pierstorff, E.; Osawa, E.; Ho, D. Active nanodiamond hydrogels for chemotherapeutic delivery. *Nano Lett.* **2007**, 7, 3305-14.

[9] Manna, S. K.; Sarkar, S.; Barr, J.; Wise, K.; Barrera, E. V.; Jejelowo, O.; Rice-Ficht, A. C.; Ramesh, G. T. Single-walled carbon nanotube induces oxidative stress and activates

nuclear transcription factor-kappa B in human keratinocytes. *Nano Lett.* **2005**, 5, 1676-84.

[10] Krueger, A.; Stegk, J.; Liang, Y. J.; Lu, L.; Jarre, G. Biotinylated nanodiamond: Simple and efficient functionalization of detonation diamond. *Langmuir* **2008**, 24, 4200-4.

[11] Niemeyer, C. M. Nanoparticles, proteins, and nucleic acids: Biotechnology meets materials science. *Angew. Chem. Int. Ed.* **2001**, 40, 4128-58.

[12] Lee, Y. S.; Mrksich, M. Protein chips: from concept to practice. *Trends Biotechnol.* **2002**, 20, S14-S8.

[13] Zhu, H.; Snyder, M. Protein chip technology. *Curr. Opin. Chem. Biol.* **2003**, 7, 55-63.

[14] Drummond, T. G.; Hill, M. G.; Barton, J. K. Electrochemical DNA sensors. *Nat. Biotechnol.* **2003**, 21, 1192-9.

[15] Lundqvist, M.; Sethson, I.; Jonsson, B. H. Protein adsorption onto silica nanoparticles: Conformational changes depend on the particles' curvature and the protein stability. *Langmuir* **2004**, 20, 10639-47.

[16] Jiang, X.; Jiang, U. G.; Jin, Y. D.; Wang, E. K.; Dong, S. J. Effect of colloidal gold size on the conformational changes of adsorbed cytochrome c: Probing by circular dichroism, UV-visible, and infrared spectroscopy. *Biomacromolecules* **2005**, 6, 46-53.

[17] Huang, H. J.; Dai, L. M.; Wang, D. H.; Tan, L. S.; Osawa, E. Large-scale self-assembly of dispersed nanodiamonds. *J. Mater. Chem.* **2008**, 18, 1347-52.

[18] Wang, H. D.; Niu, C. H.; Yang, Q. Q.; Badea, I. Study on protein conformation and adsorption behaviors in nanodiamond particle-protein complexes. *Nanotechnology* **2011**, 22, 145703.

[19] Huang, H. J.; Pierstorff, E.; Osawa, E.; Ho, D. Protein-mediated assembly of nanodiamond hydrogels into a biocompatible and biofunctional multilayer nanofilm. *Acs Nano* **2008**, 2, 203-12.

[20] Steinmuller-Nethl, D.; Kloss, F. R.; Najam-U-Haq, M.; Rainer, M.; Larsson, K.; Linsmeier, C.; Koehler, G.; Fehrer, C.; Lepperdinger, G.; Liu, X.; Memmel, N.; Bertel, E.; Huck, C. W.; Gassner, R.; Bonn, G. Strong binding of bioactive BMP-2 to nanocrystalline diamond by physisorption. *Biomaterials* **2006**, 27, 4547-56.

[21] Bondar', V. S.; Pozdnyakova, I. O.; Puzyr', A. P. Applications of nanodiamonds for separation and purification of proteins. *Phys. Solid State* **2004**, 46, 758-60.

[22] Huang, L. C. L.; Chang, H. C. Adsorption and immobilization of cytochrome c on nanodiamonds. *Langmuir* **2004**, 20, 5879-84.

[23] Kong, X. L.; Huang, L. C. L.; Hsu, C. M.; Chen, W. H.; Han, C. C.; Chang, H. C. High-affinity capture of proteins by diamond nanoparticles for mass spectrometric analysis. *Anal. Chem.* **2005**, 77, 259-65.

[24] Chung, P. H.; Perevedentseva, E.; Tu, J. S.; Chang, C. C.; Cheng, C. L. Spectroscopic study of bio-functionalized nanodiamonds. *Diamond Relat. Mater.* **2006**, 15, 622-5.

[25] Nguyen, T. T. B.; Chang, H. C.; Wu, V. W. K. Adsorption and hydrolytic activity of lysozyme on diamond nanocrystallites. *Diamond Relat. Mater.* **2007**, 16, 872-6.

[26] Huang, T. S.; Tzeng, Y.; Liu, Y. K.; Chen, Y. K.; Walker, K. R.; Guntupalli, R.; Liu, C. Immobilization of antibodies and bacterial binding on nanodiamond and carbon nanotubes for biosensor applications. *Diamond Relat. Mater.* **2004**, 13, 1098-102.

[27] Kong, X. L.; Huang, L. C. L.; Liau, S. C. V.; Han, C. C.; Chang, H. C. Polylysine-coated diamond nanocrystals for MALDI-TOF mass analysis of DNA oligonucleotides. *Anal. Chem.* **2005**, 77, 4273-7.

[28] Pierson, H. O. Handbook of carbon, graphite, diamond and fullerenes: properties, processing and applications. *Noyes Publications* **1993**.

[29] O'Connell, M. J. Carbon nanotubes: properties and applications. *Taylor & Francis Group* **2006**.

[30] Krueger, A. New carbon materials: Biological applications of functionalized nanodiamond materials. *Chem. Eur. J.* **2008**, 14, 1382-90.

[31] Choy, K. L. Chemical vapour deposition of coatings. *Prog. Mater. Sci.* **2003**, 48, 57-170.

[32] Akaishi, M.; Kanda, H.; Yamaoka, S. Synthesis of Diamond from Graphite Carbonate Systems under Very High-Temperature and Pressure. *J. Cryst. Growth* **1990**, 104, 578-81.

[33] Sternschulte, H.; Thonke, K.; Sauer, R.; Koizumi, S. Optical evidence for 630-meV phosphorus donor in synthetic diamond. *Phys. Rev. B* **1999**, 59, 12924-7.

[34] Yarbrough, W. A.; Messier, R. Current Issues and Problems in the Chemical Vapor-Deposition of Diamond. *Science* **1990**, 247, 688-96.

[35] Sung, C. M.; Sung, M. Carbon nitride and other speculative superhard materials. *Mater. Chem. Phys.* **1996**, 43, 1-18.

[36] Hamers, R. J.; Stavis, C.; Clare, T. L.; Butler, J. E.; Radadia, A. D.; Carr, R.; Zeng, H. J.; King, W. P.; Carlisle, J. A.; Aksimentiev, A.; Bashir, R. Surface functionalization of thin-film diamond for highly stable and selective biological interfaces. *P. Natl. Acad. Sci.*

USA **2011**, 108, 983-8.

[37] Hartl, A.; Schmich, E.; Garrido, J. A.; Hernando, J.; Catharino, S. C. R.; Walter, S.; Feulner, P.; Kromka, A.; Steinmuller, D.; Stutzmann, M. Protein-modified nanocrystalline diamond thin films for biosensor applications. *Nat. Mater.* **2004**, 3, 736-42.

[38] Tang, L.; Tsai, C.; Gerberich, W. W.; Kruckeberg, L.; Kania, D. R. Biocompatibility of Chemical-Vapor-Deposited Diamond. *Biomaterials* **1995**, 16, 483-8.

[39] Baranauskas, V.; Fontana, M.; Guo, Z. J.; Ceragioli, H. J.; Peterlevitz, A. C. Analysis of the coagulation of human blood cells on diamond surfaces by atomic force microscopy. *Nanotechnology* **2004**, 15, 1661-4.

[40] Hirvonen, J. P.; Koskinen, J.; Jervis, J. R.; Nastasi, M. Present progress in the development of low friction coatings. *Surf. Coat. Technol.* **1996**, 80, 139-50.

[41] Lappalainen, R.; Anttila, A.; Heinonen, H. Diamond coated total hip replacements. *Clin. Orthop. Relat. R.* **1998**, 118-27.

[42] Hirose, Y.; Amanuma, S.; Komaki, K. The Synthesis of High-Quality Diamond in Combustion Flames. *J. Appl. Phys.* **1990**, 68, 6401-5.

[43] Hupert, M.; Muck, A.; Wang, R.; Stotter, J.; Cvackova, Z.; Haymond, S.; Show, Y.; Swain, G. M. Conductive diamond thin-films in electrochemistry. *Diamond Relat. Mater.* **2003**, 12, 1940-9.

[44] Trew, R. J.; Yan, J. B.; Mock, P. M. The potential of diamond and SiC electronic devices for microwave and millimeter-wave power applications. *P. Ieee* **1991**, 79, 598-620.

[45] Qureshi, A.; Gurbuz, Y.; Howell, M.; Kang, W. P.; Davidson, J. L. Nanocrystalline

diamond film for biosensor applications. *Diamond Relat. Mater.* **2010**, 19, 457-61.

[46] Su, L.; Qiu, X. P.; Guo, L. H.; Zhang, F. H.; Tung, C. H. Amperometric glucose sensor based on enzyme-modified boron-doped diamond electrode by cross-linking method. *Sensor Actuat. B* **2004**, 99, 499-504.

[47] Narayan, R. J.; Wei, W.; Jin, C.; Andara, M.; Agarwal, A.; Gerhardt, R. A.; Shih, C. C.; Shih, C. M.; Lin, S. J.; Su, Y. Y.; Ramamurti, R.; Singh, R. N. Microstructural and biological properties of nanocrystalline diamond coatings. *Diamond Relat. Mater.* **2006**, 15, 1935-40.

[48] Golini, D.; Jacobs, S. D. Physics of Loose Abrasive Microgrinding. *Appl. Optics* **1991**, 30, 2761-77.

[49] Oles, E. J.; Inspektor, A.; Bauer, C. E. The new diamond-coated carbide cutting tools. *Diamond Relat. Mater.* **1996**, 5, 617-24.

[50] Jang, S. P.; Choi, S. U. S. Cooling performance of a microchannel heat sink with nanofluids. *Appl. Therm. Eng.* **2006**, 26, 2457-63.

[51] Monroy, E.; Omnes, F.; Calle, F. Wide-bandgap semiconductor ultraviolet photodetectors. *Semicond. Sci. Technol.* **2003**, 18, R33-R51.

[52] Okano, K.; Koizumi, S.; Silva, S. R. P.; Amaratunga, G. A. J. Low-threshold cold cathodes made of nitrogen-doped chemical-vapour-deposited diamond. *Nature* **1996**, 381, 140-1.

[53] Daniel, M. C.; Astruc, D. Gold nanoparticles: Assembly, supramolecular chemistry, quantum-size-related properties, and applications toward biology, catalysis, and nanotechnology. *Chem. Rev.* **2004**, 104, 293-346.

[54] Panyam, J.; Labhasetwar, V. Biodegradable nanoparticles for drug and gene delivery to cells and tissue. *Adv. Drug Deliver. Rev.* **2003**, 55, 329-47.

[55] Medintz, I. L.; Uyeda, H. T.; Goldman, E. R.; Mattoussi, H. Quantum dot bioconjugates for imaging, labelling and sensing. *Nat. Mater.* **2005**, 4, 435-46.

[56] Niwase, K.; Tanaka, T.; Kakimoto, Y.; Ishihara, K. N.; Shingu, P. H. Raman-Spectra of Graphite and Diamond Mechanically Milled with Agate or Stainless-Steel Ball-Mill. *Mater. T. Jim* **1995**, 36, 282-8.

[57] Iijima, S. *Japanese Patent JP 04132606* **1992**,

[58] Frenklach, M.; Kematick, R.; Huang, D.; Howard, W.; Spear, K. E.; Phelps, A. W.; Koba, R. Homogeneous Nucleation of Diamond Powder in the Gas-Phase. *J. Appl. Phys.* **1989**, 66, 395-9.

[59] Novikov, N. V. New trends in high-pressure synthesis of diamond. *Diamond Relat. Mater.* **1999**, 8, 1427-32.

[60] Danilenko, V. V. On the history of the discovery of nanodiamond synthesis. *Phys. Solid State* **2004**, 46, 595-9.

[61] Kruger, A.; Kataoka, F.; Ozawa, M.; Fujino, T.; Suzuki, Y.; Aleksenskii, A. E.; Vul', A. Y.; Osawa, E. Unusually tight aggregation in detonation nanodiamond: Identification and disintegration. *Carbon* **2005**, 43, 1722-30.

[62] Krueger, A. The structure and reactivity of nanoscale diamond. *J. Mater. Chem.* **2008**, 18, 1485-92.

[63] Shenderova, O. A. Ultrananocrystalline diamond. *William Andrew Publishing, Norwich, N.*

Y. **2006**

[64] Krueger, A. Diamond nanoparticles: Jewels for chemistry and physics. *Adv. Mater.* **2008**, 20, 2445-9.

[65] Gupta, A. K.; Gupta, M. Synthesis and surface engineering of iron oxide nanoparticles for biomedical applications. *Biomaterials* **2005**, 26, 3995-4021.

[66] Aleksenskii, A. E.; Baidakova, M. V.; Vul', A. Y.; Siklitskii, V. I. The structure of diamond nanoclusters. *Phys. Solid State* **1999**, 41, 668-71.

[67] Loktev, V. F.; Makalskii, V. I.; Stoyanova, I. V.; Kalinkin, A. V.; Likholobov, V. A.; Mitkin, V. N. Surface Modification of Ultradispersed Diamonds. *Carbon* **1991**, 29, 817-9.

[68] Ushizawa, K.; Sato, Y.; Mitsumori, T.; Machinami, T.; Ueda, T.; Ando, T. Covalent immobilization of DNA on diamond and its verification by diffuse reflectance infrared spectroscopy. *Chem. Phys. Lett.* **2002**, 351, 105-8.

[69] Kruger, A.; Liang, Y. J.; Jarre, G.; Stegk, J. Surface functionalisation of detonation diamond suitable for biological applications. *J. Mater. Chem.* **2006**, 16, 2322-8.

[70] Fu, C. C.; Lee, H. Y.; Chen, K.; Lim, T. S.; Wu, H. Y.; Lin, P. K.; Wei, P. K.; Tsao, P. H.; Chang, H. C.; Fann, W. Characterization and application of single fluorescent nanodiamonds as cellular biomarkers. *P. Natl. Acad. Sci. USA* **2007**, 104, 727-32.

[71] Yu, S. J.; Kang, M. W.; Chang, H. C.; Chen, K. M.; Yu, Y. C. Bright fluorescent nanodiamonds: No photobleaching and low cytotoxicity. *J. Am. Chem. Soc.* **2005**, 127, 17604-5.

[72] Chao, J. I.; Perevedentseva, E.; Chung, P. H.; Liu, K. K.; Cheng, C. Y.; Chang, C. C.;

Cheng, C. L. Nanometer-sized diamond particle as a probe for biolabeling. *Biophys. J.* **2007**, 93, 2199-208.

[73] Osswald, S.; Yushin, G.; Mochalin, V.; Kucheyev, S. O.; Gogotsi, Y. Control of sp(2)/sp(3) carbon ratio and surface chemistry of nanodiamond powders by selective oxidation in air. *J. Am. Chem. Soc.* **2006**, 128, 11635-42.

[74] Enoki, T.; Kobayashi, Y.; Katsuyama, C.; Osipov, V. Y.; Baidakova, M. V.; Takai, K.; Fukui, K. I.; Vul, A. Y. Structures and electronic properties of surface/edges of nanodiamond and nanographite. *Diamond Relat. Mater.* **2007**, 16, 2029-34.

[75] Xu, X. Y.; Yu, Z. M.; Zhu, Y. W.; Wang, B. C. Influence of surface modification adopting thermal treatments on dispersion of detonation nanodiamond. *J. Solid State Chem.* **2005**, 178, 688-93.

[76] Mitev, D.; Dimitrova, R.; Spassova, M.; Minchev, C.; Stavrev, S. Surface peculiarities of detonation nanodiamonds in dependence of fabrication and purification methods. *Diamond Relat. Mater.* **2007**, 16, 776-80.

[77] Shenderova, O.; Petrov, I.; Walsh, J.; Grichko, V.; Grishko, V.; Tyler, T.; Cunningham, G. Modification of detonation nanodiamonds by heat treatment in air. *Diamond Relat. Mater.* **2006**, 15, 1799-803.

[78] Pichot, V.; Comet, M.; Fousson, E.; Baras, C.; Senger, A.; Le Normand, F.; Spitzer, D. An efficient purification method for detonation nanodiamonds. *Diamond Relat. Mater.* **2008**, 17, 13-22.

[79] John, P.; Polwart, N.; Troupe, C. E.; Wilson, J. I. B. The oxidation of (100) textured

diamond. *Diamond Relat. Mater.* **2002**, 11, 861-6.

[80] Yeap, W. S.; Tan, Y. Y.; Loh, K. P. Using detonation nanodiamond for the specific capture of glycoproteins. *Anal. Chem.* **2008**, 80, 4659-65.

[81] Spitsyn, B. V.; Davidson, J. L.; Gradoboev, M. N.; Galushko, T. B.; Serebryakova, N. V.; Karpukhina, T. A.; Kulakova, I. I.; Melnik, N. N. Inroad to modification of detonation nanodiamond. *Diamond Relat. Mater.* **2006**, 15, 296-9.

[82] Liu, Y.; Gu, Z. N.; Margrave, J. L.; Khabashesku, V. N. Functionalization of nanoscale diamond powder: Fluoro-, alkyl-, amino-, and amino acid-nanodiamond derivatives. *Chem. Mater.* **2004**, 16, 3924-30.

[83] Lisichkin, G. V.; Korol'kov, V. V.; Tarasevich, B. N.; Kulakova, I. I.; Karpukhin, A. V. Photochemical chlorination of nanodiamond and interaction of its modified surface with C-nucleophiles. *Russ. Chem. B.* **2006**, 55, 2212-9.

[84] Jenkins, A. D.; Kratochvíl, P.; Stepto, R. F. T.; Suter, U. W. Glossary of Basic Terms in Polymer Science. *Pure Appl. Chem. (IUPAC Official Journal)* **1996**, 68, 2287-311.

[85] Puzyr, A. P.; Baron, A. V.; Purtov, K. V.; Bortnikov, E. V.; Skobelev, N. N.; Moginaya, O. A.; Bondar, V. S. Nanodiamonds with novel properties: A biological study. *Diamond Relat. Mater.* **2007**, 16, 2124-8.

[86] Liu, K. K.; Chen, F.; Chen, P. Y.; Lee, T. J. F.; Cheng, C. L.; Chang, C. C.; Ho, Y. P.; Chao, J. I. Alpha-bungarotoxin binding to target cell in a developing visual system by carboxylated nanodiamond. *Nanotechnology* **2008**, 19, 205102.

[87] Puzyr, A. P.; Baron, A. V.; Purtov, K. V.; Bortnikov, E. V.; Skobelev, N. N.; Moginaya, O.

A.; Bondar, V. S. Nanodiamonds with novel properties: A biological study. *Diamond Relat. Mater.* **2007**, 16, 2124-8.

[88] Kong, X. L.; Huang, L. C. L.; Hsu, C. M.; Chen, W. H.; Han, C. C.; Chang, H. C. High-affinity capture of proteins by diamond nanoparticles for mass spectrometric analysis. *Anal. Chem.* **2005**, 77, 259-65.

[89] Puzyr', A. P.; Pozdnyakova, I. O.; Bondar', V. S. Design of a luminescent biochip with nanodiamonds and bacterial luciferase. *Phys. Solid State* **2004**, 46, 761-3.

[90] Gruber, A.; Drabenstedt, A.; Tietz, C.; Fleury, L.; Wrachtrup, J.; vonBorczyskowski, C. Scanning confocal optical microscopy and magnetic resonance on single defect centers. *Science* **1997**, 276, 2012-4.

[91] Harley, R. T.; Henderson, M. J.; Macfarlane, R. M. Persistent Spectral Hole Burning of Color-Centers in Diamond. *J. Phys. C Solid State* **1984**, 17, L233-L6.

[92] Reddy, N. R. S.; Manson, N. B.; Krausz, E. R. 2-Laser Spectral Hole Burning in a Color Center in Diamond. *J. Lumin.* **1987**, 38, 46-7.

[93] Chang, Y. R.; Lee, H. Y.; Chen, K.; Chang, C. C.; Tsai, D. S.; Fu, C. C.; Lim, T. S.; Tzeng, Y. K.; Fang, C. Y.; Han, C. C.; Chang, H. C.; Fann, W. Mass production and dynamic imaging of fluorescent nanodiamonds. *Nat. Nanotechnol.* **2008**, 3, 284-8.

[94] Loubser, J.; Vanwyk, J. A. Electron-Spin Resonance in Study of Diamond. *Rep. Prog. Phys.* **1978**, 41, 1201-48.

[95] Crossfie, M.; Davies, G.; Collins, A. T.; Lightowl.Ec Role of Defect Interactions in Reducing Decay Time of H-3 Luminescence in Diamond. *J. Phys. C Solid State* **1974**, 7,

1909-17.

[96] Gaebel, T.; Popa, I.; Gruber, A.; Domhan, M.; Jelezko, F.; Wrachtrup, J. Stable single-photon source in the near infrared. *New J. Phys.* **2004**, 6, 98.

[97] Wang, H. D.; Chu, L. Y.; Song, H.; Yang, J. P.; Xie, R.; Yang, M. Preparation and enantiomer separation characteristics of chitosan/beta-cyclodextrin composite membranes. *J. Membrane Sci.* **2007**, 297, 262-70.

[98] Yu, L. Biodegradable polymer blends and composites from renewable resources. *John Wiley & Sons, Inc.* **2009**, 118.

[99] Kennedy, R.; Costain, D. J.; McAlister, V. C.; Lee, T. D. G. *Surgery* **1996**, 120, 866.

[100] Chen, L. Y.; Tian, Z. G.; Du, Y. M. Synthesis and pH sensitivity of carboxymethyl chitosan-based polyampholyte hydrogels for protein carrier matrices. *Biomaterials* **2004**, 25, 3725.

[101] Chen, S. C.; Wu, Y. C.; Mi, F. L.; Lin, Y. H.; Yu, L. C.; Sung, H. W. A novel pH-sensitive hydrogel composed of N,O-carboxymethyl chitosan and alginate cross-linked by genipin for protein drug delivery. *J. Control. Release* **2004**, 96, 285.

[102] Lin, Y. H.; Liang, H. F.; Chung, C. K.; Chen, M. C.; Sung, H. W. Physically crosslinked alginate/N,O-carboxymethyl chitosan hydrogels with calcium for oral delivery of protein drugs. *Biomaterials* **2005**, 26, 2105.

[103] Mi, F. L.; Liang, H. F.; Wu, Y. C.; Lin, Y. S.; Yang, T. F.; Sung, H. W. pH-sensitive behavior of two-component hydrogels composed of N,O-carboxymethyl chitosan and alginate. *J. Biomat. Sci.-Polym. E.* **2005**, 16, 1333.

[104] Neoh, K. G.; Shi, Z. L.; Kang, E. T.; Poh, C. K.; Wang, W. Surface Functionalization of Titanium with Carboxymethyl Chitosan and Immobilized Bone Morphogenetic Protein-2 for Enhanced Osseointegration. *Biomacromolecules* **2009**, 10, 1603-11.

[105] Elsabee, M. Z.; Abdou, E. S.; Nagy, K. S. A.; Eweis, M. Surface modification of polypropylene films by chitosan and chitosan/pectin multilayer. *Carbohyd. Polym.* **2008**, 71, 187-95.

[106] Guan, W. C.; Ke, G.; Tang, C. Y.; Guan, W. J.; Deng, F. Covalent functionalization of multiwalled carbon nanotubes with a low molecular weight chitosan. *Biomacromolecules* **2007**, 8, 322-6.

[107] Liu, Y. Y.; Tang, J.; Chen, X. Q.; Xin, J. H. Decoration of carbon nanotubes with chitosan. *Carbon* **2005**, 43, 3178-80.

[108] Wang, S. F.; Shen, L.; Zhang, W. D.; Tong, Y. J. Preparation and mechanical properties of chitosan/carbon nanotubes composites. *Biomacromolecules* **2005**, 6, 3067-72.

[109] Feng, W.; Wu, Z. G.; Feng, Y. Y.; Liu, Q.; Xu, X. H.; Sekino, T.; Fujii, A.; Ozaki, M. Preparation and characterization of chitosan-grafted multiwalled carbon nanotubes and their electrochemical properties. *Carbon* **2007**, 45, 1212-8.

[110] Cheng, J. L.; He, J. P.; Li, C. X.; Yang, Y. L. Facile approach to functionalize nanodiamond particles with V-shaped polymer brushes. *Chem. Mater.* **2008**, 20, 4224-30.

[111] Li, L.; Davidson, J. L.; Lukehart, C. M. Surface functionalization of nanodiamond particles via atom transfer radical polymerization. *Carbon* **2006**, 44, 2308-15.

[112] Nakajima, N.; Ikada, Y. Mechanism of Amide Formation by Carbodiimide for

Bioconjugation in Aqueous-Media. *Bioconjugate Chem.* **1995**, 6, 123-30.

[113] Bernkop-Schnurch, A.; Kast, C. E. Thiolated polymers - thiomers: development and in vitro evaluation of chitosan-thioglycolic acid conjugates. *Biomaterials* **2001**, 22, 2345-52.

[114] Auzely-Velty, R.; Szarpak, A.; Pignot-Paintrand, I.; Nicolas, C.; Picart, C. Multilayer assembly of hyaluronic acid/poly(allylamine): Control of the buildup for the production of hollow capsules. *Langmuir* **2008**, 24, 9767-74.

[115] van Wachem, P. B.; Plantinga, J. A.; Wissink, M. J. B.; Beernink, R.; Poot, A. A.; Engbers, G. H. M.; Beugeling, T.; van Aken, W. G.; Feijen, J.; van Luyn, M. J. A. In vivo biocompatibility of carbodiimide-crosslinked collagen matrices: Effects of crosslink density, heparin immobilization, and bFGF loading. *J. Biomed. Mater. Res.* **2001**, 55, 368-78.

[116] Sannino, A.; Pappada, S.; Madaghiele, M.; Maffezzoli, A.; Ambrosio, L.; Nicolais, L. Crosslinking of cellulose derivatives and hyaluronic acid with water-soluble carbodiimide. *Polymer* **2005**, 46, 11206-12.

[117] Katz, E.; Willner, I. Integrated nanoparticle-biomolecule hybrid systems: Synthesis, properties, and applications. *Angew. Chem. Int. Ed.* **2004**, 43, 6042-108.

[118] Roach, P.; Farrar, D.; Perry, C. C. Surface tailoring for controlled protein adsorption: Effect of topography at the nanometer scale and chemistry. *J. Am. Chem. Soc.* **2006**, 128, 3939-45.

[119] Dalton, A. B.; Ortiz-Acevedo, A.; Zorbas, V.; Brunner, E.; Sampson, W. M.; Collins, L.; Razal, J. M.; Yoshida, M. M.; Baughman, R. H.; Draper, R. K.; Musselman, I. H.;

Jose-Yacaman, M.; Dieckmann, G. R. Hierarchical self-assembly of peptide-coated carbon nanotubes. *Adv. Funct. Mater.* **2004**, 14, 1147-51.

[120] Whitesides, G. M.; Boncheva, M. Beyond molecules: Self-assembly of mesoscopic and macroscopic components. *P. Natl. Acad. Sci. USA* **2002**, 99, 4769-74.

[121] Yang, W. S.; Auciello, O.; Butler, J. E.; Cai, W.; Carlisle, J. A.; Gerbi, J.; Gruen, D. M.; Knickerbocker, T.; Lasseter, T. L.; Russell, J. N.; Smith, L. M.; Hamers, R. J. DNA-modified nanocrystalline diamond thin-films as stable, biologically active substrates. *Nat. Mater.* **2002**, 1, 253-7.

[122] Nesladek, M. Conventional n-type doping in diamond: state of the art and recent progress. *Semicond. Sci. Technol.* **2005**, 20, R19-R27.

[123] Teraji, T.; Hamada, M.; Wada, H.; Yamamoto, M.; Arima, K.; Ito, T. High rate growth and electrical/optical properties of high-quality homoepitaxial diamond(100) films. *Diamond Relat. Mater.* **2005**, 14, 255-60.

[124] Swain, G. M.; Granger, M. C.; Witek, M.; Xu, J. S.; Wang, J.; Hupert, M.; Hanks, A.; Koppang, M. D.; Butler, J. E.; Lucazeau, G.; Mermoux, M.; Strojek, J. W. Standard electrochemical behavior of high-quality, boron-doped polycrystalline diamond thin-film electrodes. *Anal. Chem.* **2000**, 72, 3793-804.

[125] Swain, G. M.; Hupert, M.; Muck, A.; Wang, R.; Stotter, J.; Cvackova, Z.; Haymond, S.; Show, Y. Conductive diamond thin-films in electrochemistry. *Diamond Relat. Mater.* **2003**, 12, 1940-9.

[126] Butler, J. E.; Mankelevich, Y. A.; Cheesman, A.; Ma, J.; Ashfold, M. N. R. Understanding

the chemical vapor deposition of diamond: recent progress. *J. Phys. Condens. Matter* **2009**, 21, 364201.

[127] Strother, T.; Knickerbocker, T.; Russell, J. N.; Butler, J. E.; Smith, L. M.; Hamers, R. J. Photochemical functionalization of diamond films. *Langmuir* **2002**, 18, 968-71.

[128] Christiaens, P.; Vermeeren, V.; Wenmackers, S.; Daenen, M.; Haenen, K.; Nesladek, M.; vandeVen, M.; Ameloot, M.; Michiels, L.; Wagner, P. EDC-mediated DNA attachment to nanocrystalline CVD diamond films. *Biosens. Bioelectron.* **2006**, 22, 170-7.

[129] Liu, Y.; Khabashesku, V. N.; Halas, N. J. Fluorinated nanodiamond as a wet chemistry precursor for diamond coatings covalently bonded to glass surface. *J. Am. Chem. Soc.* **2005**, 127, 3712-3.

[130] Decher, G. Fuzzy nanoassemblies: Toward layered polymeric multicomposites. *Science* **1997**, 277, 1232-7.

[131] Hammond, P. T. Form and function in multilayer assembly: New applications at the nanoscale. *Adv. Mater.* **2004**, 16, 1271-93.

[132] Kinnane, C. R.; Such, G. K.; Caruso, F. Tuning the Properties of Layer-by-Layer Assembled Poly(acrylic acid) Click Films and Capsules. *Macromolecules* **2011**, 44, 1194-202.

[133] Decher, G.; Hong, J. D.; Schmitt, J. Buildup of Ultrathin Multilayer Films by a Self-Assembly Process .3. Consecutively Alternating Adsorption of Anionic and Cationic Polyelectrolytes on Charged Surfaces. *Thin Solid Films* **1992**, 210, 831-5.

[134] Decher, G.; Lvov, Y.; Schmitt, J. Proof of Multilayer Structural Organization in

Self-Assembled Polycation Polyanion Molecular Films. *Thin Solid Films* **1994**, 244, 772-7.

[135] Ramsden, J. J.; Lvov, Y. M.; Decher, G. Determination of Optical-Constants of Molecular Films Assembled Via Alternate Polyion Adsorption. *Thin Solid Films* **1995**, 254, 246-51.

[136] Kipper, M. J.; Boddohi, S.; Almodovar, J.; Zhang, H.; Johnson, P. A. Layer-by-layer assembly of polysaccharide-based nanostructured surfaces containing polyelectrolyte complex nanoparticles. *Colloid. Surface. B* **2010**, 77, 60-8.

[137] Rinzler, A. G.; Wu, Z. C.; Chen, Z. H.; Du, X.; Logan, J. M.; Sippel, J.; Nikolou, M.; Kamaras, K.; Reynolds, J. R.; Tanner, D. B.; Hebard, A. F. Transparent, conductive carbon nanotube films. *Science* **2004**, 305, 1273-6.

[138] Shao-Horn, Y.; Lee, S. W.; Kim, B. S.; Chen, S.; Hammond, P. T. Layer-by-Layer Assembly of All Carbon Nanotube Ultrathin Films for Electrochemical Applications. *J. Am. Chem. Soc.* **2009**, 131, 671-9.

[139] Hu, N. F.; Zhao, L. Y.; Liu, H. Y. Assembly of layer-by-layer films of heme proteins and single-walled carbon nanotubes: electrochemistry and electrocatalysis. *Anal. Bioanal. Chem.* **2006**, 384, 414-22.

[140] Rouse, J. H.; Lillehei, P. T. Electrostatic assembly of polymer/single walled carbon nanotube multilayer films. *Nano Lett.* **2003**, 3, 59-62.

[141] Paloniemi, H.; Lukkarinen, M.; Aaritalo, T.; Areva, S.; Leiro, J.; Heinonen, M.; Haapakka, K.; Lukkari, J. Layer-by-layer electrostatic self-assembly of single-wall carbon nanotube polyelectrolytes. *Langmuir* **2006**, 22, 74-83.

[142] Hongthani, W.; Fermin, D. J. Layer-by-Layer assembly and redox properties of undoped HPHT diamond particles. *Diamond Relat. Mater.* **2010**, 19, 680-4.

[143] Saini, G.; Jensen, D. S.; Wiest, L. A.; Vail, M. A.; Dadson, A.; Lee, M. L.; Shutthanandan, V.; Linford, M. R. Core-Shell Diamond as a Support for Solid-Phase Extraction and High-Performance Liquid Chromatography. *Anal. Chem.* **2010**, 82, 4448-56.

[144] Lim, D. S.; Kim, J. H.; Lee, S. K.; Kwon, O. M.; Hong, S. I. Thickness controlled and smooth polycrystalline CVD diamond film deposition on SiO(2) with electrostatic self assembly seeding process. *Diamond Relat. Mater.* **2009**, 18, 1218-22.

[145] Lim, D. S.; Lee, S. K.; Kim, J. H.; Jeong, M. G.; Song, M. J. Direct deposition of patterned nanocrystalline CVD diamond using an electrostatic self-assembly method with nanodiamond particles. *Nanotechnology* **2010**, 21, 505302.

[146] Fermin, D. J.; Hongthani, W. H., W.; Fox, N. A. Electrochemical Properties of Two Dimensional Assemblies of Insulating Diamond Particles. *Langmuir* **2011**, 27, 5112-8.

[147] Mautner, M. M. N.; Sieck, L. W.; Liebman, J. F.; Scheiner, S. Complexing of the ammonium ion by polyethers. Comparative complexing thermochemistry of ammonium, hydronium, and alkali cations. *J. Phys. Chem.* **1996**, 100, 6445-50.

[148] Terranova, M. L.; Orlanducci, S.; Tamburri, E.; Guglielmotti, V.; Toschi, F.; Hampai, D.; Rossi, M. Polycrystalline diamond on self-assembled detonation nanodiamond: a viable route for fabrication of all-diamond preformed microcomponents. *Nanotechnology* **2008**, 19, 415601.

[149] Robinson, T.; McMullan, G.; Marchant, R.; Nigam, P. Remediation of dyes in textile

effluent: a critical review on current treatment technologies with a proposed alternative. *Bioresource Technol.* **2001**, 77, 247-55.

[150] Crini, G. Non-conventional low-cost adsorbents for dye removal: A review. *Bioresource Technol.* **2006**, 97, 1061-85.

[151] Song, Z.; Chen, L. F.; Hu, J. C.; Richards, R. NiO(111) nanosheets as efficient and recyclable adsorbents for dye pollutant removal from wastewater. *Nanotechnology* **2009**, 20, 275707.

[152] Crini, G. Studies on adsorption of dyes on beta-cyclodextrin polymer. *Bioresource Technol.* **2003**, 90, 193-8.

[153] Sun, Q. Y.; Yang, L. Z. The adsorption of basic dyes from aqueous solution on modified peat-resin particle. *Water Res.* **2003**, 37, 1535-44.

[154] Ghoreishi, S. M.; Haghighi, R. Chemical catalytic reaction and biological oxidation for treatment of non-biodegradable textile effluent. *Chem. Eng. J.* **2003**, 95, 163-9.

[155] Jain, A. K.; Gupta, V. K.; Bhatnagar, A.; Suhas Utilization of industrial waste products as adsorbents for the removal of dyes. *J. Hazard. Mater.* **2003**, 101, 31-42.

[156] Ho, Y. S.; McKay, G. Sorption of dyes and copper ions onto biosorbents. *Process Biochem.* **2003**, 38, 1047-61.

[157] Li, J.; Qu, G. Z.; Wu, Y.; Li, G. F.; Li, D. Regeneration of acid orange 7-exhausted granular activated carbon with dielectric barrier discharge plasma. *Chem. Eng. J.* **2009**, 146, 168-73.

[158] Gercel, O.; Gercel, H. F. Removal of Acid Dyes from Aqueous Solutions using

Chemically Activated Carbon. *Separ. Sci. Technol.* **2009**, 44, 2078-95.

[159] Quan, M.; Liu, X. T.; Bo, L. L.; Chen, S.; Zhao, Y. Z.; Cui, X. Y. Regeneration of acid orange 7-exhausted granular activated carbons with microwave irradiation. *Water Res.* **2004**, 38, 4484-90.

[160] Xu, D.; Hein, S.; Loo, S. L.; Wang, K. The Fixed-Bed Study of Dye Removal on Chitosan Beads at High pH. *Ind. Eng. Chem. Res.* **2008**, 47, 8796-800.

[161] Chiou, M. S.; Li, H. Y. Adsorption behavior of reactive dye in aqueous solution on chemical cross-linked chitosan beads. *Chemosphere* **2003**, 50, 1095-105.

[162] Duplay, J.; Errais, E.; Darragi, F.; M'Rabet, I.; Aubert, A.; Huber, F.; Morvan, G. Efficient anionic dye adsorption on natural untreated clay: Kinetic study and thermodynamic parameters. *Desalination* **2011**, 275, 74-81.

[163] Akar, S. T.; Uysal, R. Untreated clay with high adsorption capacity for effective removal of C.I. Acid Red 88 from aqueous solutions: Batch and dynamic flow mode studies. *Chem. Eng. J.* **2010**, 162, 591-8.

[164] Nayak, S.; Lyon, L. A. Soft nanotechnology with soft nanoparticles. *Angew. Chem. Int. Edit.* **2005**, 44, 7686-708.

[165] Meng, H.; Chen, X. W.; Wang, J. H. Ionic liquid templated porous nano-TiO2 particles for the selective isolation of cytochrome c. *Nanotechnology* **2010**, 21, 385704.

[166] Chang, Y. C.; Chen, D. H. Preparation and adsorption properties of monodisperse chitosan-bound Fe3O4 magnetic nanoparticles for removal of Cu(II) ions. *J. Colloid Interf. Sci.* **2005**, 283, 446-51.

[167] Wu, S. F.; Zhu, Y. Q. Behavior of CaTiO3/Nano-CaO as a CO2 Reactive Adsorbent. *Ind. Eng. Chem. Res.* **2010**, 49, 2701-6.

[168] Mauter, M. S.; Elimelech, M. Environmental applications of carbon-based nanomaterials. *Environ. Sci. Technol.* **2008**, 42, 5843-59.

[169] Pan, B.; Xing, B. S. Adsorption Mechanisms of Organic Chemicals on Carbon Nanotubes. *Environ. Sci. Technol.* **2008**, 42, 9005-13.

[170] Long, R. Q.; Yang, R. T. Carbon nanotubes as superior sorbent for dioxin removal. *J. Am. Chem. Soc.* **2001**, 123, 2058-9.

[171] Upadhyayula, V. K. K.; Deng, S. G.; Smith, G. B.; Mitchell, M. C. Adsorption of Bacillus subtilis on single-walled carbon nanotube aggregates, activated carbon and NanoCeram (TM). *Water Res.* **2009**, 43, 148-56.

[172] Yan, H.; Gong, A. J.; He, H. S.; Zhou, J.; Wei, Y. X.; Lv, L. Adsorption of microcystins by carbon nanotubes. *Chemosphere* **2006**, 62, 142-8.

[173] Li, Y. H.; Wang, S. G.; Wei, J. Q.; Zhang, X. F.; Xu, C. L.; Luan, Z. K.; Wu, D. H.; Wei, B. Q. Lead adsorption on carbon nanotubes. *Chem. Phys. Lett.* **2002**, 357, 263-6.

[174] Li, Y. H.; Ding, J.; Luan, Z. K.; Di, Z. C.; Zhu, Y. F.; Xu, C. L.; Wu, D. H.; Wei, B. Q. Competitive adsorption of Pb2+, Cu2+ and Cd2+ ions from aqueous solutions by multiwalled carbon nanotubes. *Carbon* **2003**, 41, 2787-92.

[175] Velten, S.; Knappe, D. R. U.; Traber, J.; Kaiser, H. P.; von Gunten, U.; Boller, M.; Meylan, S. Characterization of natural organic matter adsorption in granular activated carbon adsorbers. *Water Res.* **2011**, 45, 3951-9.

[176] Vidic, R. D.; Liu, W.; Brown, T. D. Optimization of sulfur impregnation protocol for fixed bed application of activated carbon-based sorbents for gas-phase mercury removal. *Environ. Sci. Technol.* **1998**, 32, 531-8.

[177] Pelekani, C.; Snoeyink, V. L. Competitive adsorption in natural water: Role of activated carbon pore size. *Water Res.* **1999**, 33, 1209-19.

[178] Lu, C. S.; Chung, Y. L.; Chang, K. F. Adsorption of trihalomethanes from water with carbon nanotubes. *Water Res.* **2005**, 39, 1183-9.

[179] Yang, R. T.; Long, R. Q. Carbon nanotubes as superior sorbent for dioxin removal. *J. Am. Chem. Soc.* **2001**, 123, 2058-9.

[180] Li, Y. H.; Wang, S. G.; Zhang, X. F.; Wei, J. Q.; Xu, C. L.; Luan, Z. K.; Wu, D. H. Adsorption of fluoride from water by aligned carbon nanotubes. *Mater. Res. Bull.* **2003**, 38, 469-76.

[181] Brinson, L. C.; Ramanathan, T.; Abdala, A. A.; Stankovich, S.; Dikin, D. A.; Herrera-Alonso, M.; Piner, R. D.; Adamson, D. H.; Schniepp, H. C.; Chen, X.; Ruoff, R. S.; Nguyen, S. T.; Aksay, I. A.; Prud'homme, R. K. Functionalized graphene sheets for polymer nanocomposites. *Nat. Nanotechnol.* **2008**, 3, 327-31.

[182] Lu, C.; Chiu, H.; Bai, H. Comparisons of adsorbent cost for the removal of zinc (II) from aqueous solution by carbon nanotubes and activated carbon. *J. Nanosci. Nanotechnol.* **2007**, 7, 1647-52.

[183] Steinmuller-Nethl, D.; Kloss, F. R.; Najam-U-Haq, M.; Rainer, M.; Larsson, K.; Linsmeier, C.; Koehler, G.; Fehrer, C.; Lepperdinger, G.; Liu, X.; Memmel, N.; Bertel, E.;

Huck, C. W.; Gassner, R.; Bonn, G. Strong binding of bioactive BMP-2 to nanocrystalline diamond by physisorption. *Biomaterials* **2006**, 27, 4547-56.

[184] Bondar', V. S.; Pozdnyakova, I. O.; Puzyr', A. P. Applications of nanodiamonds for separation and purification of proteins. *Phys. Solid State* **2004**, 46, 758-60.

[185] Kong, X. L.; Huang, L. C. L.; Liau, S. C. V.; Han, C. C.; Chang, H. C. Polylysine-coated diamond nanocrystals for MALDI-TOF mass analysis of DNA oligonucleotides. *Anal. Chem.* **2005**, 77, 4273-7.

[186] Gibson, N. M.; Luo, T. J. M.; Shenderova, O.; Choi, Y. J.; Fitzgerald, Z.; Brenner, D. W. Fluorescent dye adsorption on nanocarbon substrates through electrostatic interactions. *Diamond Relat. Mater.* **2010**, 19, 234-7.

[187] Chen, X. G.; Park, H. J. Chemical characteristics of O-carboxymethyl chitosans related to the preparation conditions. *Carbohyd. Polym.* **2003**, 53, 355.

[188] Muzzarelli, R. A. A. Carboxymethylated Chitins and Chitosans. *Carbohyd Polym* **1988**, 8, 1.

[189] Chen, J.; Deng, S. Z.; Chen, J.; Yu, Z. X.; Xu, N. S. Graphitization of nanodiamond powder annealed in argon ambient. *Appl. Phys. Lett.* **1999**, 74, 3651.

[190] Nakanishi, K.; Sakiyama, T.; Imamura, K. On the adsorption of proteins on solid surfaces, a common but very complicated phenomenon. *J. Biosci. Bioeng.* **2001**, 91, 233-44.

[191] Karajanagi, S. S.; Vertegel, A. A.; Kane, R. S.; Dordick, J. S. Structure and function of enzymes adsorbed onto single-walled carbon nanotubes. *Langmuir* **2004**, 20, 11594-9.

[192] Forato, L. A.; Bernardes, R.; Colnago, L. A. Protein structure in KBr pellets by infrared

spectroscopy. *Anal. Biochem.* **1998**, 259, 136-41.

[193] Souillac, P. O.; Middaugh, C. R.; Rytting, J. H. Investigation of protein/carbohydrate interactions in the dried state. 2. Diffuse reflectance FTIR studies. *Int. J. Pharm.* **2002**, 235, 207-18.

[194] Creighton, T. E. *Protein Structure: A Practical Approach, Second ed.* **1997**, (Oxford, New York).

[195] Wang, Y. S.; Jiang, Q.; Liu, L. R.; Zhang, Q. Q. The interaction between bovine serum albumin and the self-aggregated nanoparticles of cholesterol-modified O-carboxymethyl chitosan. *Polymer* **2007**, 48, 4135-42.

[196] Shang, L.; Wang, Y. Z.; Jiang, J. G.; Dong, S. J. pH-dependent protein conformational changes in albumin : gold nanoparticle bioconjugates: A spectroscopic study. *Langmuir* **2007**, 23, 2714-21.

[197] Buijs, J.; Norde, W.; Lichtenbelt, J. W. T. Changes in the secondary structure of adsorbed IgG and F(ab')(2) studied by FTIR spectroscopy. *Langmuir* **1996**, 12, 1605-13.

[198] Jackson, M.; Mantsch, H. H. The Use and Misuse of Ftir Spectroscopy in the Determination of Protein-Structure. *Crit. Rev. Biochem. Mol.* **1995**, 30, 95-120.

[199] Vass, E.; Hollosi, M.; Besson, F.; Buchet, R. Vibrational spectroscopic detection of beta- and gamma-turns in synthetic and natural peptides and proteins. *Chem. Rev.* **2003**, 103, 1917-54.

[200] Roach, P.; Farrar, D.; Perry, C. C. Interpretation of protein adsorption: Surface-induced conformational changes. *J. Am. Chem. Soc.* **2005**, 127, 8168-73.

[201] Giacomelli, C. E.; Bremer, M. G. E. G.; Norde, W. ATR-FTIR study of IgG adsorbed on different silica surfaces. *J. Colloid Interface Sci.* **1999**, 220, 13-23.

[202] Dong, A.; Huang, P.; Caughey, W. S. Redox-Dependent Changes in Beta-Extended Chain and Turn Structures of Cytochrome-C in Water Solution Determined by 2Nd Derivative Amide-I Infrared-Spectra. *Biochemistry-Us* **1992**, 31, 182-9.

[203] Kanakis, C. D.; Tarantilis, P. A.; Polissiou, M. G.; Diamantoglou, S.; Tajmir-Riahi, H. A. Antioxidant flavonoids bind human serum albumin. *J. Mol. Struct.* **2006**, 798, 69-74.

[204] Pi, Y. Y.; Shang, Y. Z.; Peng, C. J.; Liu, H. L.; Hu, Y.; Jiang, J. W. Interactions between bovine serum albumin and gemini surfactant alkanediyl-alpha, omega-bis(dimethyidodecyl-ammonium bromide). *Biopolymers* **2006**, 83, 243-9.

[205] Panyala, N. R.; Pena-Mendez, E. M.; Havel, J. Gold and nano-gold in medicine: overview, toxicology and perspectives. *J. Appl. Biomed.* **2009**, 7, 75-91.

[206] Albani, J. R. Structure and Dynamics of Macromolecules: Absorption and Fluorescence Studies. Amsterdam: Elsevier pp 141-192; 2004.

[207] Royer, C. A. Probing protein folding and conformational transitions with fluorescence. *Chem. Rev.* **2006**, 106, 1769-84.

[208] Yang, Y. Y.; Chung, T. S.; Ng, N. P. Morphology, drug distribution, and in vitro release profiles of biodegradable polymeric microspheres containing protein fabricated by double-emulsion solvent extraction/evaporation method. *Biomaterials* **2001**, 22, 231-41.

[209] Mellott, M. B.; Searcy, K.; Pishko, M. V. Release of protein from highly cross-linked hydrogels of poly(ethylene glycol) diacrylate fabricated by UV polymerization.

Biomaterials **2001**, 22, 929-41.

[210] Sulkowska, A. Interaction of drugs with bovine and human serum albumin. *J. Mol. Struct.* **2002**, 614, 227-32.

[211] Albani, J. R. Structure and Dynamics of Macromolecules: Absorption and Fluorescence Studies. Amsterdam: Elsevier pp 99-140; 2004.

[212] Wei, Y. L.; Li, J. Q.; Dong, C.; Shuang, S. M.; Liu, D. S.; Huie, C. W. Investigation of the association behaviors between biliverdin and bovine serum albumin by fluorescence spectroscopy. *Talanta* **2006**, 70, 377-82.

[213] Qin, C.; Xie, M. X.; Liu, Y. Characterization of the myricetin-human serum albumin complex by spectroscopic and molecular modeling approaches. *Biomacromolecules* **2007**, 8, 2182-9.

[214] Papadopoulou, A.; Green, R. J.; Frazier, R. A. Interaction of flavonoids with bovine serum albumin: A fluorescence quenching study. *J. Agric. Food. Chem.* **2005**, 53, 158-63.

[215] Creamer, L. K. Effect of Sodium Dodecyl-Sulfate and Palmitic Acid on the Equilibrium Unfolding of Bovine Beta-Lactoglobulin. *Biochemistry* **1995**, 34, 7170-6.

[216] Saha, B.; Das, G. Malachite Nanoparticle: A New Basic Hydrophilic Surface for pH-Controlled Adsorption of Bovine Serum Albumin with a High Loading Capacity. *J. Phys. Chem. C* **2009**, 113, 15667-75.

[217] Klajnert, B.; Stanislawska, L.; Bryszewska, M.; Palecz, B. Interactions between PAMAM dendrimers and bovine serum albumin. *Bba-Proteins Proteom* **2003**, 1648, 115-26.

[218] Lee, C. T.; Smith, K. A.; Hatton, T. A. Photocontrol of protein folding: The interaction of

photosensitive surfactants with bovine serum albumin. *Biochemistry* **2005**, 44, 524-36.

[219] Sadler, P. J.; Tucker, A. Ph-Induced Structural Transitions of Bovine Serum-Albumin - Histidine Pka Values and Unfolding of the N-Terminus during the N to F Transition. *Eur. J. Biochem.* **1993**, 212, 811-7.

[220] Efimova, Y. M.; Haemers, S.; Wierczinski, B.; Norde, W.; van Well, A. A. Stability of globular proteins in H2O and D2O. *Biopolymers* **2007**, 85, 264-73.

[221] Vertegel, A. A.; Siegel, R. W.; Dordick, J. S. Silica nanoparticle size influences the structure and enzymatic activity of adsorbed lysozyme. *Langmuir* **2004**, 20, 6800-7.

[222] Jachimska, B.; Wasilewska, M.; Adamczyk, Z. Characterization of globular protein solutions by dynamic light scattering, electrophoretic mobility, and viscosity measurements. *Langmuir* **2008**, 24, 6866-72.

[223] Rezwan, K.; Meier, L. P.; Rezwan, M.; Voros, J.; Textor, M.; Gauckler, L. J. Bovine serum albumin adsorption onto colloidal Al2O3 particles: A new model based on zeta potential and UV-vis measurements. *Langmuir* **2004**, 20, 10055-61.

[224] Labhasetwar, V.; Song, C. X.; Humphrey, W.; Shebuski, R.; Levy, R. J. Arterial uptake of biodegradable nanoparticles: Effect of surface modifications. *J. Pharm. Sci.* **1998**, 87, 1229-34.

[225] Wang, H. D.; Yang, Q. Q.; Niu, C. H. Functionalization of nanodiamond particles with N,O-carboxymethyl chitosan. *Diamond Relat. Mater.* **2010**, 19, 441-4.

[226] Brewer, S. H.; Glomm, W. R.; Johnson, M. C.; Knag, M. K.; Franzen, S. Probing BSA binding to citrate-coated gold nanoparticles and surfaces. *Langmuir* **2005**, 21, 9303-7.

[227] Yoon, J. Y.; Park, H. Y.; Kim, J. H.; Kim, W. S. Adsorption of BSA on highly carboxylated microspheres - Quantitative effects of surface functional groups and interaction forces. *J. Colloid Interface Sci.* **1996**, 177, 613-20.

[228] Freitas, C.; Muller, R. H. Effect of light and temperature on zeta potential and physical stability in solid lipid nanoparticle (SLN (TM)) dispersions. *Int. J. Pharm.* **1998**, 168, 221-9.

[229] Karajanagi, S. S.; Yang, H. C.; Asuri, P.; Sellitto, E.; Dordick, J. S.; Kane, R. S. Protein-assisted solubilization of single-walled carbon nanotubes. *Langmuir* **2006**, 22, 1392-5.

[230] Edri, E.; Regev, O. pH effects on BSA-dispersed carbon nanotubes studied by spectroscopy-enhanced composition evaluation techniques. *Anal. Chem.* **2008**, 80, 4049-54.

[231] Edri, E.; Regev, O. "Shaken, Not Stable": Dispersion Mechanism and Dynamics of Protein-Dispersed Nanotubes Studied via Spectroscopy. *Langmuir* **2009**, 25, 10459-65.

[232] Birenbaum, N. S.; Lai, B. T.; Chen, C. S.; Reich, D. H.; Meyer, G. J. Selective noncovalent adsorption of protein to bifunctional metallic nanowire surfaces. *Langmuir* **2003**, 19, 9580-2.

[233] Wang, J.; Xu, D. K.; Kawde, A. N.; Polsky, R. Metal nanoparticle-based electrochemical stripping potentiometric detection of DNA hybridization. *Anal. Chem.* **2001**, 73, 5576-81.

[234] Yang, N. J.; Uetsuka, H. S.; Sawa, E.; Nebel, C. E. Vertically Aligned Nanowires from Boron-Doped Diamond. *Nano Lett.* **2008**, 8, 3572-6.

[235] Creighton, T. E. *Protein structure: a practical approach, second ed.,* Oxford, New York, , 1997.

[236] Twardowski, M.; Nuzzo, R. G. Chemically mediated grain growth in nanotextured Au, Au/Cu thin films: Novel substrates for the formation of self-assembled monolayers. *Langmuir* **2002**, 18, 5529-38.

[237] Zhang, M. N.; Yan, Y. M.; Gong, K. P.; Mao, L. Q.; Guo, Z. X.; Chen, Y. Electrostatic layer-by-layer assembled carbon nanotube multilayer film and its electrocatalytic activity for O-2 reduction. *Langmuir* **2004**, 20, 8781-5.

[238] Gomez, H.; Ram, M. K.; Alvi, F.; Stefanakos, E.; Kumar, A. Novel Synthesis, Characterization, and Corrosion Inhibition Properties of Nanodiamond-Polyaniline Films. *J. Phys. Chem. C* **2010**, 114, 18797-804.

[239] Carroll, J. B.; Frankamp, B. L.; Srivastava, S.; Rotello, V. M. Electrostatic self-assembly of structured gold nanoparticle/polyhedral oligomeric silsesquioxane (POSS) nanocomposites. *J. Mater. Chem.* **2004**, 14, 690-4.

[240] Hammond, P. T.; Kim, J.; Lee, S. W.; Shao-Horn, Y. Electrostatic Layer-by-Layer Assembled Au Nano particle/MWNT Thin Films: Microstructure, Optical Property, and Electrocatalytic Activity for Methanol Oxidation. *Chem. Mater.* **2009**, 21, 2993-3001.

[241] Kotov, N. A.; Shim, B. S.; Zhu, J.; Jan, E.; Critchley, K.; Ho, S. S.; Podsiadlo, P.; Sun, K. Multiparameter Structural Optimization of Single-Walled Carbon Nanotube Composites: Toward Record Strength, Stiffness, and Toughness. *Acs Nano* **2009**, 3, 1711-22.

[242] Richert, L.; Lavalle, P.; Payan, E.; Shu, X. Z.; Prestwich, G. D.; Stoltz, J. F.; Schaaf, P.;

Voegel, J. C.; Picart, C. Layer by layer buildup of polysaccharide films: Physical chemistry and cellular adhesion aspects. *Langmuir* **2004**, 20, 448-58.

[243] Siemens, J.; Huschek, G.; Siebe, C.; Kaupenjohann, M. Concentrations and mobility of human pharmaceuticals in the world's largest wastewater irrigation system, Mexico City-Mezquital Valley. *Water Res.* **2008**, 42, 2124-34.

[244] Balakrishnan, V. K.; Terry, K. A.; Toito, J. Determination of sulfonamide antibiotics in wastewater: A comparison of solid phase microextraction and solid phase extraction methods. *J. Chromatogr. A* **2006**, 1131, 1-10.

[245] Rains, C. P.; Noble, S.; Faulds, D. Sulfasalazine - a Review of Its Pharmacological Properties and Therapeutic Efficacy in the Treatment of Rheumatoid-Arthritis. *Drugs* **1995**, 50, 137-56.

[246] Bauer, C.; Jacques, P.; Kalt, A. Investigation of the interaction between a sulfonated azo dye (AO7) and a TiO2 surface. *Chem. Phys. Lett.* **1999**, 307, 397-406.

[247] Bourikas, K.; Stylidi, M.; Kondarides, D. I.; Verykios, X. E. Adsorption of acid orange 7 on the surface of titanium dioxide. *Langmuir* **2005**, 21, 9222-30.

[248] Das, C.; Saha, A.; Hung, C. H.; Lee, G. H.; Peng, S. M.; Goswami, S. Ruthenium complexes of 2-[(4-(arylamino)phenyl)azo]pyridine formed via regioselective phenyl ring amination of coordinated 2-(phenylazo)pyridine: Isolation of products, X-ray structure, and redox and optical properties. *Inorg. Chem.* **2003**, 42, 198-204.

[249] Kaim, W.; Doslik, N.; Frantz, S.; Sixt, T.; Wanner, M.; Baumann, F.; Denninger, G.; Kummerer, H. J.; Duboc-Toiac, C.; Fiedler, J.; Zalis, S. Azo compounds as electron

acceptor or radical ligands in transition metal species: spectroelectrochemistry and high-field EPR studies of ruthenium, rhodium and copper complexes of 2,2 '-azobis(5-chloropyrimidine). *J. Mol. Struct.* **2003**, 656, 183-94.

[250] Zhu, D. Q.; Pignatello, J. J. Characterization of aromatic compound sorptive interactions with black carbon (charcoal) assisted by graphite as a model. *Environ. Sci. Technol.* **2005**, 39, 2033-41.

[251] Ji, L. L.; Chen, W.; Duan, L.; Zhu, D. Q. Mechanisms for strong adsorption of tetracycline to carbon nanotubes: A comparative study using activated carbon and graphite as adsorbents. *Environ. Sci. Technol.* **2009**, 43, 2322-7.

[252] Bandara, J.; Mielczarski, J. A.; Kiwi, J. 1. Molecular mechanism of surface recognition. Azo dyes degradation on Fe, Ti, and Al oxides through metal sulfonate complexes. *Langmuir* **1999**, 15, 7670-9.

[253] Msagati, T. A. M.; Nindi, M. M. Multiresidue determination of sulfonamides in a variety of biological matrices by supported liquid membrane with high pressure liquid chromatography-electrospray mass spectrometry detection. *Talanta* **2004**, 64, 87-100.

[254] French, D. L.; Mauger, J. W. Evaluation of the Physicochemical Properties and Dissolution Characteristics of Mesalamine - Relevance to Controlled Intestinal Drug-Delivery. *Pharm. Res.* **1993**, 10, 1285-90.

[255] Zerrouk, N.; Dorado, J. M. G.; Arnaud, P.; Chemtob, C. Physical characteristics of inclusion compounds of 5-ASA in alpha and beta cyclodextrins. *Int. J. Pharm.* **1998**, 171, 19-29.

[256] Ji, L. L.; Chen, W.; Zheng, S. R.; Xu, Z. Y.; Zhu, D. Q. Adsorption of Sulfonamide Antibiotics to Multiwalled Carbon Nanotubes. *Langmuir* **2009**, 25, 11608-13.

[257] Thiele-Bruhn, S.; Seibicke, T.; Schulten, H. R.; Leinweber, P. Sorption of sulfonamide pharmaceutical antibiotics on whole soils and particle-size fractions. *J. Environ. Qual.* **2004**, 33, 1331-42.

[258] Rodriguez, A.; Ovejero, G.; Sotelo, J. L.; Mestanza, M.; Garcia, J. Adsorption of dyes on carbon nanomaterials from aqueous solutions. *J. Environ. Sci. Heal. A* **2010**, 45, 1642-53.

[259] Silva, J. P.; Sousa, S.; Rodrigues, J.; Antunes, H.; Porter, J. J.; Goncalves, I.; Ferreira-Dias, S. Adsorption of acid orange 7 dye in aqueous solutions by spent brewery grains. *Sep. Purif. Technol.* **2004**, 40, 309-15.

[260] Gotovac, S.; Hattori, Y.; Noguchi, D.; Miyamoto, J.; Kanamaru, M.; Utsumi, S.; Kanoh, H.; Kaneko, K. Phenanthrene adsorption from solution on single wall carbon nanotubes. *J. Phys. Chem. B* **2006**, 110, 16219-24.

[261] Kasai, P. H. Dissociative Electron-Capture of Sulfones and Sulfonates - Matrix-Isolation Esr Study. *J. Am. Chem. Soc.* **1991**, 113, 3317-21.

[262] Allen, L.; Weinberger, J.; Weinberger, R. Determination of impurities in the drug 5-aminosalicylic acid by micellar electrokinetic capillary chromatography using an electrolyte pH that approaches the isoelectric point of the parent compound. *J. Chromatogr. A* **2004**, 1053, 217-26.

[263] French, D. L.; Himmelstein, K. J.; Mauger, J. W. Physicochemical aspects of controlled release of substituted benzoic and naphthoic acids from Carbopol(R) gels.

J.Control.Release **1995**, 37, 281-9.

[264] Wang, H.; Zeng, H.; Liu, Z. M.; Yang, Y. H.; Deng, T.; Shen, G. L.; Yu, R. Q. Immunophenotyping of acute leukemia using an integrated piezoelectric immunosensor array. *Anal. Chem.* **2004**, 76, 2203-9.

[265] Wang, H.; Ding, Y. J.; Liu, J.; Shen, G. L.; Yu, R. Q. A piezoelectric immunosensor for the detection of alpha-fetoprotein using an interface of gold/hydroxyapatite hybrid nanomaterial. *Biomaterials* **2007**, 28, 2147-54.

[266] Nakanishi, K.; Muguruma, H.; Karube, I. A novel method of immobilizing antibodies on a quartz crystal microbalance using plasma-polymerized films for immunosensors. *Anal. Chem.* **1996**, 68, 1695-700.

[267] Wang, K.; Xu, D.; Hein, S.; Loo, L. S. Modified Chitosan Hydrogels for the Removal of Acid Dyes at High pH: Modification and Regeneration. *Ind. Eng. Chem. Res.* **2011**, 50, 6343-6.

[268] Peng, X. J.; Wang, J.; Luan, Z.; Zhao, C. W. Regeneration of carbon nanotubes exhausted with dye reactive red 3BS using microwave irradiation. *J. Hazard. Mater.* **2010**, 178, 1125-7.

[269] Lee, M. W.; Chatterjee, S.; Woo, S. H. Adsorption of congo red by chitosan hydrogel beads impregnated with carbon nanotubes. *Bioresource Technol.* **2010**, 101, 1800-6.

[270] Woo, S. H.; Chatterjee, S.; Chatterjee, T.; Lim, S. R. Effect of the addition mode of carbon nanotubes for the production of chitosan hydrogel core-shell beads on adsorption of Congo red from aqueous solution. *Bioresource Technol.* **2011**, 102, 4402-9.